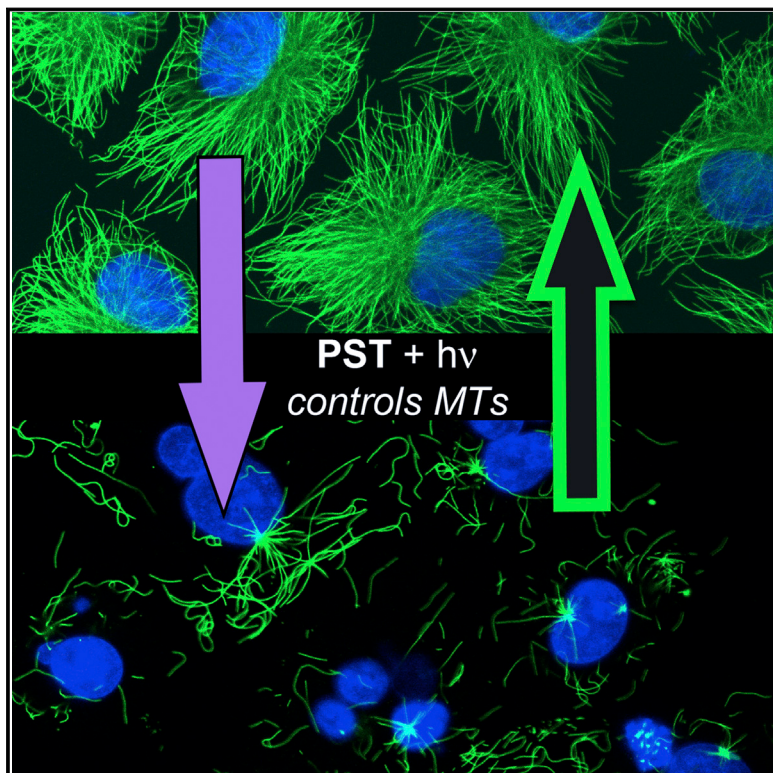


Photoswitchable Inhibitors of Microtubule Dynamics Optically Control Mitosis and Cell Death

Graphical Abstract



Authors

Malgorzata Borowiak, Wallis Nahaboo,
Martin Reynders, ..., Angelika Vollmar,
Dirk Trauner, Oliver Thorn-Seshold

Correspondence

dirk.trauner@cup.uni-muenchen.de
(D.T.),
oliver.thorn-seshold@cup.
uni-muenchen.de (O.T.-S.)

In Brief

Microtubule-inhibiting small molecules are crucial for cell biology research and in cancer therapy. Photostatins are microtubule inhibitors that can be switched on and off in vivo by visible light, modulating microtubule dynamics with subsecond response time, and controlling mitosis with single-cell spatial precision. Photostatins are also 250 times more cytotoxic under blue light than when kept in the dark, making them both valuable tools for cell biology, and promising as precision-targeted chemotherapeutics.

Highlights

- Photostatins (PSTs) switch microtubule dynamics off and on under blue and green light
- PSTs modulate microtubule dynamics in live cells with response time below 1 s
- PSTs control mitosis in vivo with spatial precision on the single-cell level
- PSTs exposed to blue light are 250 times more cytotoxic than PSTs kept in the dark

Photoswitchable Inhibitors of Microtubule Dynamics Optically Control Mitosis and Cell Death

Małgorzata Borowiak,^{1,2} Wallis Nahaboo,² Martin Reynders,¹ Katharina Nekolla,⁴ Pierre Jalinot,² Jens Hasserodt,³ Markus Rehberg,⁴ Marie Delattre,² Stefan Zahler,¹ Angelika Vollmar,¹ Dirk Trauner,^{1,*} and Oliver Thorn-Seshold^{1,3,*}

¹Department of Chemistry and Pharmacy and Centre for Integrated Protein Science, Ludwig-Maximilians-University Munich, 5-13 Butenandtstrasse, 81377 Munich, Germany

²Laboratoire de Biologie Moléculaire de la Cellule, CNRS, École Normale Supérieure de Lyon, 46 Allée d'Italie, 69364 Lyon, France

³Laboratoire de Chimie, CNRS, École Normale Supérieure de Lyon, 46 Allée d'Italie, 69364 Lyon, France

⁴Walter Brendel Centre of Experimental Medicine, 27 Marchioninistrasse, Ludwig-Maximilians-Universität, München, Munich 81377, Germany

*Correspondence: dirk.trauner@cup.uni-muenchen.de (D.T.), oliver.thorn-seshold@cup.uni-muenchen.de (O.T.-S.)

<http://dx.doi.org/10.1016/j.cell.2015.06.049>

SUMMARY

Small molecules that interfere with microtubule dynamics, such as Taxol and the Vinca alkaloids, are widely used in cell biology research and as clinical anticancer drugs. However, their activity cannot be restricted to specific target cells, which also causes severe side effects in chemotherapy. Here, we introduce the photostatins, inhibitors that can be switched on and off in vivo by visible light, to optically control microtubule dynamics. Photostatins modulate microtubule dynamics with a subsecond response time and control mitosis in living organisms with single-cell spatial precision. In longer-term applications in cell culture, photostatins are up to 250 times more cytotoxic when switched on with blue light than when kept in the dark. Therefore, photostatins are both valuable tools for cell biology, and are promising as a new class of precision chemotherapeutics whose toxicity may be spatiotemporally constrained using light.

INTRODUCTION

Microtubules (MTs) are highly dynamic components of the cytoskeleton that play vital roles in a variety of cellular processes, including intracellular transport, cell motility, and proliferation (Dumontet and Jordan, 2010). As such, small molecule inhibitors that interfere with MT dynamics are indispensable tools in cell biology (Peterson and Mitchison, 2002). In medicine, they are one of the most clinically useful classes of chemotherapeutics, due to their antimitotic and pro-apoptotic effects (Jordan et al., 1998). However, the current inhibitors are nonspecific in the sense that their bioactivity cannot be either spatially or temporally directed, e.g., against selected cells and tissues, at defined times. This restricts their scope of application in research, as it prevents their use in spatially or temporally addressing the varied processes dependent on microtubule dynamics. In cancer medicine, this nonspecificity causes severe systemic side effects such as cardiotoxicity and neurotoxicity (Ghinet et al., 2013;

Hooper et al., 2013; Tozer et al., 2002; Tron et al., 2006), which limit the doses at which chemotherapeutics can be applied, thus impairing their therapeutic value (Dumontet and Jordan, 2010; Gill et al., 2014; Stanton et al., 2011). Therefore, developing inhibitors of MT dynamics whose action can be targeted to specific cells at defined times is an important challenge (Velema et al., 2014).

Optically controlling MT inhibitors could be an elegant solution to this problem of specificity, since light can be applied with high spatiotemporal precision (Velema et al., 2014). Small molecule approaches are particularly attractive, since genetic engineering is not required and dosing is straightforward, so their scope for practical applications to both research and medicine is extensive. Prior research toward the optical modulation of MT inhibitors has explored both photobleachable and photouncageable drugs (Hadfield et al., 2002; Hamaguchi and Hiramoto, 1986; Velema et al., 2014; Wühr et al., 2010), and a photoactivation approach based on carbon-carbon double bond isomerization has been proposed (Bisby et al., 2013; Hadfield et al., 2002). However, the nonspecific toxicity of these designs may be significant, since short wavelengths and/or high light intensity are required, leading to side reactions and toxic byproducts (Wu et al., 2009). Fundamentally though, such irreversibly triggered approaches cannot combat the diffusion of the active drug, so they will always suffer from limited spatiotemporal resolution. Spatially and temporally restricting bioactivity instead demands reversible, *in situ* switching over many off↔on cycles (Velema et al., 2014). We here present a series of MT inhibitors that can be fully reversibly photoswitched by low-intensity visible light, to control microtubule structure, dynamics, and a range of MT-dependent processes in living cells and organisms, with the spatiotemporal precision of light.

RESULTS

Design and Photoswitching of Photostatins

We designed the photostatins (PSTs) as reversibly photoswitchable analogs of combretastatin A-4 (CA4) (Pettit et al., 1989). CA4 is one of the most prominent colchicine domain MT inhibitors (CDIs). Its potency, its vascular disrupting and antiangiogenic properties, and its avoidance of multidrug-resistance make it a promising candidate for tumor chemotherapy, and

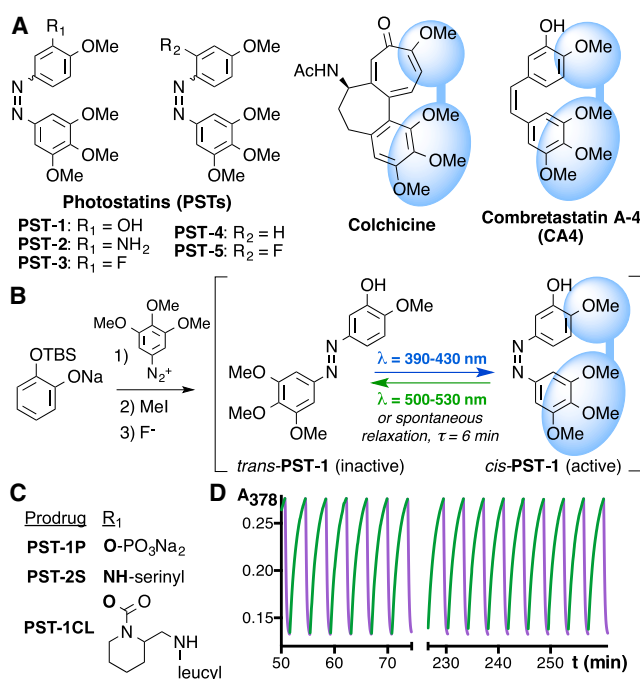


Figure 1. Design, Synthesis and Switching of the Photostatins

(A) Structural comparison of PSTs with colchicine and CA4 (the pharmacophore is indicated in blue).
 (B) Synthesis and switching of representative compound PST-1: only the *cis* isomer displays the CDI pharmacophore.
 (C) PST prodrugs that are unmasked by enzymes.
 (D) PST-1 is rapidly and reversibly photoswitched, with excellent photostability, by alternating 388 nm (violet) and 508 nm (green) illuminations (plot: absorbance at 378 nm, in PBS; see also Figures S1A and S1B).

three CA4 derivatives have progressed to clinical trials (Tozer et al., 2002; Tron et al., 2006). The CA4 pharmacophore is a trimethoxybenzene ring held *cis* to a low-steric-demand, methoxy-bearing arene (Bhattacharyya et al., 2008). Crucially, *trans*-CA4 is several orders of magnitude less potent than the *cis* isomer (Tron et al., 2006). We replaced the bridging C=C double bond of the stilbenoid combretastatins with an isosteric N=N double bond to give the azobenzene PSTs, which can be *trans*↔*cis* photoisomerized with full reversibility and excellent photostability over many cycles by low intensity visible light (Figure 1). We anticipated that the *cis*-PSTs would reproduce the valuable pharmacology of CA4, while their *trans* isomers would be biologically inactive. We aimed to reversibly photoswitch PSTs between the *cis* and *trans* isomeric forms *in situ*, to turn their bioactivity on and off, with high spatiotemporal precision, inside living cells and organisms.

We synthesized a series of PSTs (PST-1–PST-5) by diazonium coupling, in two to four synthetic steps (Figure 1 and Supplemental Information) (Thorn-Seshold et al., 2014). Considering the solubility problems that have hampered the combretastatins, we also prepared PST-1P and PST-2S, as azobenzene analogs (“azologues”) of two nonspecific combretastatin prodrugs that have entered Phase III clinical trials: PST-1P is an azologue of CA4P or “fosbretabulin” and

PST-2S is an azologue of the serinyl anilide “ombrabulin” (Ohsumi et al., 1998; Pettit and Rhodes, 2009). Lastly, PST-1CL was synthesized to explore dual optical-and-biochemical targeting via exopeptidases (Thorn-Seshold et al., 2012).

The switching of the PSTs was demonstrated by UV-Vis spectroscopy (Figure 1D and Supplemental Information, Part B). All compounds were rapidly and fully reversibly photoswitched in phosphate-buffered saline (PBS) buffer, without degradation over hundreds of cycles, by low-power illumination. Their *para*-methoxy substituents enable PSTs to be *trans*↔*cis* photoswitched using visible light (Knoll, 2003), benefiting *in vivo* compatibility: 380–420 nm light gives approximately 90% *cis* isomer, which bears the CDI pharmacophore; longer wavelengths give decreasing *cis* percentages until 500–530 nm gives approximately 85% *trans* isomer, which does not bear the pharmacophore (Figure S1A). In the dark, spontaneous (unidirectional) *cis*→*trans* isomerization leads to 100% *trans* isomer, with half-lives τ , ranging from 0.8–120 min (Figure S1B), being modulated by the substitution pattern (Knoll, 2003). This process acts as a safety mechanism, whereby the concentration of bioactive *cis* isomer will drop to zero unless blue light pulses are reapplied on the timescale of this reversion half-life. Therefore, even without using green light to actively switch off the PSTs, any *cis*-PST diffusing into a non-illuminated area, or remaining after a period of illumination, will spontaneously and rapidly be isomerized to *trans*, thus spatiotemporally restricting the PSTs’ inhibitory bioactivity to illuminated zones only.

The Toxicity of PSTs Depends on Illumination Conditions

The potency, robustness, and light-specificity of the PSTs’ biological effects were directly assessed *in cellulo*. *Trans*-PSTs were assayed by shielding experiments from light (100% *trans*; “dark regime”), while *cis*-PSTs were assayed by applying a “toxic regime” of frequently pulsed, short illuminations (e.g., 75 ms pulses of 390 nm light every 15 s). To apply these illuminations in cell culture, we hand-built a cheap, computerized LED lighting system to illuminate > 30 well plates separately with independent wavelengths and timings (Figure S6 and Supplemental Information). Crystal violet assays in the MDA-MB-231 human breast cancer cell line showed that PSTs are powerfully cytotoxic under the toxic lighting regime, but not in the dark. Their EC₅₀ values of 0.5–5.4 μM under the toxic regime represent potencies up to 100 times greater than under the dark regime (Figures 2A and 2B and Figures S2A–S2I), and closely similar results were obtained for the PSTs’ light-dependent cytotoxicity in HeLa (cervical cancer) cells (Figures S2J–S2N).

We then investigated the dependency of the PSTs’ bioactivity on the irradiating wavelength in detail. We examined the proliferation of HeLa cells exposed to PST-1P, after pulsed illuminations at a range of wavelengths from 370–535 nm, by MTT assay (Figures 2C and 2D). Illumination at 380–390 nm gave the most potent cytotoxicity, while the dose-response curves for wavelengths up to 525 nm were translated progressively higher concentrations by factors that match the relative *trans*/*cis* ratios at those wavelengths (Figure S1C). This supports the conclusions that the choice of illuminating wavelength determines the concentration of the *cis* form generated, and that this *cis* concentration is the primary determinant of the PSTs’ bioactivity. For

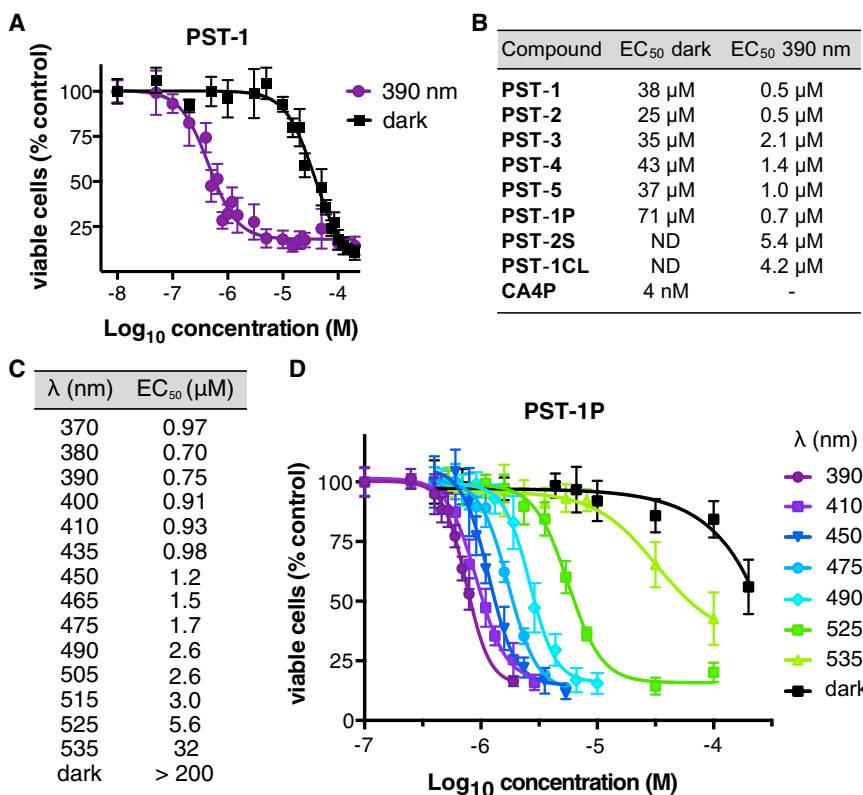


Figure 2. PSTs Are Submicromolar Cytotoxins when Irradiated with 390 nm Light, but Even >250 Times Less Toxic in the Dark

(A) Cell viability dose-response curves for PST-1 under 390 nm irradiation and in the dark are separated by approximately 2 orders of magnitude (crystal violet staining, MDA-MB-231 cells, cosolvents used).

(B) PSTs are between 20- to 100-fold more cytotoxic under 390 nm illuminations than in the dark (same data as in A; see also Figures S2A–S2I).

(C) The cytotoxicity of PST-1P can be tuned by choosing the wavelength of light applied (MTT assay, HeLa cells, no cosolvents used).

(D) Dose-response curves for PST-1P are horizontally translated according to the irradiating wavelength used (same data as in C; see also Figure S1C).

Results are given as mean ± SD.

PST-1P were analyzed by western blot and showed the PARP proteolytic signature typical of apoptosis only under the toxic lighting regime (Figure 3C).

Finally, cell-cycle analysis of MDA-MB-231 cells treated with PST-1 showed G₂/M phase arrest beginning sharply around 500 nM under the toxic regime (Figures 3D and 3E), matching the EC₅₀

comparison, the *trans* isomer (assayed under dark conditions) was confirmed to be > 250 times less toxic than the *cis* form, and also showed a markedly shallower dose-dependency that could argue for a different biochemical mechanism of toxicity (Figure 2D, Figure S1C, and Supplemental Information, Part C1). These experiments indicate how the PSTs' biological effects can be not only sharply controlled (illuminated or dark), but also finely tuned (wavelength dependence) by lighting conditions.

PSTs Induce Mitotic Arrest and Cell Death in a Light-Dependent Manner

We pursued further studies of the mechanism and light-dependency of PST-induced cytotoxicity focusing on PST-1 and its prodrug PST-1P. We first assayed cell membrane permeability (propidium iodide exclusion assay) and nuclear fragmentation (quantification of DNA content) in MDA-MB-231 cells. Neither assay showed a response to PST-1 below 50 μM in the dark regime. However, under the toxic regime, even submicromolar PST-1 induced loss of membrane integrity, and depletion of nuclear DNA content resulting in the emergence of hypodiploid (sub-G₁) cells (Figures 3A and 3B and Figure S3E). Similar results were obtained in Jurkat (T cell lymphoma) and HeLa cells (Figures S3A–S3D). We subsequently examined cleavage of poly(ADP-ribose) polymerase (PARP). Full-length PARP (116 kDa) is involved in the repair of DNA damage caused by a variety of cellular stresses. During apoptosis, PARP is cleaved by caspase-3, caspase-7, and possibly by other suicidal proteases, into an 89-kDa catalytic fragment and a 24-kDa DNA-binding domain (Chaitanya et al., 2010). HeLa cells treated with

values seen in the cytotoxicity assays. By contrast, in the dark even 100 μM of PST-1 had no effect on cell-cycle repartition (Figures S3F and S3G). As G₂/M arrest is typical of MT-disrupting agents (Tron et al., 2006), this supports the design conjecture that only *cis*-PSTs inhibit MT dynamics. Similar results were obtained in HEK293T (human embryonic kidney) and HeLa cells (Figures S3I and S3J). We also explored a dual wavelength “rescue protocol,” to illustrate repeated, dynamic photocontrol over PST cytotoxicity. In this protocol, each pulse contains a component at 390 nm immediately followed by another at 515 nm (so that the transiently formed *cis* is reisomerized back to *trans* during each pulse). The rescue substantially reduced G₂/M arrest compared to the toxic regime (Figure S3H). This highlights that PSTs can be reversibly and efficiently photoisomerized in cellulo in the long term (>5,000 *trans* → *cis* → *trans* photoswitching cycles over 2 days), without degradation of the drug and without phototoxicity to the cell.

Taken together, these results support the interpretation that the *cis*-PSTs generated *in situ* upon blue light exposure potently induce mitotic arrest, presumably linked to the activation of the spindle assembly checkpoint, and result in cell death which displays many characteristics of apoptosis. By contrast, the *trans*-PSTs that are established under dark conditions (or which predominate under longer wavelength illumination) are all but inactive due to their ~100-fold weaker cytotoxicity, which additionally does not involve mitotic arrest. Both these results are general across a range of cell lines, supporting the conjecture that PSTs should be appropriate for use in any eukaryotic system. These experiments thereby supported our overall design,

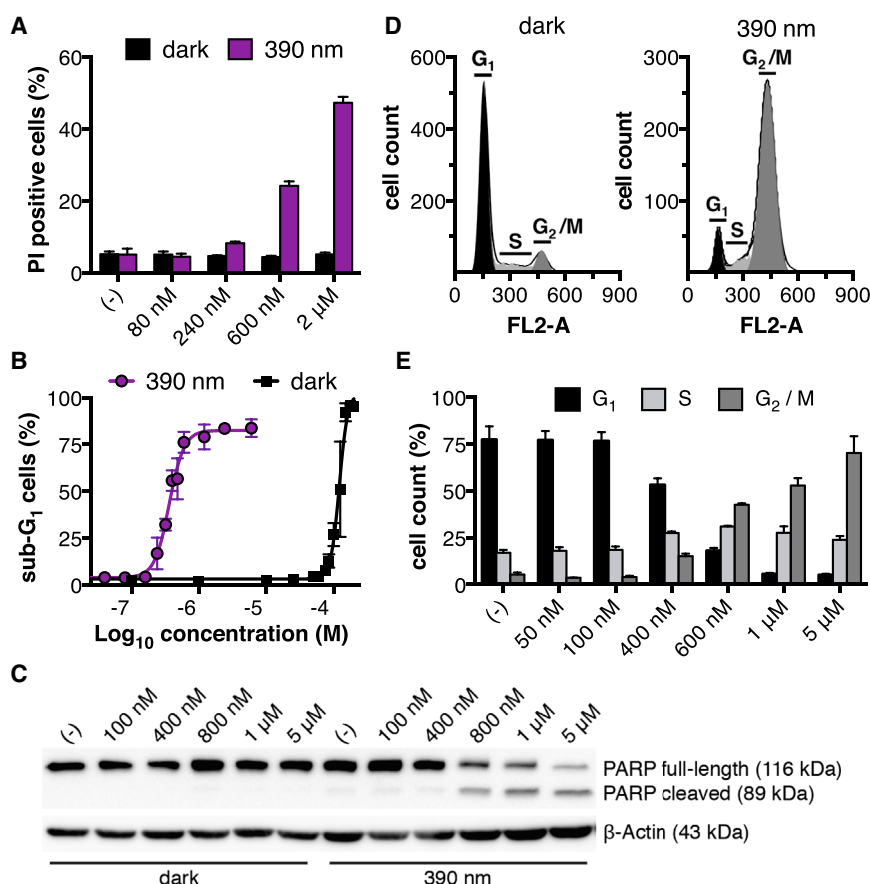


Figure 3. PSTs Induce Cell-Cycle Arrest and Apoptosis upon Blue Light Illumination, but Not in the Dark

(A) PST-1 gives light-dependent induction of membrane permeability (propidium iodide exclusion assay, MDA-MB-231 cells).

(B) PST-1 gives light-dependent induction of nuclear fragmentation (increase of sub-G₁ population; MDA-MB-231 cells).

(C) Treatment with PST-1P results in PARP cleavage upon blue light illumination, but not in the dark (western blot, HeLa cells).

(D) MDA-MB-231 cells treated with 2 μM PST-1 show normal cell-cycle repartition in the dark (left) while illumination under the toxic regime gives strong G₂/M arrest (right).

(E) PST-1 causes dose-dependent cell-cycle arrest in G₂/M phase under the toxic illumination regime.

Results are given as mean ± SD. See Figure S3 for further results.

showing that PSTs can be used as antimitotic cytotoxins that can be robustly and reversibly photoswitched in living cells between the essentially “off” *trans* form and the potent “on” *cis* form. We now turned our focus to testing the specific molecular premise of the PSTs’ design: by evaluating their capacity to effect MT disruption *in situ* in a reversibly photoswitchable manner.

PSTs Bind Tubulin and Inhibit Its Polymerization in a Light-Controlled Manner

To validate tubulin as the molecular target of *cis*-PSTs, we first assayed the ability of PST-1 to bind to the colchicine domain on tubulin. We used purified tubulin in an *in vitro* radioligand scintillation proximity assay (SPA) (Tahir et al., 2000) to examine the competitive displacement of ³H-colchicine from its tubulin binding site by PST-1 under light and dark conditions. This assay confirmed that *cis*-PST-1 competes dose dependently with colchicine for tubulin binding, as does its isosteric parent drug CA4 (Figure 4A). The SPA returned an EC₅₀ value of 30 μM for PST-1 under 390 nm illumination, with the reference compound CA4 showing higher affinity (EC₅₀ = 0.16 μM), which mirrors the activity difference shown previously in the cytotoxicity assays. Importantly, *trans*-PST-1 showed no significant competitive binding to tubulin, further supporting the off↔on design conjecture of our study.

We next assayed PST-1 for inhibition of tubulin polymerization in a biochemical assay using purified tubulin. PST-1 strongly

inhibited *in vitro* tubulin polymerization under 390 nm illumination in a dose-dependent manner (EC₅₀ ~5 μM), but exerted no inhibitory effects in the dark (EC₅₀ >> 40 μM; Figure 4B). Lastly, we confirmed PST-1’s functional potency as photoswitchable MT inhibitor in live cells by immunofluorescence imaging of endogenous tubulin. In the dark, PST-1 had no effects on MT structure, but under

the toxic regime PST-1 caused dose-dependent MT depolymerization, as well as nuclear fragmentation that is typical of apoptotic cells, as seen with the reference compound CA4 (Figure 4C, Figure S4A). This indicates that *cis*-PST-1 is a powerful inhibitor of tubulin polymerization both *in vitro* and *in cellulo*, while *trans*-PST-1 is not.

PSTs Achieve Reversible Optical Control over Microtubule Dynamics in Live Cells

To directly visualize PSTs’ effects on MT dynamics in live cells, we imaged the end-binding protein EB3. EB3 clusters at the plus tips of growing MTs, and dissociates in phases of MT shrinkage. As its binding/unbinding kinetics are fast, EB3 imaging thus reveals MT growth dynamics (Bieling et al., 2007; Maurer et al., 2012). We treated interphase cells expressing mCherry-tagged EB3 with PST-1, and imaged them while photoswitching PST-1 *in situ* with alternating 2 min phases of pulsed 405 nm and 514 nm illuminations. Control cells (without PST-1 treatment) showed no variation of comet behavior with the illumination phase. In contrast, under PST-1 treatment, applying 405 nm light led to the disappearance of EB3 comets in less than a second, while changing to a 514 nm phase restored comet size and dynamics—also in less than a second—and this switching was entirely reversible over many cycles (Movies S1 and S2; Figure 5A; see also Supplemental Information). We used the MATLAB software u-track (Applegate et al., 2011) to identify,

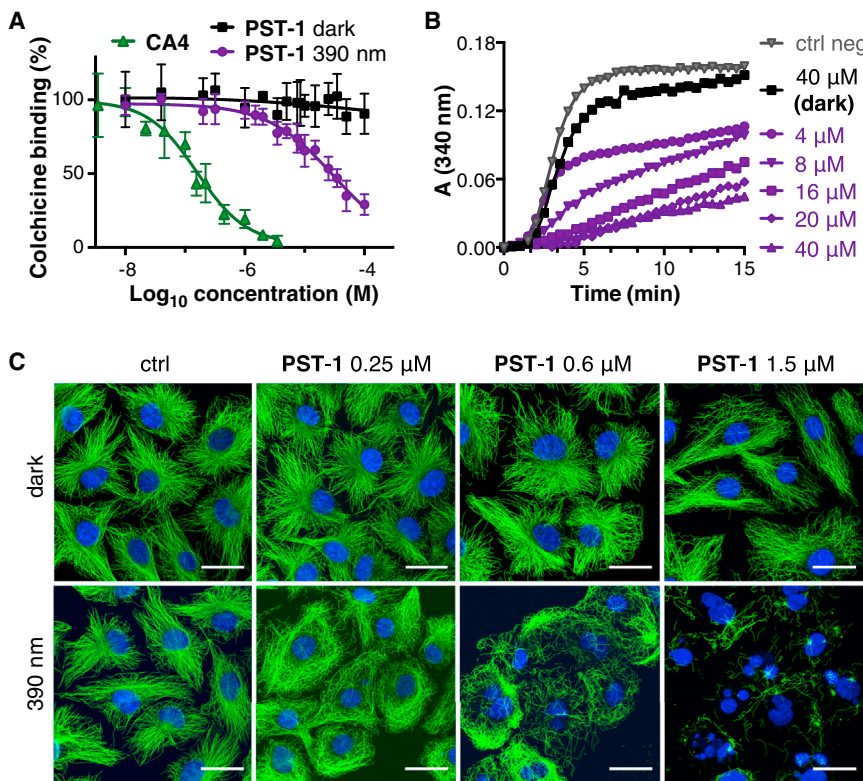


Figure 4. *cis*-PST-1 Binds at the Colchicine Site on Tubulin Heterodimers and Inhibits Tubulin Polymerization In Vitro and In Cellulo

(A) PST-1 exposed to 390 nm competes with colchicine for tubulin binding, mirroring the effect of the CA4 positive control, while no such interaction can be detected in the dark (radioligand binding assay). Results are given as mean \pm SD.

(B) PST-1 shows strong, dose-dependent inhibition of tubulin polymerization under 390 nm illumination (violet curves), but in the dark even 40 μ M PST-1 (black curve) shows near-identical behavior to the negative control (gray curve) (turbidimetric in vitro polymerization assay; greater absorbance corresponds to a greater degree of polymerization).

(C) Under the toxic regime, PST-1 induces MT breakdown and nuclear fragmentation dose-dependently, while under the dark regime, MT structure is unaffected (MDA-MB-231 cells treated for 20 hr with PST-1, then stained for α -tubulin (green) and DNA (blue); scale bars, 20 μ m; see also Figure S4A).

follow, and quantify the EB3 comets from several independent movies (Movie S3), conservatively analyzing for the total number of EB3 comets, as well as their lifetime, speed, and distance traveled. The combined statistics show that *trans* \leftrightarrow *cis* photoisomerizations of PST-1 inside living cells achieve optical switching of these functional parameters of MT polymerization dynamics, thus allowing fully reversible switching between phases of ordinary MT dynamics and of MT catastrophe simply by applying light (Figures 5B–E). Together with the preceding results, these experiments indicate that PSTs are a robust and powerful tool for precise, rapid, reversible, and noninvasive optical control over both MT dynamics and MT-dependent processes, suitable for both short- and long-term use in a range of systems from *in vitro* to *in cellulo*.

PSTs Control Mitosis and the Microtubule Cytoskeleton In Vivo

We next examined PST-1's optical control over MT dynamics *in vivo*. We monitored mitotic progression of developing *C. elegans* embryo as a readout of functional microtubule dynamics. The synchronicity of several blastomeres at early developmental stages gives a useful internal control for the normal mitosis rate (Strome and Wood, 1983). We used transgenic embryos with mCherry-tagged cell membrane marker PH and histone H2B to identify blastomeres and follow their cell-cycle progression. Embryos were bathed in PST-1, and individual cells within 8- to 32-cell stage embryos were targeted with millisecond pulses of 405 and/or 514 nm light, once the chromosomes organized into a single plate (entry to metaphase).

Applying 405 nm pulses blocked the targeted cell in metaphase (Figure 6A; Movie S4), but cells targeted by a 405 + 514 nm rescue protocol divided normally (Figure 6B; Movie S5). Crucially, in both cases, neighboring cells continued mitosis unperturbed. Thus, PST-1 can achieve reversible, optical control over MT dynamics and its dependent processes *in vivo*, and can execute that control with single-cell spatial precision.

Lastly, we examined PSTs' control over the MT cytoskeleton in mammalian tissue *in vivo*. We selected the highly water-soluble prodrug PST-1P to avoid needing a cosolvent, aiming at better *in vivo* compatibility. The cremaster muscle tissue of living mice was superfused (Baez, 1973) for 40 min with PST-1P, while being either illuminated at 390 nm with a low-power LED or else kept in the dark. Then, under red light conditions, animals were sacrificed and the tissue was excised, fixed, and stained for MTs. PST-1P destroyed the MT network under 390 nm illumination, but caused no disruptive effects in the dark (Figure 6C; Figures S5A–S5D). This confirms the suitability of PSTs for optically defined MT depolymerization in mammalian tissue *in vivo*.

DISCUSSION

Biological implementations of photoswitchable small molecules have traditionally focused on transmembrane proteins, usually expressed in neurons, whose inherently nonlinear response has contributed to many successful applications (Fehrentz et al., 2011). Here, we show that photopharmacology also offers valuable applications to intracellular targets such as the microtubule cytoskeleton, which is highly conserved and fundamental to all eukaryotes (Dumontet and Jordan, 2010). The PSTs embed a photoswitch inside the CDI pharmacophore,

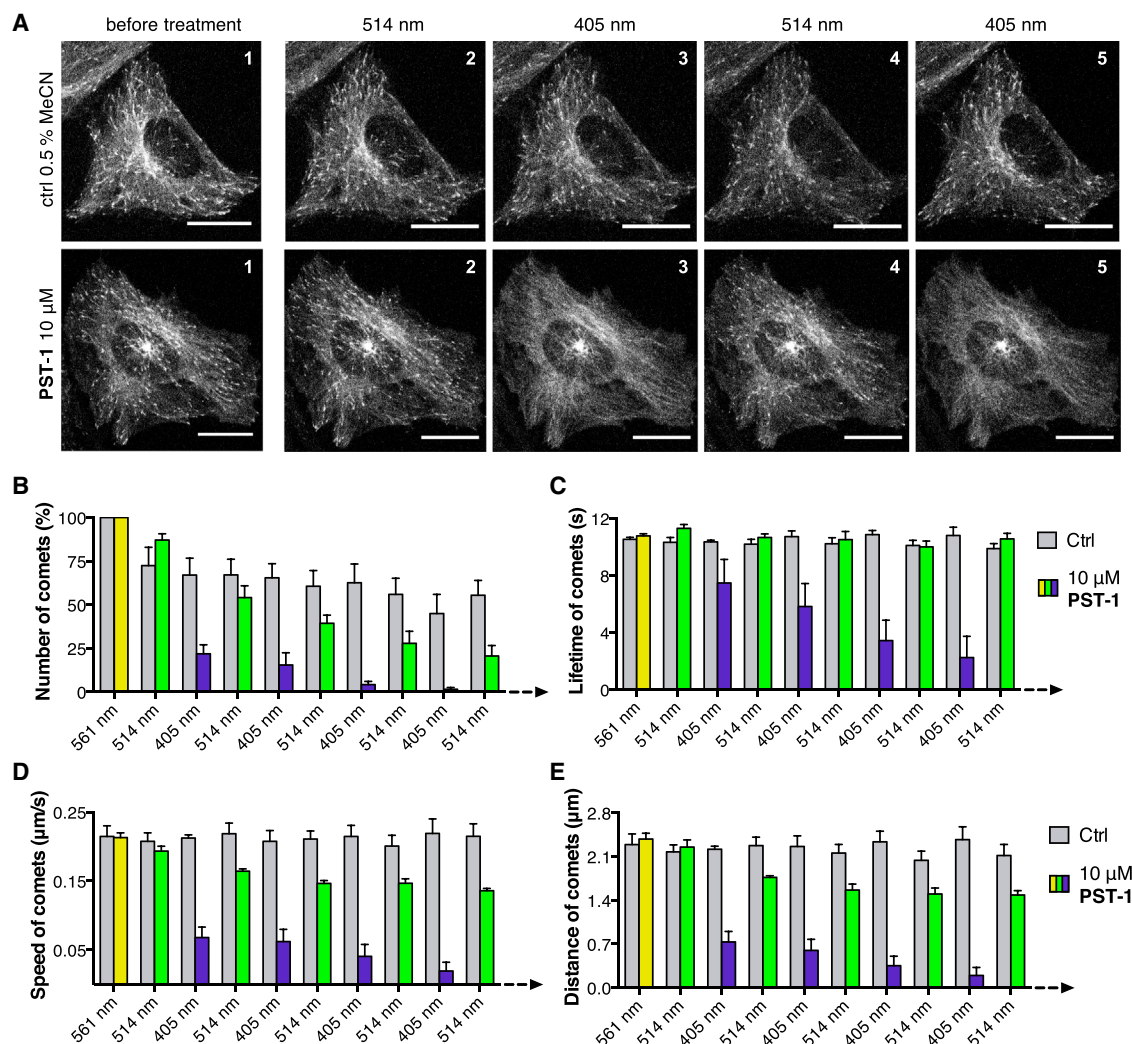


Figure 5. PST-1 Optically Controls Microtubule Dynamics in Living Cells with Full Reversibility

(A) Reversible *trans* ↔ *cis* photoisomerization of PST-1 *in cellulo* by alternating phases of blue and green light causes microtubule dynamics to stop and start again, with <1 s response time and with full reversibility (see full data in [Movies S1](#) and [S2](#)). MDA-MB-231 cells transiently expressing EB3-mCherry were incubated for 10 min in the dark with 10 μ M PST-1 or with cosolvent control, then imaged at 561 nm under alternating phases of illuminations at 405 nm and 514 nm (images from the time-lapse sequence are shown in chronological order; scale bars, 20 μ m).

(B–E) Statistical analysis of the number of EB3 comets (B), and their lifetime (C), speed (D), and total distance traveled (E) show that PST-1 treatment allows for full, reversible optical control over microtubule dynamics *in cellulo*, with MT dynamics being blocked under phases of blue illumination but resuming normal behavior under phases of green illumination. Grey bars represent data for cells illuminated but without PST-1 treatment, while colored bars represent cells illuminated and treated with PST-1 at 10 μ M (for which the color indicates the phase's illumination wavelength). Data were assembled from u-track analysis of multiple independent movies acquired as in (A), and are given as mean ± SEM for each phase, with phases arranged in chronological order; each phase lasted 2 min. The bleaching of the mCherry tag over the course of the experiment reduces the automatic detection of EB3 comets by u-track, which progressively reduces the apparent comet number determined by conservative analysis (B); for unbiased analysis consult the original data in [Movies S1](#) and [S2](#).

generating minimal-complexity cell permeant compounds which are straightforward to synthesize and can be applied as water-soluble prodrugs. The PSTs have reproduced the MT disrupting, cytostatic, and cytotoxic effects of their CDI isosteres ([Bhattacharyya et al., 2008](#)) through *in vitro*, *in cellulo*, and *in vivo* assays, with the novel advantage that PSTs can spatially and temporally target these effects with full reversibility.

PSTs can exploit visible light *trans* ↔ *cis* photoswitching, combined with spontaneous *cis* → *trans* relaxation, to create steep

cis/trans spatiotemporal gradients even *in vivo*. Since the *cis*-PSTs are two orders of magnitude more potent than the *trans*-PSTs, this allows them to apply their strong bioactivity in a highly localized fashion. The PSTs' temporal specificity on the order of seconds, and spatial specificity down to at least the single-cell level, enable a variety of precise and fully reversible studies which are inaccessible to the current MT inhibitors. We envision that finely localized light delivery, possibly combined with substitution patterns that give faster spontaneous

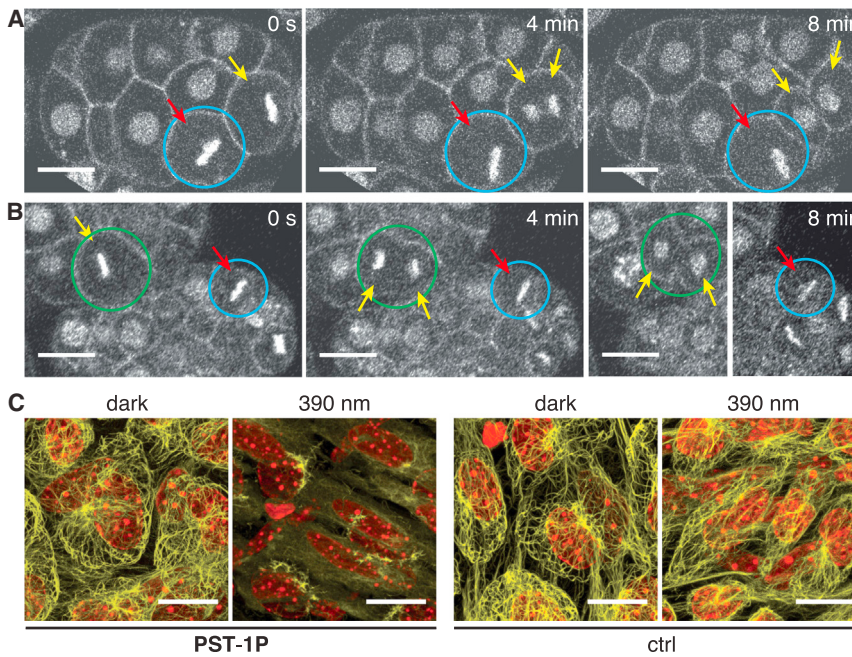


Figure 6. PSTs Optically Control MT Structure and Function In Vivo

(A and B) PSTs achieve fully reversible optical control over mitosis within a living organism, with single-cell spatial precision (see full data in [Movies S4](#) and [S5](#)). *C. elegans* embryos expressing mCherry::H2B and mCherry::PH were bathed in 40 μ M PST-1, and a single cell in each embryo was illuminated at either 405 nm (blue ROI, toxic regime) or 405 + 514 nm (green ROI, rescue protocol). Cells illuminated by the toxic regime showed mitotic arrest (stationary chromosomes marked with red arrows), while in cells exposed to the rescue protocol, chromosomes continued to segregate (yellow arrows); neighboring cells continued mitosis unperturbed. Scale bars, 10 μ m; time is shown relative to chromosome organization into the metaphase plate (start of illumination); two z-slices are given in (B) at t = 8 min, as the cells of interest had moved to distinct focal planes; see also [Figures S4B–S4G](#). (C) PST-1P applied in living mouse tissue gives complete MT disruption under 390 nm light, but has no effects in the dark. The cremaster muscle in live C57BL/6 mice was superfused with 50 μ M PST-1P or with PBS ("ctrl") for 40 min while dark conditions or 390 nm were applied. Muscle was then excised, fixed, and stained for α -tubulin (yellow) and nuclei (red). 3D-rendered z-stacks of total thickness 30 μ m are shown; scale bars, 15 μ m. See also [Figure S5](#).

cis \rightarrow *trans* relaxation, may also allow PSTs to achieve subcellularly localized MT inhibition. The reversibility of the PSTs' bioactivity allows quick recovery of normal MT function after PST treatment, so studies may establish not only the short-term consequences of inhibiting MT-dependent processes, but also their long-term effects on the whole organism. We therefore expect that PSTs will prove useful tools for spatiotemporally precise research into a range of MT-dependent processes, including intracellular transport, synaptic plasticity, cell division, motility, invasion, and angiogenesis, revealing new insights in cellular and developmental biology as well as in vivo physiology.

Considering medical applications, we anticipate that the *cis*-PSTs will share many of the features that especially suit CA4 to tumor chemotherapy ([Tron et al., 2006](#)), in addition to the cytotoxic and antimitotic properties we have demonstrated. Crucially, however, the PSTs may avoid the therapeutically limiting side effects of the current MT inhibitors, as PSTs applied globally may be activated locally by precise illumination *in vivo*. This will benefit from the light delivery methods developed over decades of research in photodynamic therapy, and more recently, in optogenetics ([Grossweiner, 2005](#); [Ibsen et al., 2013](#)). It may be possible to use dual wavelength illuminations to actively restrain the *cis* form inside a protective "belt zone" ([Figure S1F](#)). We also anticipate that the PSTs' spontaneous *cis* \rightarrow *trans* relaxation, on the scale of minutes, can passively reduce systemic exposure to bioactive *cis*-PSTs. PSTs may thus be used to deliver stronger on-target effects than can be achieved with the current, globally active MT inhibitors, while simultaneously reducing the accompanying side effects. Therefore we envision that PSTs will not only prove to be useful tools for cell biology, but also promise to deliver

more efficient cancer chemotherapy, using the spatiotemporal precision of photopharmacology.

EXPERIMENTAL PROCEDURES

Chemical Synthesis and Photocharacterizations

PSTs were synthesized and characterized by standard chemical methods. The UV-visible absorption spectra of the *cis* and *trans* isomers were determined by HPLC-UV-Vis. A monochromator was used to perform *trans* \leftrightarrow *cis* isomerizations *in vitro*, with readout by UV-Vis spectroscopy. UV-Vis spectroscopy was used to monitor spontaneous *cis* \rightarrow *trans* relaxation. Full design, synthesis, and photocharacterization of the PSTs is detailed in the [Supplemental Information](#).

Cell Culture Assays

MDA-MB-231, Jurkat, HEK293T, and HeLa cell lines were maintained under standard cell culture conditions. PSTs were applied using a minimum of cosolvent, typically 2% acetonitrile for 100 μ M PST. Cells were incubated in light-proof boxes, either in the dark (*trans*-PSTs) or with pulsed illuminations using a home-made "Disco" LED lighting system (*cis*-PSTs and rescue protocol). The Disco uses an Arduino microcomputer to operate arrays of LEDs that can be placed under or over well plates to illuminate them during an experiment. Typically, 10–30 well plates per assay were illuminated using independent pulse timings and wavelengths ([Figure S6](#)). Crystal violet staining ([Saotome et al., 1989](#)) and MTT assay ([Cushman et al., 1991](#)) were performed according to standard protocols. Nuclear fragmentation, cell-cycle analysis and propidium iodide exclusion assays were performed using flow cytometry analysis according to standard procedures ([Nicoletti et al., 1991](#)). Full details of cell culture assays and a guide to build and run the Disco LED system are given in the [Supplemental Information](#).

In Vitro Tubulin Radioligand Binding Competition Assay

Scintillation proximity assay was performed as described ([Tahir et al., 2000](#)), with the Disco LED system used to apply 390 nm light pulses to assay *cis*-PST-1 (see [Supplemental Information](#) for further details).

In Vitro Tubulin Polymerization Assay

Tubulin polymerization assay was performed as described (Lin et al., 1988), with a monochromator used to apply 390 nm light to assay the *cis*-PSTs (see *Supplemental Information* for further details).

Fixed and Live Cell Imaging by Confocal Microscopy

For fixed cell imaging, MDA-MB-231 cells were incubated with PST under illumination by the Disco system, then washed with extraction buffer to remove monomeric and dimeric tubulin subunits, fixed with glutaraldehyde, and immunostained for α -tubulin by standard methods, then imaged with a Zeiss LSM 510 Meta confocal microscope. For video microscopy, HeLa cells were transiently transfected with EB3-mCherry plasmid using the jetPRIME reagent. Following the addition of PST-1, EB3-mCherry was imaged at 561 nm at a rate of 17 frames per minute using an UltraVIEW VOX spinning-disk confocal microscope, while cells were exposed to alternating phases of pulsed photoisomerization illuminations (one 100 ms pulse every 3.53 s) using lasers at 405 nm and 514 nm, with each phase lasting for 2 min (see *Supplemental Information* for further details). EB3 comets were tracked and analyzed with the MATLAB software u-track (Applegate et al., 2011); data for corresponding photoisomerization phases were averaged across multiple independent experiments to yield the final statistics.

C. elegans Video Microscopy

The *C. elegans* fluorescent strain ANA090 was cultured using standard protocols and maintained at 25°C. RNAi against *perm-1* was performed by feeding ANA090 L4 larva on HT115 bacteria for 24 hr according to standard protocol (Carvalho et al., 2011), then embryos were mounted with 40 μ M PST-1 and imaged at 561 nm using a Zeiss LSM 710 confocal microscope, using 405 nm and 514 nm laser ROI illuminations to achieve PST photoisomerizations within selected cells (see *Supplemental Information* for further details).

Mouse Cremaster Muscle Experiment

Male C57BL/6 mice at the age of 10–12 weeks were prepared for microsurgery of the cremaster muscle as previously described (Baez, 1973), and 50 μ M PST-1P was added to the superfusion solution. For 40 min, animals were either kept in the dark, or else had the pelvic region illuminated by a 390 nm LED with milliwatt-range light output. Animals were then sacrificed, and the tissue was excised, immunostained, and imaged on a Leica SP5 confocal microscope following standard procedures (Rehberg et al., 2010) (see *Supplemental Information* for further details). Mouse experiments were performed according to German legislation for the protection of animals and approved by the Regierung von Oberbayern, München, Germany, with protocols approved under permits 55.2-1-54-2532-110-12.

SUPPLEMENTAL INFORMATION

Supplemental Information includes Supplemental Experimental Procedures, six figures, and five movies and can be found with this article online at <http://dx.doi.org/10.1016/j.cell.2015.06.049>.

AUTHOR CONTRIBUTIONS

M.B., D.T., and O.T.-S. conceived the study and wrote the manuscript with support from all authors. O.T.-S. designed the PSTs, performed synthesis, analyses, modeling, and made the illumination system; M.B. designed and ran *in vitro* and *in cellulo* experiments; W.N. designed and ran *C. elegans* experiments; M. Reynders performed synthesis; K.N. ran cremaster muscle experiments; P.J., J.H., M.D., M. Rehberg, S.Z., and A.V. supervised experiments.

ACKNOWLEDGMENTS

This paper is dedicated to Dr Michael Bishop, who was an outstanding mentor, and is a lasting inspiration. This project was supported by funds from the European Research Council (ERC Advanced Grant No. 268795 “CARV” to D.T.), the Deutsche Forschungsgemeinschaft (SFB 1032 to D.T., M. Rehberg, and S.Z.), and the Comité de la Recherche Académique, Rhône-Alpes Region,

France (ARC1-Santé 2013 project “PHOTO-CAN” to O.T.-S., M.B., J.H., and P.J.). O.T.-S. and M.B. were additionally supported by fellowships from the ENS-Lyon (Fonds Recherche 2013) and the Canceropôle Lyon Auvergne Rhône-Alpes (CLARA Mobilité Jeunes 2013). W.N. was supported by a French Government PhD fellowship. We thank G. Höfner, L. de la Rosa de la Rosa, P. Mayer, and the CALM platform (LMU), the PLATIM facility (UMS Biosciences, Lyon), H. Bachmeier and A. Gersdorf (LMU Elektrotechnik), and J.-C. Matalier (ENS-Lyon) for help with equipment and assays. We thank V. Small (IMBA, Vienna) for EB3-mCherry plasmid, Caenorhabditis Genetics Center for nematode strains (supported by NIH NCRR), and A. Wainman, R. Zimmermann and A. Haines for electronics advice. O.T.-S. intends to found a startup in 2016/2017 to make photostatins commercially available.

Received: October 24, 2014

Revised: March 6, 2015

Accepted: June 12, 2015

Published: July 9, 2015

REFERENCES

- Applegate, K.T., Besson, S., Matov, A., Bagonis, M.H., Jaqaman, K., and Danuser, G. (2011). plusTipTracker: Quantitative image analysis software for the measurement of microtubule dynamics. *J. Struct. Biol.* **176**, 168–184.
- Baez, S. (1973). An open cremaster muscle preparation for the study of blood vessels by *in vivo* microscopy. *Microvasc. Res.* **5**, 384–394.
- Bhattacharyya, B., Panda, D., Gupta, S., and Banerjee, M. (2008). Anti-mitotic activity of colchicine and the structural basis for its interaction with tubulin. *Med. Res. Rev.* **28**, 155–183.
- Bieling, P., Laan, L., Schek, H., Munteanu, E.L., Sandblad, L., Dogterom, M., Brunner, D., and Surrey, T. (2007). Reconstitution of a microtubule plus-end tracking system *in vitro*. *Nature* **450**, 1100–1105.
- Bisby, R., Botchway, S., Hadfield, J., McGown, A., and Scherer, K.M. February 2013. Multi-Photon Isomerisation Of Combretastatins And Their Use in Therapy. Patent WO2013021208.
- Carvalho, A., Olson, S.K., Gutierrez, E., Zhang, K., Noble, L.B., Zanin, E., Desai, A., Groisman, A., and Oegema, K. (2011). Acute drug treatment in the early *C. elegans* embryo. *PLoS ONE* **6**, e24656.
- Chaitanya, G.V., Steven, A.J., and Babu, P.P. (2010). PARP-1 cleavage fragments: signatures of cell-death proteases in neurodegeneration. *Cell Commun. Signal.* **8**, 31.
- Cushman, M., Nagarathnam, D., Gopal, D., Chakraborti, A.K., Lin, C.M., and Hamel, E. (1991). Synthesis and evaluation of stilbene and dihydrostilbene derivatives as potential anticancer agents that inhibit tubulin polymerization. *J. Med. Chem.* **34**, 2579–2588.
- Dumontet, C., and Jordan, M.A. (2010). Microtubule-binding agents: a dynamic field of cancer therapeutics. *Nat. Rev. Drug Discov.* **9**, 790–803.
- Fehrentz, T., Schönberger, M., and Trauner, D. (2011). Optochemical genetics. *Angew. Chem. Int. Ed. Engl.* **50**, 12156–12182.
- Ghinet, A., Tourneau, A., Rigo, B., Stocker, V., Leman, M., Farce, A., Dubois, J., and Gautret, P. (2013). Synthesis and biological evaluation of fluoro analogues of antimitotic phenstatin. *Bioorg. Med. Chem.* **21**, 2932–2940.
- Gill, J.H., Loadman, P.M., Shnyder, S.D., Cooper, P., Atkinson, J.M., Ribeiro Morais, G., Patterson, L.H., and Falconer, R.A. (2014). Tumor-targeted pro-drug ICT2588 demonstrates therapeutic activity against solid tumors and reduced potential for cardiovascular toxicity. *Mol. Pharm.* **11**, 1294–1300.
- Grossweiner, L. (2005). *The Science of Phototherapy: An Introduction* (Springer).
- Hadfield, J., McGown, A., Mayalar, S., Land, E., Hamblett, I., Gaukroger, K., Lawrence, N., Hepworth, L., and Butler, J. June 2002. Substituted Stilbenes, Their Reactions and Anticancer Activity. Patent WO200250007.
- Hamaguchi, M.S., and Hiramoto, Y. (1986). Analysis of the Role of Astral Rays in Pronuclear Migration in Sand Dollar Eggs by the Colcemid-UV Method. *Dev. Growth Differ.* **28**, 143–156.

- Hooper, A.T., Loganzo, F., May, C., and Gerber, H.-P. (2013). Identification and Development of Vascular Disrupting Agents: Natural Products That Interfere with Tumor Growth. In *Natural Products and Cancer Drug Discovery*, F.E. Koehn, ed. (Springer), pp. 17–38.
- Ibsen, S., Zahavy, E., Wrasidlo, W., Hayashi, T., Norton, J., Su, Y., Adams, S., and Esener, S. (2013). Localized *in vivo* activation of a photoactivatable doxorubicin prodrug in deep tumor tissue. *Photochem. Photobiol.* **89**, 698–708.
- Jordan, A., Hadfield, J.A., Lawrence, N.J., and McGown, A.T. (1998). Tubulin as a target for anticancer drugs: agents which interact with the mitotic spindle. *Med. Res. Rev.* **18**, 259–296.
- Knoll, H. (2003). Photoisomerism of Azobenzenes. In *CRC Handbook of Organic Photochemistry and Photobiology*, F. Lenci and W. Horstpool, eds. (CRC Press).
- Lin, C.M., Singh, S.B., Chu, P.S., Dempcy, R.O., Schmidt, J.M., Pettit, G.R., and Hamel, E. (1988). Interactions of tubulin with potent natural and synthetic analogs of the antimitotic agent combretastatin: a structure-activity study. *Mol. Pharmacol.* **34**, 200–208.
- Maurer, S.P., Fourniol, F.J., Bohner, G., Moores, C.A., and Surrey, T. (2012). EBs recognize a nucleotide-dependent structural cap at growing microtubule ends. *Cell* **149**, 371–382.
- Nicoletti, I., Migliorati, G., Pagliacci, M.C., Grignani, F., and Riccardi, C. (1991). A rapid and simple method for measuring thymocyte apoptosis by propidium iodide staining and flow cytometry. *J. Immunol. Methods* **139**, 271–279.
- Ohsumi, K., Nakagawa, R., Fukuda, Y., Hatanaka, T., Morinaga, Y., Nihei, Y., Ohishi, K., Suga, Y., Akiyama, Y., and Tsuji, T. (1998). Novel combretastatin analogues effective against murine solid tumors: design and structure-activity relationships. *J. Med. Chem.* **41**, 3022–3032.
- Peterson, J.R., and Mitchison, T.J. (2002). Small molecules, big impact: a history of chemical inhibitors and the cytoskeleton. *Chem. Biol.* **9**, 1275–1285.
- Pettit, G.R., and Rhodes, M.R. July 2009. Synthesis of combretastatin A-4 prodrugs and trans-isomers thereof. US Patent 7557096.
- Pettit, G.R., Singh, S.B., Hamel, E., Lin, C.M., Alberts, D.S., and Garcia-Kendall, D. (1989). Isolation and structure of the strong cell growth and tubulin inhibitor combretastatin A-4. *Experientia* **45**, 209–211.
- Rehberg, M., Praetner, M., Leite, C.F., Reichel, C.A., Bihari, P., Mildner, K., Duhr, S., Zeuschner, D., and Krombach, F. (2010). Quantum dots modulate leukocyte adhesion and transmigration depending on their surface modification. *Nano Lett.* **10**, 3656–3664.
- Saotome, K., Morita, H., and Umeda, M. (1989). Cytotoxicity test with simplified crystal violet staining method using microtitre plates and its application to injection drugs. *Toxicol. In Vitro* **3**, 317–321.
- Stanton, R.A., Gernert, K.M., Nettles, J.H., and Aneja, R. (2011). Drugs that target dynamic microtubules: a new molecular perspective. *Med. Res. Rev.* **31**, 443–481.
- Strome, S., and Wood, W.B. (1983). Generation of asymmetry and segregation of germ-line granules in early *C. elegans* embryos. *Cell* **35**, 15–25.
- Tahir, S.K., Kovar, P., Rosenberg, S.H., and Ng, S.-C. (2000). Rapid colchicine competition-binding scintillation proximity assay using biotin-labeled tubulin. *Biotechniques* **29**, 156–160.
- Thorn-Seshold, O., Vargas-Sanchez, M., McKeon, S., and Hasserodt, J. (2012). A robust, high-sensitivity stealth probe for peptidases. *Chem. Commun. (Camb.)* **48**, 6253–6255.
- Thorn-Seshold, O., Borowiak, M., Hasserodt, J., and Trauner, D. (2014). Azoaryls as reversibly modulatable tubulin inhibitors (PCTFR2014000095).
- Tozer, G.M., Kanthou, C., Parkins, C.S., and Hill, S.A. (2002). The biology of the combretastatins as tumour vascular targeting agents. *Int. J. Exp. Pathol.* **83**, 21–38.
- Tron, G.C., Pirali, T., Sorba, G., Pagliai, F., Busacca, S., and Genazzani, A.A. (2006). Medicinal chemistry of combretastatin A4: present and future directions. *J. Med. Chem.* **49**, 3033–3044.
- Velema, W.A., Szymanski, W., and Feringa, B.L. (2014). Photopharmacology: beyond proof of principle. *J. Am. Chem. Soc.* **136**, 2178–2191.
- Wu, Y.I., Frey, D., Lungu, O.I., Jaehrig, A., Schlichting, I., Kuhlman, B., and Hahn, K.M. (2009). A genetically encoded photoactivatable Rac controls the motility of living cells. *Nature* **461**, 104–108.
- Wühr, M., Tan, E.S., Parker, S.K., Detrich, H.W., 3rd, and Mitchison, T.J. (2010). A model for cleavage plane determination in early amphibian and fish embryos. *Curr. Biol.* **20**, 2040–2045.

Supplemental Figures

Cell

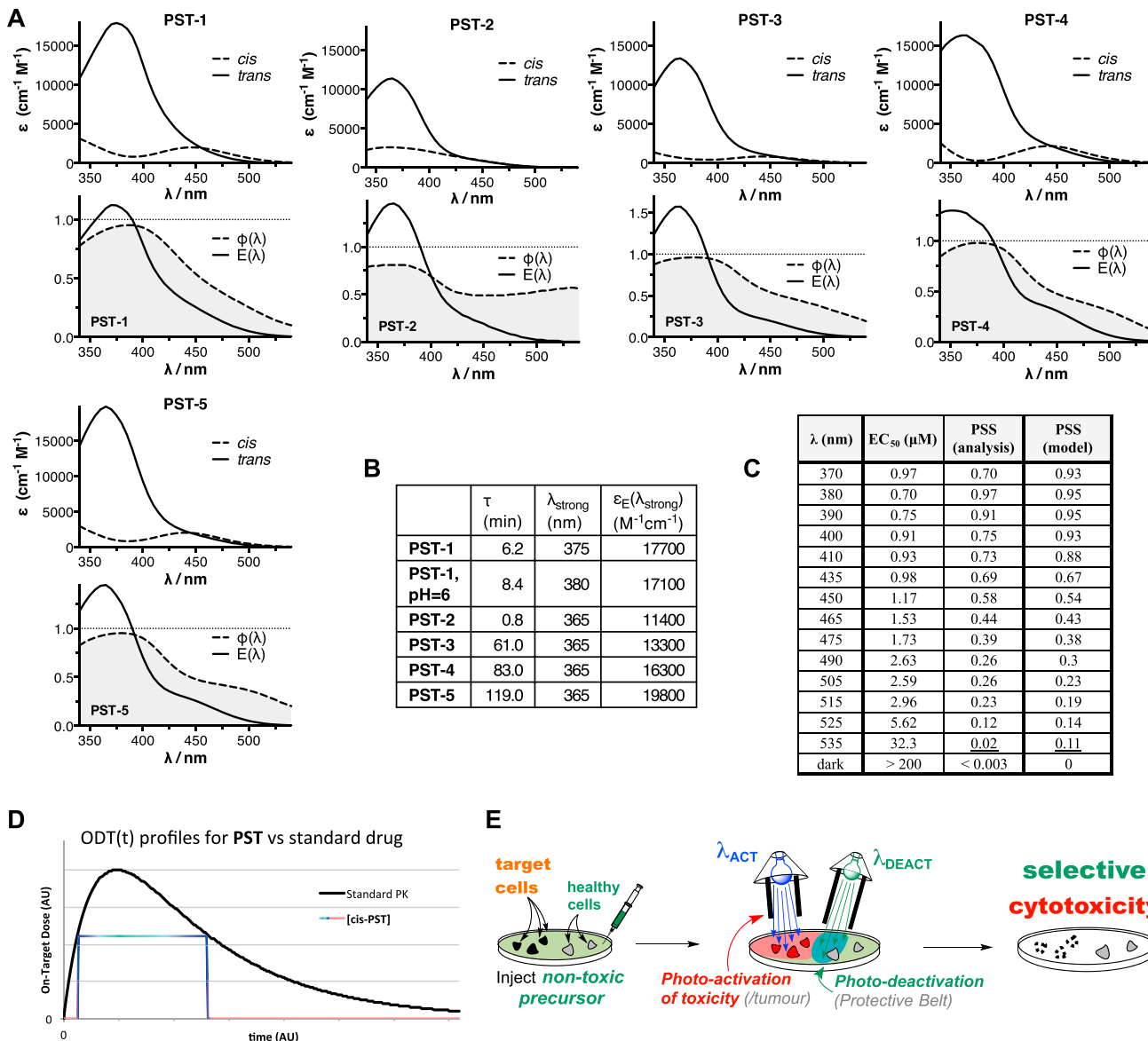


Figure S1. Full Photocharacterization of the PSTs, and Design and Use of the “Disco” Photoswitching System, Related to Figure 1

(A) Absorption spectra of *trans* (solid lines) and *cis* (dotted lines) isomers of the non-prodrug PSTs (PST-1 – PST-5) in water-acetonitrile solution (upper), and their $\phi(\lambda)$ (dotted lines) and $E(\lambda)$ (solid lines) (lower), determined as per supplementary sections B.1-B.2. (B) τ , λ_{strong} and $\epsilon_E(\lambda_{\text{strong}})$ determined as per supplementary sections B.1 and B.4. (C) Summary results from MTT assay in HeLa cells after 44 hr incubation with PST-1P under lighting with different wavelengths but constant pulse timings. Results illustrate the predictable dependency of observed cytotoxicity upon wavelength. That the observed cytotoxicity is governed by the underlying [cis-PST-1] with an EC₅₀ of about 0.68 μ M in this assay, is supported since the back-calculated PSS_{exp}(λ) values [PSS (analysis)] at different wavelengths are reliably correlated with the calculated $\phi(\lambda)$ values from Figure S1A [PSS (model)]. (D) Model comparing an on-target dose profile OTD(t) which can be established for a [cis]-PST to the typical PK pattern of an always-on drug. (E) Two-wavelength active photoisomerization concept for in vivo spatial restriction of photoswitchable cytotoxins to a specific zone, illustrating the importance of assaying the toxic regime (left zone), the rescue protocol (overlap zone), green-only illumination (central zone) and the dark regime (right zone) as the limiting cases for the cytotoxicity experienced in each area.

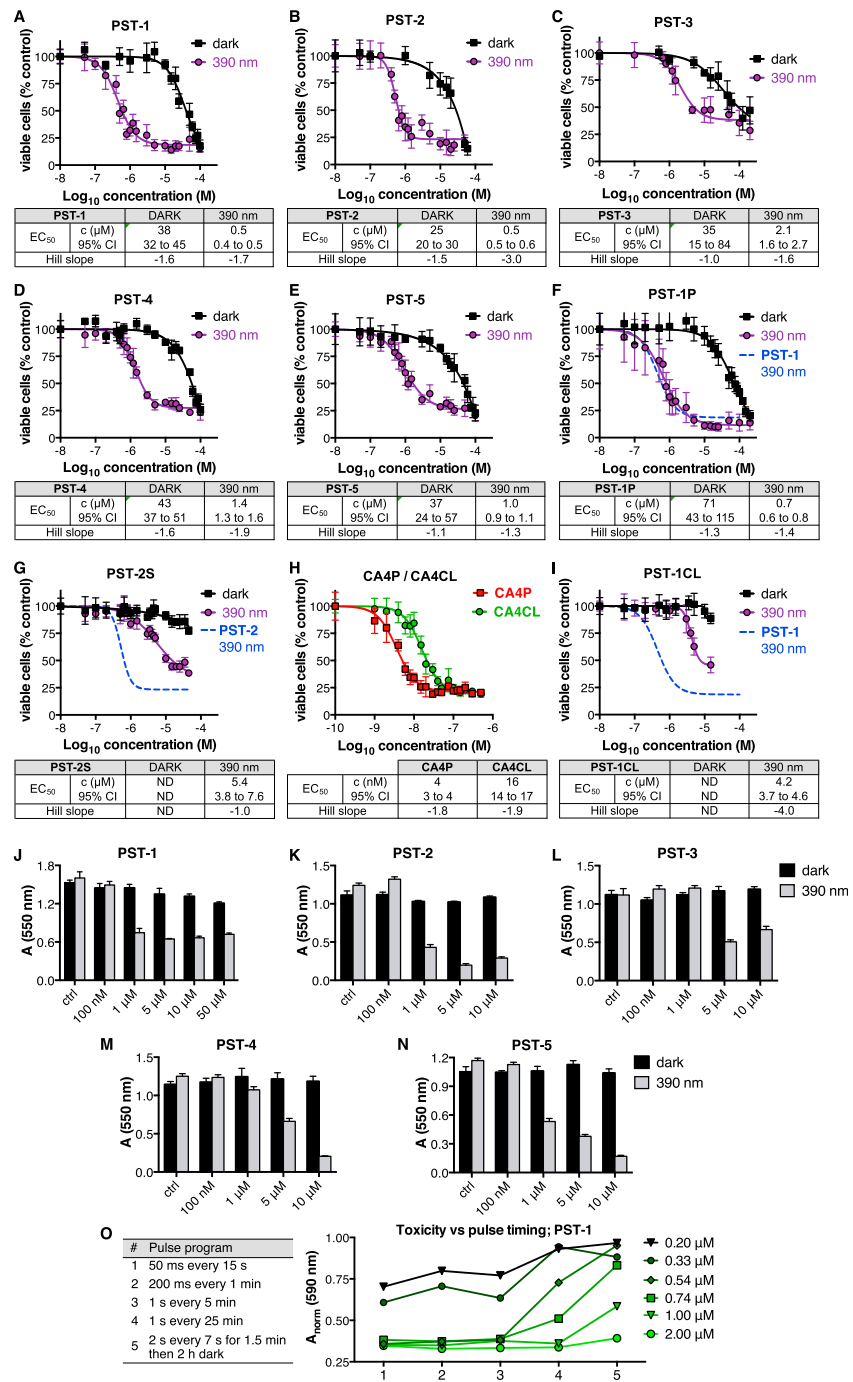
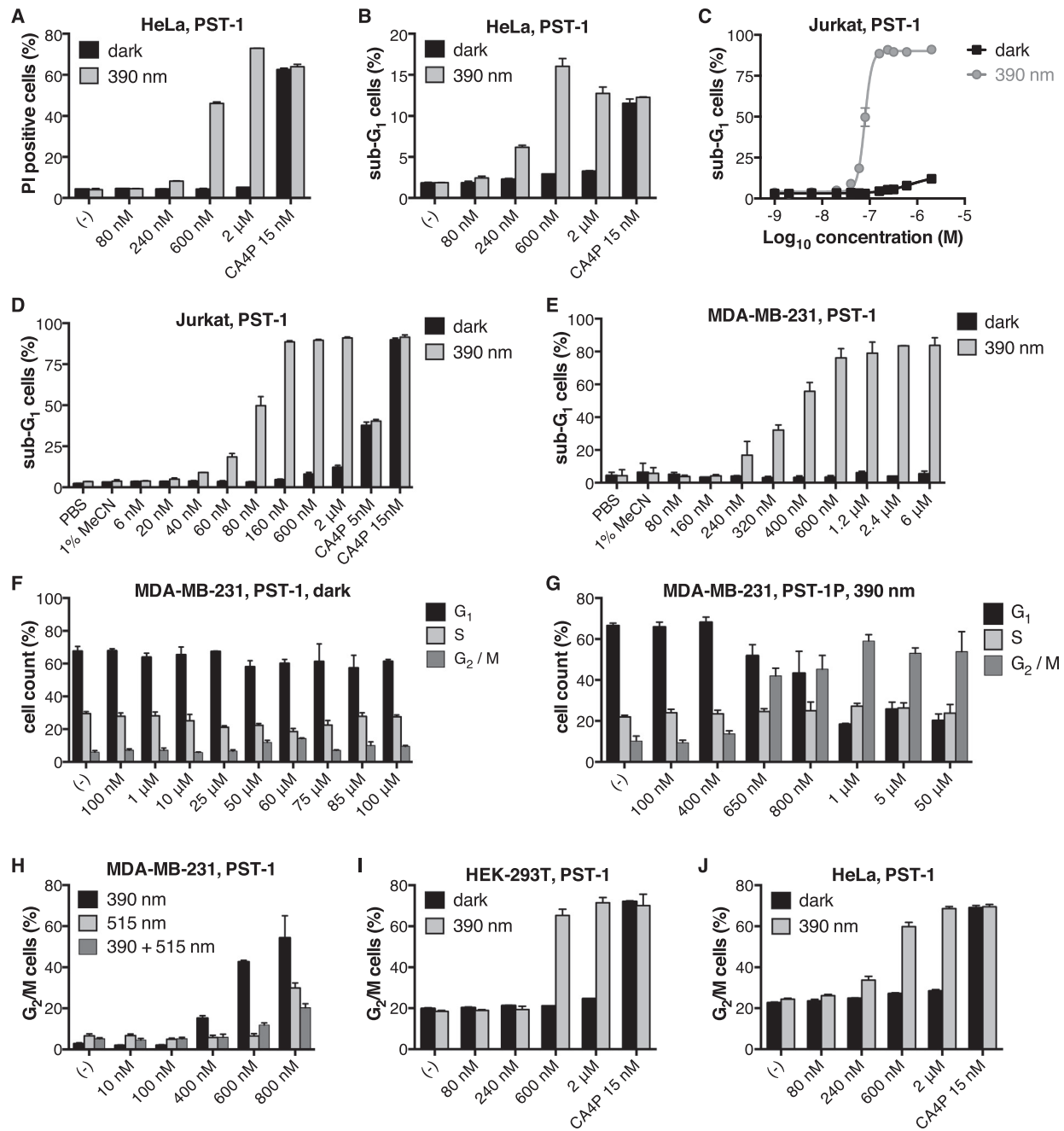


Figure S2. Full Data for the Cytotoxicity Assays of the PSTs, Related to Figure 2

(A-I) Cytotoxicity profiles of all PSTs in the dark and upon illumination with 390 nm light under the toxic regime, assessed in MDA-MB-231 cells by crystal violet staining after 48 hr. Profiles of PST prodrugs PST-1P, PST-1CL and PST-2S are presented in comparison to the toxic regime profiles of their active cores. The profile of peptidase-triggered stilbene prodrug CA4CL is compared to that of CA4P as a control of the cyclisation prodrug strategy. Data were summarized in Figure 2B. (J-N) The light-dependent cytotoxicity of PSTs as shown by MTT assay in HeLa cells after 45 hr incubation with PSTs under dark or toxic regimes (vertical axis is the formazan absorption readout); the assay with PST-1 used 1% MeCN as cosolvent, the other experiments used 1% DMSO. (O) MTT assay in HEK293T cells after 72 hr incubation with PST-1 under different lighting pattern timings at 390 nm. Results illustrate the dependency of observed cytotoxicity upon the specific pulse program as opposed to the time-averaged photon flux (e.g., compare programs 3-5). Results are given as mean ± SD.

**Figure S3. Data for Assays of Cell-Cycle and Cell Death Parameters, Related to Figure 3**

(A) PST-1 induces cell membrane permeability in HeLa cells in a light-dependent manner; cells were treated for 70 hr with PST-1 under the dark and toxic regimes, and the percentage of PI positive cells in the total amount of cells determined. (B-E) PST-1 induces dose-dependent nuclear fragmentation in HeLa (B), Jurkat (C and D), and MDA-MB-231 cells (E) under the toxic regime only. Dose response curve for Jurkat cells (C) was fitted based on the raw data partially presented in (D), for which an EC₅₀ = 79 nM was determined for PST-1 upon 390 nm illumination. Graph (E) represents data corresponding to dose response curves shown in Figure 3B. (F–J) Light-dependent effects of PSTs on cell cycle. (F) When kept in the dark, PST-1 shows no influence on cell-cycle arrest even up to 100 μM (MDA-MB-231 cells, 48 hr of dark PST-1 treatment). (G) Prodrug PST-1P reproduces the cell-cycle arrest seen for PST-1 when illuminated with blue light; compare to Figure 3E. (H) The rescue lighting regime reduces the effect on cell-cycle arrest exerted by PST-1 relative to what is experienced when only the 390 nm pulse component is used. Cells were pulsed with 390 nm light followed by 515 nm pulse that greatly decreased the effective *cis*-PST-1 concentration and contributed to reduction in G₂/M arrest. (I–J) PST-1 provokes light-dependent G₂/M phase arrest in HEK293T (I) and HeLa (J) cells. Results are given as mean ± SD.

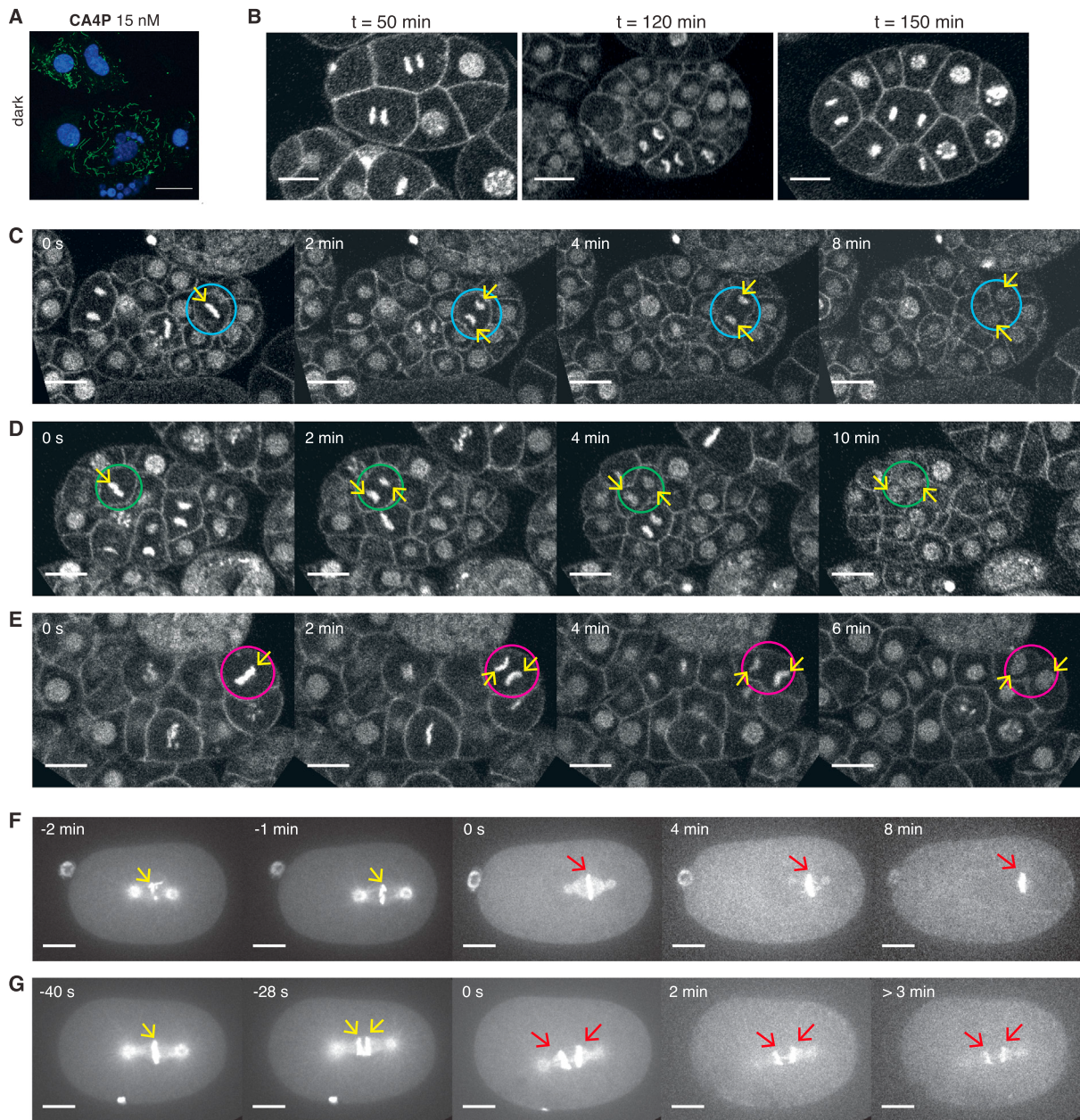


Figure S4. Cell and *C. elegans* Microscopy Studies, Related to Figures 4 and 6

(A) Representative confocal microscope image showing microtubule network following CA4P treatment (15 nM final concentration). This positive control accompanies immunofluorescence microscopy images from Figure 4C (α -tubulin is shown in green, nuclei are stained blue, white bar corresponds to a scale of 20 μ m). (B-E) Controls for lighting parameters in the *C. elegans* experiments. Images show representative *C. elegans* embryos expressing mCherry::H2B and mCherry::PH, permeabilized and bathed in M9 buffer with or without 40 μ M PST-1; all scale bars, 10 μ m. (B) Embryos, incubated for 50 min (left), 120 min (middle), and 150 min (right), with PST-1 but without photoisomerization illumination, show normal mitotic progression. (C and D) The encircled cell has been illuminated for 2 to 5 ms every 30 s, using the 405 nm laser only (blue circle, C) or with twin pulses of 405 nm then 514 nm lasers (green circle, D), but without PST-1, showing no disruption of mitosis due to lighting protocol only. (E) Embryos incubated in 40 μ M PST-1; the encircled cell has been illuminated for 2 to 5 ms every 30 s using the 514 nm laser, without giving mitotic arrest. (F-G) Positive control timelapse sequences showing *C. elegans* embryos expressing histone and tubulin fused to GFP, under treatment with the known MT inhibitor, colchicine. Embryos were permeabilized and bathed in M9 buffer, and colchicine was added at t = 0 s. (F) Colchicine added during metaphase. (G) Colchicine added during anaphase. Stationary chromosomes and moving chromosomes are shown with red and yellow arrows, respectively. Scale bar, 10 μ m.

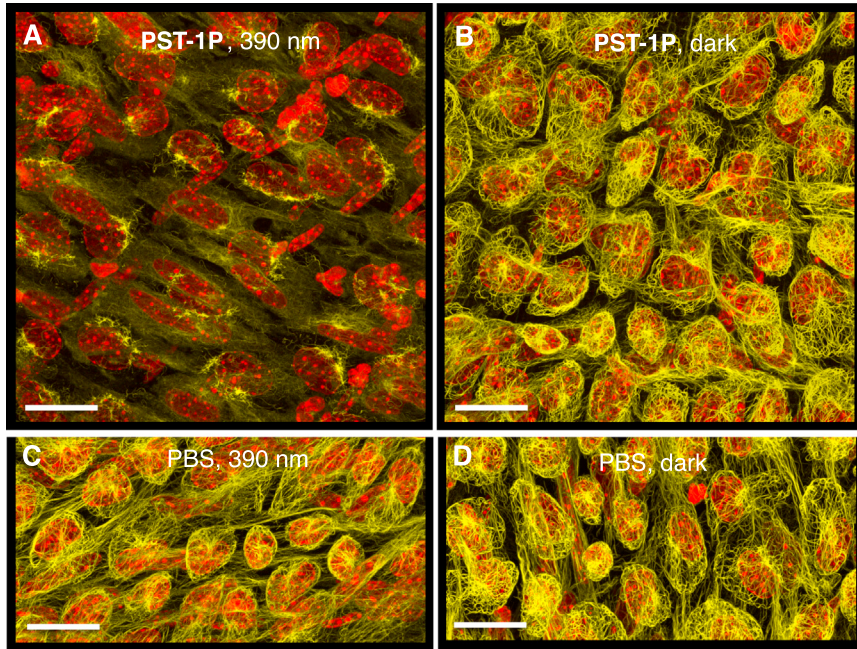


Figure S5. Expanded Images of the Mouse Cremaster Muscle Experiments, Related to Figure 6

Immunofluorescence images of MT structure after treatment with 50 μ M PST-1P applied *in vivo* to mouse cremaster tissue shows total MT disruption under 390 nm illumination (A), but the dark regime result (B) is identical to negative controls (C-D) showing no disruption. 3D rendered z-stacks of optical sections of 30 μ m total thickness are shown. Tubulin staining is shown in yellow, nuclei are shown in red. Scale bars, 20 μ m.

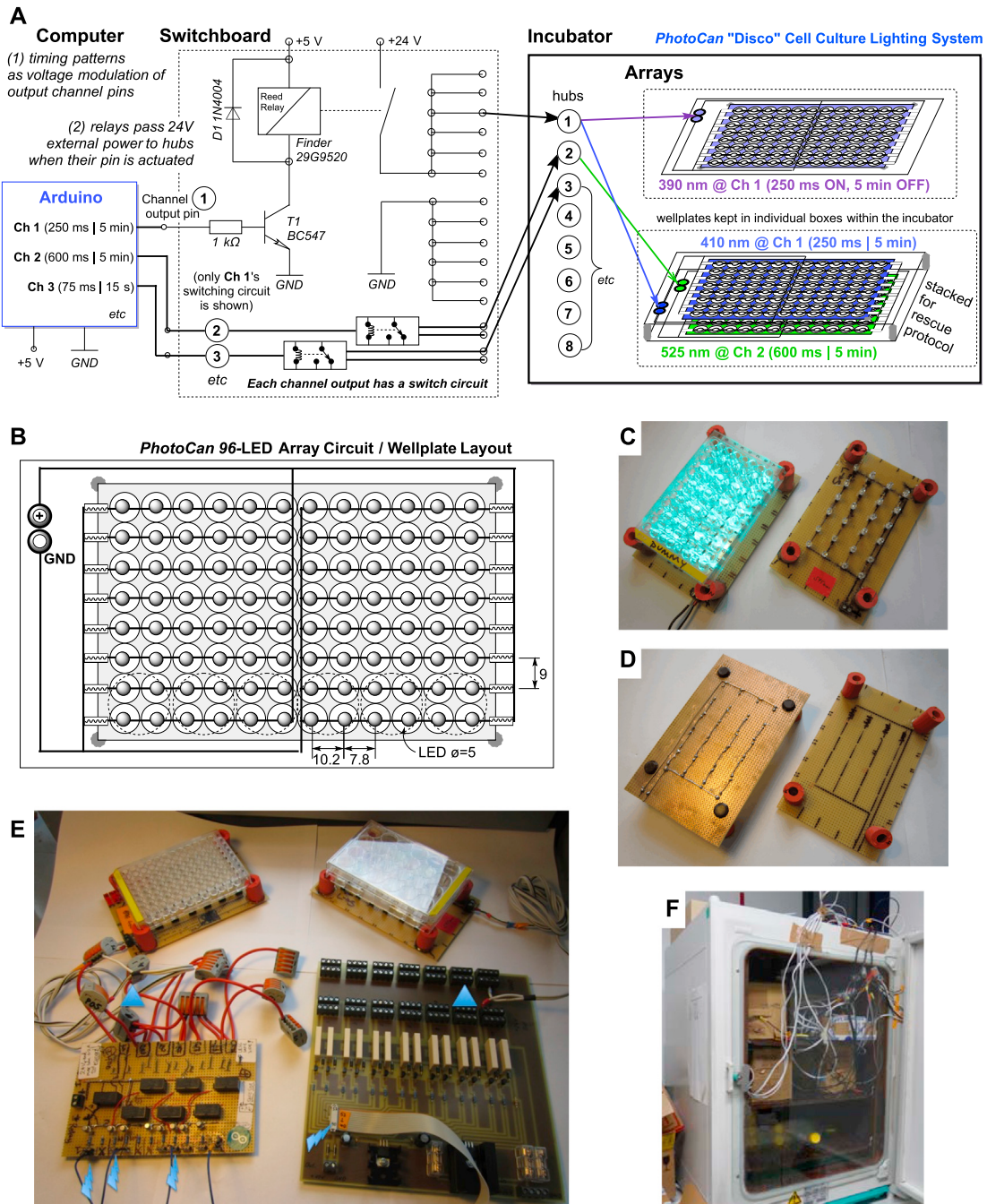


Figure S6. “Disco” Computer-Controlled LED-Based Automatic Lighting System for Cell Culture Experiments; Related to Figure 2

(A) Schematic overview of the Disco system including circuit diagram for a switchboard operated by the Arduino microcomputer. The Arduino (blue, at left) sends e.g., 3 input timing sequences through connectors to the switchboard (dotted, center), which powers the corresponding LED-arrays with those timing sequences (in the incubator, right). (B) 96-array layout (dimensions in mm). (C and D) 24-arrays under construction: (C) 24-arrays completed; at left: with wellplate in place and powered, at right: without well plate, to show geometry; (D) at left: underside showing soldering pattern, at right: top side showing layout. (E) Switchboards used in this work. At left, self-built 7-channel system with limit of ~80 separate 24-arrays and variable voltage tolerance; at right, a machined 14-channel system for higher current and fixed voltage (limit 400 separate 96-arrays); power supplies and the Arduino are out of frame. (F) Massively parallel Disco assay in practice: Arduino, powerpack and switchboard sit on top of the incubator; leads feed into the incubator to power the LED-arrays which are contained inside cardboard boxes to limit wavelength crosstalk. For further details see Appendix 2.

Cell

Supplemental Information

Photoswitchable Inhibitors of Microtubule Dynamics

Optically Control Mitosis and Cell Death

Malgorzata Borowiak, Wallis Nahaboo, Martin Reynders, Katharina Nekolla, Pierre Jalinot, Jens Hasserodt, Markus Rehberg, Marie Delattre, Stefan Zahler, Angelika Vollmar, Dirk Trauner, Oliver Thorn-Seshold

Supplemental Information

This paper is dedicated to Dr Michael Bishop, who was an outstanding mentor, and is a lasting inspiration.

Authorship Statement: Following the ICMJE guidelines, the authors declare their roles in this work as follows: **M. Borowiak**: proposed, designed, ran and analysed cell biology experiments and *in vitro* assays; wrote the cell biology portions of the manuscript; **W. Nahaboo**: designed and ran *C. elegans* microscopy experiments; wrote the *C. elegans* portion of the manuscript; **M. Reynders**: performed chemical synthesis; **K. Nekolla**: ran mouse cremaster microscopy experiments and wrote the mouse cremaster portion of the manuscript; **P. Jalinot**: supervised initial cell biology evaluation of **CA4CL**; **J. Hasserodt**: supervised synthesis of **CA4CL**; **M. Rehberg**: designed and supervised mouse cremaster microscopy experiments; **M. Delattre**: designed and supervised *C. elegans* experiments; **S. Zahler**: supervised *in cellulo* immunofluorescence microscopy; **A. Vollmar**: supervised cytotoxicity assays and cell cycle analysis; **D. Trauner**: supervised syntheses of **Photostatins** and *in vitro* and *in cellulo* assays, and proposed further applications; **O. Thorn-Seshold**: invented the design of **Photostatins** as light-controllable cytotoxins; proposed, designed and performed syntheses and photochemical analyses; designed, built and programmed the LED-array lighting system; wrote the design, chemistry, photocharacterisation portions of the manuscript. **MB**, **DT** and **OTS** conceived the study; coordinated research; and wrote the manuscript with support from all authors.

Thanks: The authors express their gratitude for project financial support from the European Research Council (ERC Advanced Grant No. 268795 “CARV” to DT), the Deutsche Forschungsgemeinschaft (SFB 1032 funding to KN, M. Rehberg, SZ, and DT), and the Comité de la Recherche Académique, Rhône-Alpes, (funding call ARC1-Santé 2013, project PHOTO-CAN to OTS, MB, JH and PJ); and to the Canceropôle Lyon Auvergne Rhône-Alpes for facilitating collaborations (CLARA Mobilité Jeunes 2013 awarded to MB and OTS). We thank Herbert Bachmeier and Axel Gersdorf (LMU Elektrotechnik) for prototyping manual LED arrays and expanding the computerised LED-array cell culture system; Dr Georg Höfner (LMU) for help with radioligand assays; Dr. Jean-Christophe Mulatier (ENS-Lyon) for synthesis of combretastatin A-4; Peter Mayer for X-ray structure determination (LMU); the PLATIM (UMS Biosciences Lyon) and CALM (LMU) imaging facilities; L. de la Osa de la Rosa for cell culture assistance (LMU); V. Small (IMBA, Vienna) for EB3-mCherry plasmid; and the Caenorhabditis Genetics Center (supported by the NIH NCRR) for nematode strains. OTS and MB are grateful to the ENS-Lyon Fonds Recherche 2013 for additional financial support (salary grant). WN was supported by a French Government PhD fellowship. OTS thanks Bob Pettit for inspiration; Andrew Haines for sage advice on electrical circuit design; and Robert Zimmerman and Anthony Wainman for discussions on the design of the LED system.

Table of Contents

Part A: Chemical Synthesis and Characterisation	5
Conventions	5
Standard Procedures	6
PST-1: “azocombretastatin A-4”; route using TBS protecting group.....	8
PST-1: alternative route using tosyl protecting group	12
PST-2: meta-amino analogue (azoombrabulin’s active core).....	13
PST-3: meta-fluoro analogue	15
PST-4: meta-hydro analogue.....	16
PST-5: meta-hydro, ortho-fluoro analogue	17
PST-1P: “azo-CA4P”, a water-soluble phosphate prodrug of PST-1	18
PST-2S: “azoombrabulin” – a water-soluble serine prodrug of PST-2	20
PST-1CL and CA4CL : peptide prodrugs of PST-1 and CA4	21
Part B: Photocharacterisation <i>in vitro</i>	26
Spectrophotometry equipment.....	26
B.1: <i>trans</i> - and <i>cis</i> - absorption spectra	26
B.2: Calculated $\phi(\lambda)$ and $E(\lambda)$	27
B.3: Reversible <i>trans</i> ↔ <i>cis</i> photoisomerisation	27
B.4: Thermal <i>cis</i> → <i>trans</i> reversion halflives.....	28
ASSAYS <i>in vitro</i>, <i>in cellulo</i>, & <i>in vivo</i>	
Materials and Methods	28
Safety Precautions	28
Biochemical Assays <i>in vitro</i>	28
Cell Culture.....	29
Cell Biology Assays	31
<i>C. elegans</i> experiments	34
Mouse cremaster muscle experiments	34
RESULTS	
Part C: Cell Biology	36
C.1: Toxicity dependency on pulse frequency and illumination wavelength.....	36
C.2. Photoactuated cytotoxicity of PSTs	38
C.3: G ₂ /M phase cell cycle arrest (PST-1 and PST-1P)	38
C.4: Membrane permeability induced by PST-1	39
C.5: Nuclear fragmentation (PST-1)	39
C.6: IF staining of tubulin in fixed cells.....	39
Part D: <i>C. elegans</i> experiments	40
Part E: Mouse cremaster muscle experiment.....	41
Appendix 1: Photoisomerisation parameter space	42
Rationale for the quantities to be measured by <i>in vitro</i> studies:.....	42
Defining and determining $\varepsilon_E(\lambda)$ and $\varepsilon_Z(\lambda)$, PSS(λ), τ , and $E(\lambda)$:.....	44
A note on photoisomerisations at wavelengths above 530 nm.....	46

Appendix 2: PhotoCan “Disco” cell culture lighting system.....	47
Disco system – in practice	47
Disco system – Switchboards	47
Disco system – LED arrays	48
Disco system – Arduino program 1	49
Disco system – Arduino program 2	51
Appendix 3: PST design and handling.....	54
Choice of Prodrug Strategies for PSTs.....	54
Solubility and Handling.....	55
Appendix 4: Photopharmacology: design, rationale, applications	57
From Principles to Biological Assay Design: Rationale	57
<i>cis</i> -activity, dual targeting and other advantages for spatial precision.....	58
Temporal modulation of photopharmaceuticals	59
Supplemental References	62

Part A: Chemical Synthesis and Characterisation

Conventions

Diazene geometry and nomenclature: Azobenzenes are drawn by default in their Z-isomeric form in these Part A synthetic descriptions. This is intended to enable easier comparison with the SAR literature of their isosteric antitubulin stilbenes and stilbenoids such as the combretastatins. However, this should be understood to imply either or both of the E & Z forms constituting a given sample depending on light exposure, therefore by default they are also named without E/Z-designations.

Abbreviations: The following nonstandard abbreviations are used: Hx – distilled isohexanes, Cy – cyclohexane, EA – ethyl acetate, peth – petroleum ether (40-60° fraction), DCM – dichloromethane, TFA – 2,2,2-trifluoroacetic acid, Et – ethyl, Ac – acetyl, Me – methyl, MeCN – acetonitrile, iPr – isopropyl, iPen – *iso*-pentyl, Bu – butyl, DMAP – 4-(dimethylamino)pyridine, DBU – 1,8-diazabicycloundec-7-ene, DMAP – 4-dimethylaminopyridine, iPenONO – isopentyl nitrite, HOEt – 1-hydroxybenzotriazole, DCC – dicyclohexylcarbodiimide, DMF – dimethylformamide, brsm – based on recovered starting material, TBS – *tert*-butyldimethylsilyl, PBS – phosphate buffer saline, Ts or tosyl – *para*-toluenesulfonyl, Boc – *tert*-butoxycarbonyl, Ser – L-serinyl, Leu – L-leucyl, **CA4** - combretastatin A-4, **CA4P** – combretastatin A-4 phosphate ester disodium salt, brsm – based on recovered starting material, wt% - percentage by weight.

Reagents and Conditions: Unless stated otherwise, (1) all reactions and characterisations were performed with unpurified, undried, non-degassed solvents and reagents, used as obtained, under closed air atmosphere without special precautions; (2) “hexane” used for chromatography was distilled from commercial crude isohexane fraction on rotavap; (3) “column” and “chromatography” refer to flash column chromatography, which was performed on Merck silica gel Si-60 (40-63 µm); (4) procedures and yields are unoptimised; (5) yields refer to isolated chromatographically and spectroscopically pure materials, corrected for residual solvent content; (6) all eluent and solvent mixtures are given as volume ratios unless otherwise specified, thus “1:1 Cy:EA” indicates a 1:1 mixture (by volume) of cyclohexane and ethyl acetate.

Thin-layer chromatography (TLC) was run on 0.25 mm Merck silica gel plates (60, F-254). UV light (254 nm) was used as a visualising agent, and standard TLC dips based on p-anisaldehyde (Anis), Hanessian’s cerium ammonium molybdate formulation (Han), 0.6% methanolic FeCl₃ (FeCl₃), basic KMnO₄ (KMnO₄), phosphomolybdic acid (PMA), Dragendorff’s reagent (Drag), vanillin (Van) and ninhydrin (Nin) - followed by heating where necessary - were used as developing agents. R_f values were usually determined in hexane:ethyl acetate (Hx:EA) or cyclohexane:ethyl acetate (Cy:EA) eluents. TLC characterisations are thus abbreviated as per (R_f = 0.09 on 6:1 Hx:EA, Anis).

NMR: Standard NMR characterisation was by ¹H- and ¹³C-NMR spectra. Known compounds were checked against literature data and their spectral analysis is not detailed unless necessary.

Spectrometers used were Bruker DPX 200 (200 MHz & 50 MHz for ^1H and ^{13}C respectively), Varian VNMRS 300 (300 MHz, 75 MHz and 282 MHz for ^1H , ^{13}C and ^{19}F respectively), Bruker Ascend 400 (400 MHz & 100 MHz for ^1H and ^{13}C respectively), Bruker AVANCE 500 (500 MHz & 125 MHz for ^1H and ^{13}C respectively), as indicated, at 300K. Where not indicated otherwise, the NMR solvent was CDCl_3 . Chemical shifts (δ) are reported in ppm calibrated to residual non-perdeuterated solvent as an internal reference (Gottlieb et al., 1997). The following peak descriptions are used: singlet (s), doublet (d), triplet (t), quartet (q), multiplet (m), broad (br); apparent multiplicities (resolved by 2D experiments or determined by complete spectral assignment) are denoted by a tilde, eg. “doublet of doublets, appears as a triplet with apparent coupling constant $J = 3 \text{ Hz}$ ” is denoted ($\sim\text{t}$, 3 Hz).

Mass Spectra: Unit mass measurements were performed on AGILENT 1100 SL and AGILENT 1200 SL coupled LC-MS systems with ESI mode ionisation, with binary eluent mixtures of water-acetonitrile, with the water containing sodium/ammonium formate or formic acid. Both direct injection of the sample (abbreviated DIMS) and LCMS were performed as specified. For LCMS, standard run conditions used an Eclipse Plus $3.5 \mu\text{m} / 4.6 \times 100 \text{ mm}$ C18 column, maintained at 25°C , with a 2 mL/min flow rate, whereby the solvent front eluted at $t_{\text{ret}} = 0.76 \text{ min}$. A linear gradient of eluent composition from $90:10 \rightarrow 10:90$ water:acetonitrile was applied over the first 4.5 min, then 10:90 maintained until all peaks of interest had been observed (typically a further 3 min). Ion peaks from (positive/negative mode) are reported as (+/-) with units Th (m/z). Thus “LCMS(+): $t_{\text{ret}} = 5.60 \text{ & } 5.82 \text{ min, each } 419 \text{ Th} = [\text{MH}]^+$ ” indicates LCMS under the standard run conditions with ESI ionisation giving two positive ion peaks eluting at 5.60 and 5.82 min retention times, each at m/z = 419 Th, attributed as the protonated molecular ion. Unless stated otherwise, all reported peaks in the positive mode were $[\text{MH}]^+$ peaks, and all observed peaks in the negative mode were $[\text{M}-\text{H}]^-$ peaks. HRMS was carried out by the Service Central d’Analyse du CNRS, Solaize, France, and by the Zentrale Analytik of the LMU, Munich using ESI or EI ionisation as specified.

Standard Procedures

Where Standard Procedures were used in synthesis, unless stated otherwise, the amounts of reactants/reagents employed were implicitly adjusted to maintain the same molar ratios as in the given Procedure, and no other alterations from the Standard Procedure (eg reaction time, extraction solvent, temperature) were made, unless stated otherwise.

Standard Procedure A: Diazo Coupling using isopentyl nitrite

To the aniline (1 mmol) were added MeOH (5 mL) and conc. HCl (0.25 mL), and the mixture cooled in an icebath. A solution of isopentyl nitrite (1.02 mmol) in methanol (0.6 mL) was added dropwise and the reaction stirred for 30 min in the cold. A cold solution of the phenol (1.05 mmol) in methanol (2 mL) and NaOH (2.0 M, 1.8 mL) was prepared, and to it was added the solution of the diazonium,

dropwise over 1 minute. After typically 30 minutes stirring in the cold, the pH was adjusted to 7 with phosphate buffer, chloroform (10 mL) was added, and the aqueous phase was extracted with CHCl₃ (2×10 mL). The combined organic layers were washed with water (15 mL) and brine (10 mL), dried on Na₂SO₄, filtered and concentrated. Chromatography with a Hx:EA gradient was used to separate the *para*-phenolic azobenzene product which typically ran as a single isomer during chromatography.

Standard Procedure B: Phenol methylation in acetone

To the phenol (1 mmol) were added K₂CO₃ (3 mmol), technical grade acetone (10 mL), and MeI (2 mmol), and the mixture stirred at RT for 2-12 h, until TLC showed satisfactory conversion. TLC often separated the E/Z azobenzene isomers, with the major spot being the faster-running E isomer; the Z isomer typically appeared at near-identical R_f to that of the phenol starting material. The volatiles were evaporated on the rotavap, then the crude mixture was separated by chromatography with a Hx:EA gradient. Since the *para*-O-methylated E and Z product isomers typically were separable by chromatography, the crude product could be kept in the dark overnight and protected from light during loading and chromatography (eg wrapping the column with aluminium foil) to ensure cleaner separation of the desired product (as the E isomer) from other impurities, though this was typically not necessary.

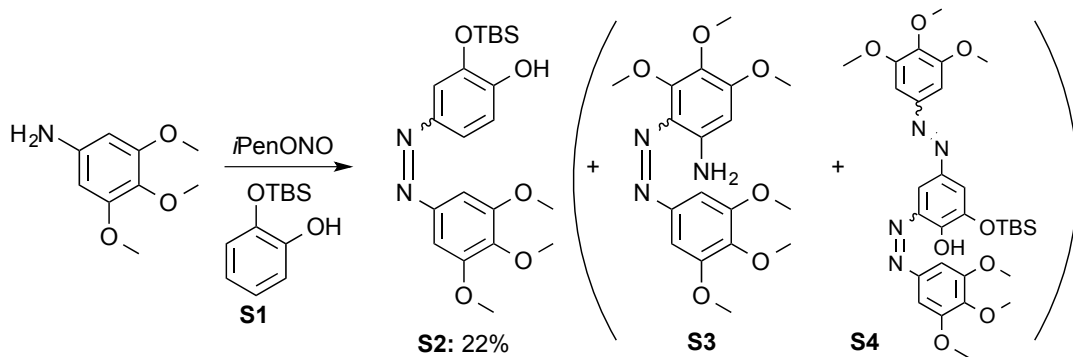
Standard Procedure C: Phenol methylation using MeI and Ag₂CO₃ in toluene

To the phenol (1 mmol) in a screw-cap pressure tube were added toluene (6 mL), Ag₂CO₃ (1 mmol, supported on Celite or not), and MeI (1.5 mmol). The tube was sealed, protected from light, and the reaction heated to 110°C overnight with stirring. After cooling, the crude reaction mixture was filtered, the residue washed with chloroform (2 mL), and the combined filtrates concentrated and separated on column as for Standard Procedure B.

Standard Procedure D: Diazo Coupling using HNO₂

The aniline (1 mmol) was dissolved in aqueous HCl (1.2 M, 0.95 mL), diluted with water (3 mL) and cooled in an icebath while a cold aqueous solution of NaNO₂ (0.85 M, 1 mL, 1.2 eq) was added dropwise with stirring. Stirring in the icebath was continued for 6 min, then a cold aqueous solution of NaOH (1.0 M, 0.65 mL) was added dropwise followed by a cold solution of the phenol (1.05 mmol) in THF (4 mL). After four minutes stirring, the pH was adjusted to 8 with phosphate buffer, and stirring in the cold continued for 5 min before chloroform (4 mL) was added. The aqueous phase was extracted with CHCl₃ (2×8 mL), then the combined organic layers were washed with water (12 mL) and brine (10 mL), dried on Na₂SO₄, filtered and concentrated. Chromatography with a Hx:EA gradient was used to separate the azobenzene product; significant quantities of byproducts were usually obtained.

PST-1: “azocombretastatin A-4”; route using TBS protecting group



2-((*tert*-butyldimethylsilyl)oxy)phenol (S1**)**

Catechol (580 mg, 5.27 mmol) was added to a stirred solution of TBSCl (658 mg, 4.4 mmol) and imidazole (850 mg, 11.6 mmol) in DMF (15 mL), then NEt₃ (1 mL, 7.5 mmol) was added and a precipitate formed. The reaction mixture was stirred overnight, concentrated on the rotavap, and partitioned between water (75 mL) and ethyl acetate (25 mL). The aqueous phase was extracted twice with ethyl acetate (2×25 mL), then the combined organic extracts were washed with water (2×25 mL), brine (10 mL), dried on Na₂SO₄, filtered and evaporated to yield a pale yellow crude (980 mg) of which 817 mg was purified by chromatography on 100:0→20:1→10:1 Hx:EA giving **S1** as colourless oil (567 mg, 75%; R_f = 0.56 on 9:1 Hx:EA, Han). ¹H-NMR matched literature data (Bastos et al., 2005).

2-((*tert*-butyldimethylsilyl)oxy)-4-((3,4,5-trimethoxyphenyl)diazaryl)phenol (S2**)**

By Standard Procedure A, commercial 3,4,5-trimethoxyaniline (236 mg, 1.29 mmol) was reacted with **S1** (250 mg, 1.12 mmol) to yield a deep red crude oil. Chromatography on 5:1→1:1 Hx:EA returned **S2** as a yellow oil (102 mg, 0.244 mmol, 22%; R_f = 0.24 on 5:1 Hx:EA).

Alternatively, by Standard Procedure D, 3,4,5-trimethoxyaniline (237 mg, 1.29 mmol) was reacted with **S1** (300 mg, 1.34 mmol) to yield a black crude powder. Chromatography on 5:1→1:1 Hx:EA returned unreacted **S1** (226 mg, 1.01 mmol; R_f = 0.95 on 5:2 Hx:EA, Han), then **S2** as a yellow oil (76 mg, 0.182 mmol, 14% or 55% brsm; R_f = 0.63 on 5:2 Hx:EA), then a deep red powder suspected to be the bis(azo) product **S4** (10 mg, 0.016 mmol, 1.3%; R_f = 0.40 on 5:2 Hx:EA), and lastly **S3** as a deep orange solid (39 mg, 0.10 mmol, 8%; R_f = 0.15 on 5:2 Hx:EA).

S2: NMR of the product as isolated ex organic solvent revealed a roughly 55:44 proportion of [presumably E:Z] isomers when analysed in CDCl₃ without precautions to block ambient light. Their spectra could for some peaks be separated (denoted _E or _Z): ¹H-NMR (400 MHz): δ = 7.57-7.53 (m, 1H), 7.47-7.44 (m, 1H), 7.23 (s, 2Hz) & 7.21 (s, 2H_E), 7.07 (d, 8.5 Hz, 1H_E) & 6.97 (d, 8.5 Hz, 1Hz), 5.88 (s br, 1H_E) & 5.66 (s br, 1H_Z), 3.98 (s, 6H_E) & 3.97 (s, 6H_Z), 3.94 (s, 3H), 1.06 (s, 9H_E) & 1.05 (s, 9H_Z), 0.36 (s, 6H_E) & 0.34 (s, 6H_Z) ppm. ¹³C-NMR (100 MHz): δ = 153.5 (×2, E & Z), 150.3 &

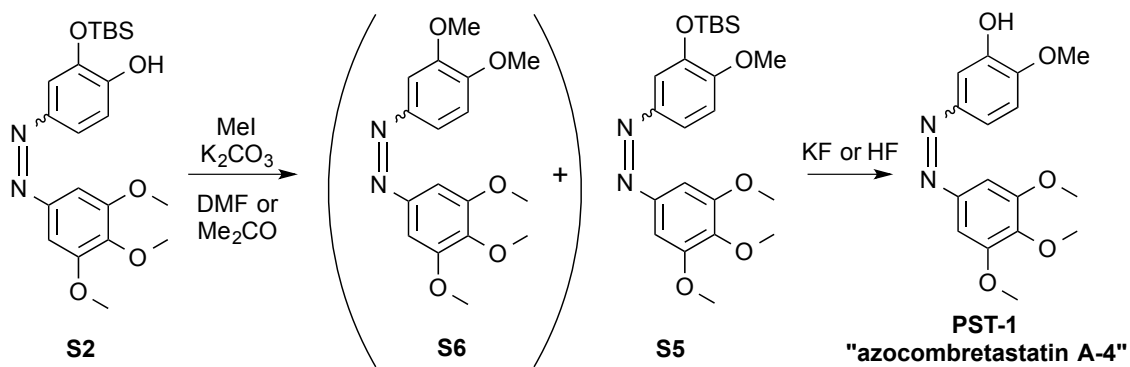
148.6 (E & Z), 148.5 & 142.9 (E & Z), 147.9 (E & Z), 146.5 & 145.4 (E & Z), 140.2 & 140.1 (E & Z), 119.6 & 118.1 (E & Z), 117.5 & 114.6 (Z & E), 110.7 & 106.9 (E & Z), 100.2 & 100.1 ($\times 2$, E & Z), 61.0 (E & Z), 56.2 & 56.2 ($\times 2$, E & Z), 25.8 & 25.7 ($\times 3$, E & Z), 18.3 & 18.2 (E & Z), -4.2 & -4.3 ($\times 3$, E & Z) ppm. LCMS(+): $t_{\text{ret}} = 5.60$ & 5.82 min, each 419 Th = [MH] $^+$: these peaks were assigned to the Z & E isomers respectively since the UV absorption profile of the first peak showed an absorption shoulder between 450-510 nm (Z), while the second peak was more intense especially between 320-380 nm (E) but without a shoulder. HRMS (ESI+) calcd for [C₂₁H₃₃N₂O₆Si] $^+ = [\text{M}\cdot\text{H}_3\text{O}^+]$: m/z 437.210, found 437.236.

3,4,5-trimethoxy-2-((3,4,5-trimethoxyphenyl)diazenyl)aniline (S3)

S3 was isolated as a deep orange solid (39 mg, 0.103 mmol, 8%; $R_f = 0.15$ on 5:2 Hx:EA) during Standard Procedure D for **S2**. Its formation might be due either to direct attack of the aniline on the diazonium with Nietzki rearrangement of the triazene product, or else to *ortho*-attack of the aniline on the diazonium. ¹H-NMR (400 MHz): $\delta = 7.14$ (s, 2H), 6.83 (s br, 2H), 5.96 (s, 1H), 4.08 (s, 3H), 3.96 (s, 6H), 3.92 (s, 3H), 3.89 (s, 3H), 3.88 (s, 3H) ppm. ¹³C-NMR (100 MHz): $\delta = 157.3$, 153.7, 153.6 ($\times 2$), 149.5, 139.0 ($\times 2$), 134.1, 124.9, 98.9 ($\times 2$), 93.7, 63.1, 61.6, 61.0, 56.1 ($\times 2$), 55.8 ppm. LCMS(+): $t_{\text{ret}} = 4.0$ min, 378 Th = [MH] $^+$. HRMS (ESI+) calcd for [C₁₈H₂₄N₃O₆] $^+ = [\text{MH}^+]$: m/z 378.1660, found 378.1657. **S3** crystallised from slow evaporation of a chloroform solution; single crystal X-ray diffraction confirmed the structural assignment (full data are available through the CCDC, with deposition #1028006).

2-((tert-butyldimethylsilyloxy)-4-((3,4,5-trimethoxyphenyl)diazenyl)-6-((3,4,5-trimethoxyphenyl)diazenyl)phenol (S4)

Trace **S4** was isolated as a deep red powder (10 mg, 0.016 mmol, 1.3%, $R_f = 0.40$ on 5:2 Hx:EA) during Standard Procedure D for **S2**, and assigned the given structure on the basis of its HRMS and ¹H-NMR. ¹H-NMR (400 MHz): $\delta = 7.42$ (s, 1H), 7.38 (s, 1H), 7.32 (s, 2H), 7.29 (s, 2H), 3.96 (s, 3H), 3.95 (s, 3H), 3.95 (s, 6H), 3.94 (s, 6H), 1.08 (s, 9H), 0.40 (s, 6H). HRMS (ESI+) calcd for [C₃₀H₄₁N₄O₈] $^+ = [\text{MH}^+]$: m/z 613.2688, found 613.2693.



2-methoxy-5-((3,4,5-trimethoxyphenyl)diazenyl)phenol ("azocombretastatin A-4", PST-1)

By Standard Procedure B, **S2** (100 mg, 0.23 mmol) was methylated in acetone (5 mL) using MeI (80 mg, 0.56 mmol) and K_2CO_3 (420 mg, 3 mmol). After evaporation of the volatiles, the residue was partitioned between $CHCl_3$ (10 mL) and aqueous phosphate buffer (pH=3), extracted with $CHCl_3$ (2×10 mL), and pad filtered on silica using 2.4:1 Hx:EA eluent, yielding 94 mg crude red oil. To this under nitrogen atmosphere were added MeCN (6 mL) and HF (70% in pyridine, 165 mg), and the reaction stirred for 15 minutes. $CaCO_3$ (1.0 g), $CaCl_2$ (0.5 g) and water (10 mL) were added to quench excess HF, the pH adjusted to 3 with KH_2PO_4 , then the mixture was extracted with $CHCl_3$ (3×10 mL). The combined organic layers were washed with brine (10 mL), dried on Na_2SO_4 , filtered and concentrated to a black crude powder (70 mg). Flash chromatography with 5:1 \rightarrow 2.4:1 Hx:EA in the dark (aluminium foil wrapped around the column) separated the three crude components cleanly without problems due to the different R_f values of their E and Z isomers, giving **S5** (6 mg, 0.014 mmol, 6%), then **S6** (5 mg, 0.015 mmol, 6%), then **PST-1** (14 mg, 0.044 mmol, 19 % over 2 steps).

Alternatively, to **S2** (73 mg, 0.175 mmol) were added K_2CO_3 (44 mg, 0.32 mmol), dry DMF (2 mL), and MeI (1.37 g of a 4.3 wt% solution in DMF, 0.43 mmol), and the mixture stirred at RT for 2 h until TLC (5:1 Hx:EA) showed complete conversion of the starting material to a faster-running product, presumably **S5**. The volatiles were evaporated at 60 °C and 5 mbar, then THF (8 mL) and an aqueous solution of KF (1 M, 5 mL) were added to the residue and the mixture stirred at RT for 3h 30 min. The bulk of the THF was removed on the rotavap, then water (15 mL), brine (2 mL), and KH_2PO_4/K_2HPO_4 buffer (2 M, pH=6.8, 4 mL) were added and the aqueous phase extracted with dichloromethane (3×15 mL). The combined organic layers were washed with water (15 mL) and brine (10 mL) and dried on Na_2SO_4 , filtered and concentrated to a crude oil. Flash chromatography with a very gentle gradient covering 5:1 \rightarrow 2.4:1 Hx:EA returned protected **S5** (12.0 mg, 0.028 mmol, 16%), then **S6** (8.0 mg, 0.024 mmol, 14%), then **PST-1** (19.7 mg, 0.062 mmol, 35% over 2 steps).

PST-1: R_f (E/Z)= 0.36 and 0.18 on 1.7:1 Hx:EA (Anis), orange solid. NMR of the product as isolated with blocking ambient light revealed a single geometric isomer. 1H -NMR (400 MHz): δ = 7.59-7.53 (m, 1H), 7.24 (s, 2H), 7.00 (d, 8.4 Hz, 1H), 5.84-5.66 (s br, 1H), 4.01 (s, 3H), 3.99 (s, 6H), 3.95 (s,

3H) ppm. ^{13}C -NMR (100 MHz): δ = 153.5 ($\times 2$), 149.2, 148.5, 147.3, 146.2, 140.2, 119.0, 110.1, 106.0, 100.2 ($\times 2$), 61.0, 56.2 ($\times 2$), 56.2 ppm. LCMS(+): t_{ret} = 3.12 & 3.89 min, each 319 Th = [MH] $^+$: these peaks were assigned to the *cis* & *trans* isomers respectively since the first peak had a secondary absorption band at 445 nm. HRMS (EI+) calcd for $[\text{C}_{16}\text{H}_{18}\text{N}_2\text{O}_5]^+ = [\text{M}^+]$: m/z 318.1288, found 318.1287. **PST-1** crystallised from slow evaporation of a chloroform/ethyl acetate solution; single crystal X-ray diffraction confirmed the structural assignment (full data are available through the CCDC, with deposition #1053581).

1-((*tert*-butyldimethylsilyl)oxy)-2-(3,4,5-trimethoxyphenyl)diazene (S5)

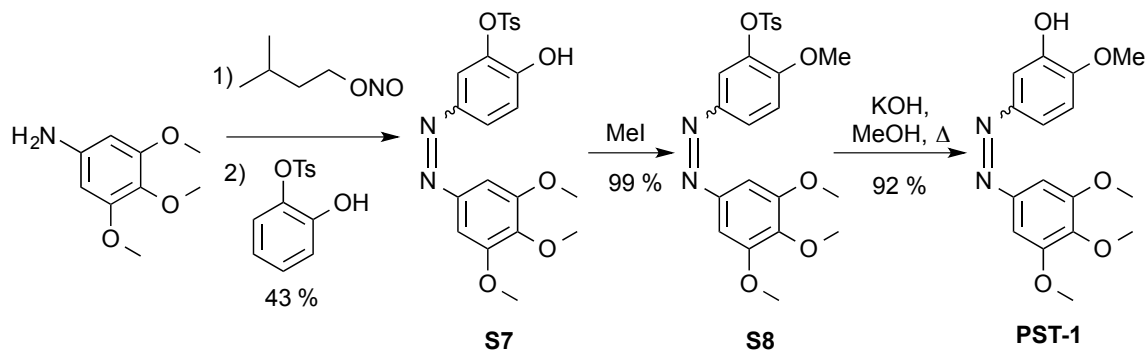
S5 was isolated as a yellow solid ($R_f(E/Z) = 0.65$ and 0.45 on 2.4:1 Hx:EA (Anis)) during the above procedures for **PST-1**. NMR of the product taken with precautions to block ambient light revealed a single geometric isomer. ^1H -NMR (400 MHz): δ = 7.61 (dd, 8.6 & 2.4 Hz, 1H), 7.48 (d, 2.4 Hz, 1H), 7.23 (s, 2H), 6.99 (d, 8.7 Hz, 1H), 3.99 (s, 6H), 3.95 (s, 3H), 3.92 (s, 3H), 1.05 (s, 9H), 0.23 (s, 6H) ppm. ^{13}C -NMR (100 MHz): δ = 154.1, 153.6 ($\times 2$), 148.6, 146.9, 145.7, 140.3, 119.7, 113.5, 111.3, 100.3 ($\times 2$), 61.2, 56.4 ($\times 2$), 55.7, 25.9 ($\times 3$), 18.7, -4.4, -4.5 ppm. LCMS(+): $t_{\text{ret}} = 5.40$ & 6.75 min, each 433.1 Th = [MH] $^+$: these peaks were assigned to the Z & E isomers respectively since the UV absorption profile from 350-390 nm of the first peak (Z) was far weaker than that of the second peak (E) although the integrals on the MSD were almost identical. HRMS (ESI+) calcd for $[\text{C}_{22}\text{H}_{33}\text{N}_2\text{O}_5\text{Si}]^+ = [\text{M}^+]$: m/z 433.21533, found 433.21532.

1-(3,4-dimethoxyphenyl)-2-(3,4,5-trimethoxyphenyl)diazene (S6)

S6 was isolated as a yellow solid ($R_f(E/Z) = 0.34$ and 0.14 on 2.4:1 Hx:EA; $R_f(E/Z) = 0.53$ and 0.28 on 1.7:1 Hx:EA (Anis)) during the above procedures for **PST-1**. NMR of the product taken with precautions to block ambient light revealed a single geometric isomer. ^1H -NMR (400 MHz): δ = 7.65 (dd, 8.5 & 2.2 Hz, 1H), 7.54 (d, 2.2 Hz, 1H), 7.26 (s, 2H), 7.03 (d, 8.5 Hz, 1H), 4.02 (s, 3H), 4.01 (s, 3H), 4.00 (s, 6H), 3.95 (s, 3H) ppm. ^{13}C -NMR (100 MHz, CD_3CN): δ = 154.3 ($\times 2$), 152.8, 150.4, 149.1, 147.1, 140.8, 120.9, 111.6, 102.4, 100.5, 60.6, 56.3 ($\times 2$), 56.2, 55.9 ppm. LCMS(+): $t_{\text{ret}} = 3.45$ & 4.35 min, each 333.1 Th = [MH] $^+$: these peaks were assigned to the Z & E isomers respectively since the first peak had a secondary absorption band at 440 nm. HRMS (ESI+) calcd for $[\text{C}_{17}\text{H}_{21}\text{N}_2\text{O}_5]^+ = [\text{M}^+]$: m/z 333.1445, found 333.1443.

PST-1: alternative route using tosyl protecting group

An alternative synthesis gave **PST-1** without byproduct **S6**.



2-hydroxy-5-((3,4,5-trimethoxyphenyl)diazenyl)phenyl 4-methylbenzenesulfonate (**S7**)

Commercial 3,4,5-trimethoxyaniline (1.045 g, 5.71 mmol) was reacted with known 2-hydroxyphenyl 4-para-toluenesulfonate (Bailey et al., 2004) (1.508 g, 5.71 mmol) by Standard Procedure A except that stirring of the mixture of phenolate and diazonium was continued for 5 h at 0 °C to for greater conversion. Following workup, the deep red crude oil was chromatographed on 5:1→1:1 Hx:EA returning **S7** as a yellow oil (1.130 g, 2.47 mmol, 43%; $R_f = 0.43$ on 1:1 Hx:EA). $^1\text{H-NMR}$ (400 MHz): $\delta = 7.76$ (d, 8.4 Hz, 2H), 7.72 (dd, 8.7 & 2.3 Hz, 1H), 7.51 (d, 2.3 Hz, 1H), 7.29 (dd, 8.5 & 0.8 Hz, 2H), 7.11 (s, 2H), 7.04 (d, 8.7 Hz, 1H), 3.89 (s, 6H), 3.86 (s, 3H), 2.39 (s, 3H) ppm. $^{13}\text{C-NMR}$ (100 MHz): $\delta = 153.5$ ($\times 2$), 150.7, 148.1, 146.4, 146.4, 140.7, 137.3, 131.2, 130.1 ($\times 2$), 128.7 ($\times 2$), 124.0, 118.1, 117.4, 100.4 ($\times 2$), 61.1, 56.2 ($\times 2$), 21.8 ppm. LCMS(+): $t_{\text{ret}} = 4.60$ min, 459 Th = [MH] $^+$. HRMS (ESI+) calcd for $[\text{C}_{22}\text{H}_{23}\text{N}_2\text{O}_7\text{S}]^+ = [\text{MH}^+]$: m/z 459.12205, found 459.12168.

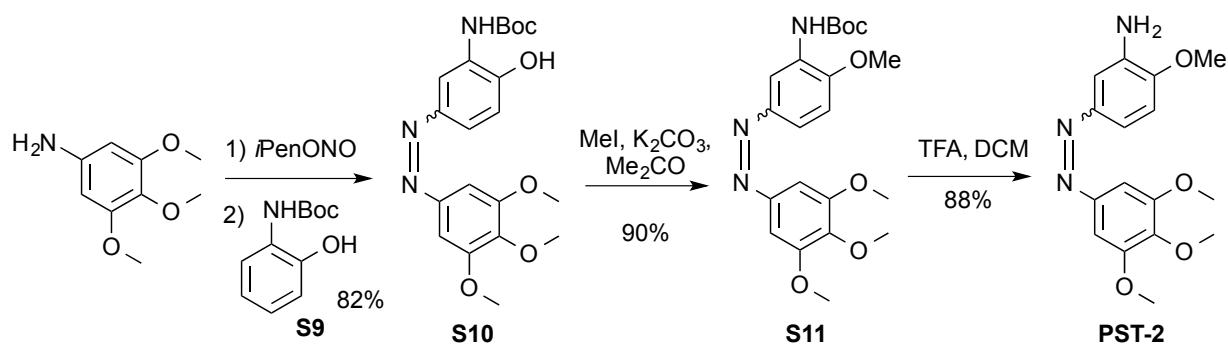
2-methoxy-5-((3,4,5-trimethoxyphenyl)diazenyl)phenyl 4-methylbenzenesulfonate (**S8**)

By Standard Procedure B, **S7** (700 mg, 1.53 mmol) was methylated overnight. Chromatography of the red crude solid on 5:1→1:1 Hx:EA returned **S8** (712 mg, 1.51 mmol, 99%; $R_f = 0.62$ and 0.46 on 1:1 Hx:EA, FeCl_3 ; E and Z isomers) as a red oil. $^1\text{H-NMR}$ (400 MHz, DMSO-d_6): $\delta = 7.93$ (dd, 8.8 & 2.4 Hz, 1H), 7.75 (d, 8.4 Hz, 2H), 7.63 (d, 2.4 Hz, 1H), 7.49 (d, 8.5 Hz, 2H), 7.28 (d, 8.9 Hz, 1H), 7.23 (s, 2H), 3.91 (s, 6H), 3.77 (s, 3H), 3.61 (s, 3H), 2.44 (s, 3H) ppm. $^{13}\text{C-NMR}$ (100 MHz, DMSO-d_6): $\delta = 154.2$, 153.8 ($\times 2$), 148.0, 146.3, 145.6, 140.7, 138.5, 132.3, 130.4 ($\times 2$), 128.8 ($\times 2$), 126.2, 115.6, 113.9, 100.7 ($\times 2$), 60.7, 56.6, 56.5 ($\times 2$), 21.6 ppm. LCMS(+): $t_{\text{ret}} = 4.48$ & 5.17 min, 473 Th = [MH] $^+$: these peaks were assigned to the *cis* & *trans* isomers respectively since the UV absorption profile of the first peak (*cis*) featured a shoulder centred around 450 nm. HRMS (ESI+) calcd for $[\text{C}_{23}\text{H}_{25}\text{N}_2\text{O}_7\text{S}]^+ = [\text{MH}^+]$: m/z 473.13770, found 473.13730.

2-methoxy-5-((3,4,5-trimethoxyphenyl)diazenyl)phenol, “azocombretastatin A-4” (PST-1)

To **S8** (525 mg, 1.10 mmol) were added KOH (1.25 g) and MeOH (25 mL) and the solution heated to 80 °C for 1 hour. After evaporation of the volatiles, the residue was partitioned between EtOAc (20 mL) and aqueous KH₂PO₄ solution (10%, 30 mL), then the aqueous layer was extracted with EtOAc (2×10 mL). The combined organic layers were washed with water (20 mL), brine (10 mL), dried on Na₂SO₄, filtered and concentrated. The crude oil was chromatographed on 5:1→1:1 Hx:EA, giving **PST-1** (320 mg, 1.01 mmol, 92%) as an orange solid, identical by NMR and LCMS to that synthesised previously from **S2**.

PST-2: meta-amino analogue (azoombrabulin’s active core)



tert-butyl (2-hydroxyphenyl)carbamate (S9)

2-aminophenol (3.93 g, 36 mmol) was stirred with *tert*-butoxycarbonyl dicarbonate (8.32 g, 38 mmol) in dry pyridine (30 mL) with triethylamine (4 mL) warming from 0 °C to 25 °C over 12 h. The volatiles were evaporated and the residue partitioned between diethyl ether and phosphate buffer (pH=10); the ether layer was washed with phosphate buffer then brine, dried on Na₂SO₄, filtered and evaporated to yield 8.1 g of dark crude product which could be purified by column chromatography (20:1→5:1 Hex:EA), or by fractional crystallisations from acetone-hexane followed by hot hexane trituration, to give known compound **S9**. NMR spectra matched literature data (Shindo et al., 2003): ¹H-NMR (400 MHz): δ = 8.15 (s br, 1H), 7.08-7.00 (m, 2H), 6.99 (d, 7.9 Hz, 1H), 6.88 (~t, 7.5 Hz, 1H), 6.69 (s, 1H), 1.56 (s, 9H) ppm. ¹³C-NMR (100 MHz): δ = 155.1, 147.6, 125.7, 125.5, 121.5, 120.7, 119.1, 82.2, 28.3 (×3) ppm. DIMS(ESI+): 210 Th = [MH]⁺.

tert-butyl (2-hydroxy-5-((3,4,5-trimethoxyphenyl)diazenyl)phenyl)carbamate (S10)

By Standard Procedure A, 3,4,5-trimethoxyaniline (368 mg, 2.01 mmol) was reacted with **S9** (406 mg, 1.94 mmol). Chromatography on 5:1→2.4:1 Hx:EA returned **S10** (642 mg, 1.59 mmol, 82%; R_f = 0.22 on 2.4:1 Hx:EA, FeCl₃) as a brown viscous oil. ¹H-NMR (400 MHz, CD₃CN): δ = 8.36 (s, 1H), 8.32 (d, 2.3 Hz, 1H), 7.54 (dd, 8.5 & 2.4 Hz, 1H), 7.35 (s, 1H), 7.19 (s, 2H), 7.02 (d, 8.5 Hz, 1H), 3.89 (s, 6H), 3.80 (s, 3H) ppm. ¹³C-NMR (100 MHz, CD₃CN): δ = 153.7 (×2), 153.5, 149.0, 148.5, 146.1, 140.1, 127.5, 120.6, 115.4, 112.3, 100.0 (×2), 80.6, 60.0, 55.8 (×2), 27.52 (×3)

ppm. LCMS(+): $t_{\text{ret}} = 4.65$ min, 404 Th = [MH]⁺. HRMS (ESI+) calcd for [C₂₀H₂₆N₃O₆]⁺ = [MH⁺]: m/z 404.1816, found 404.1817.

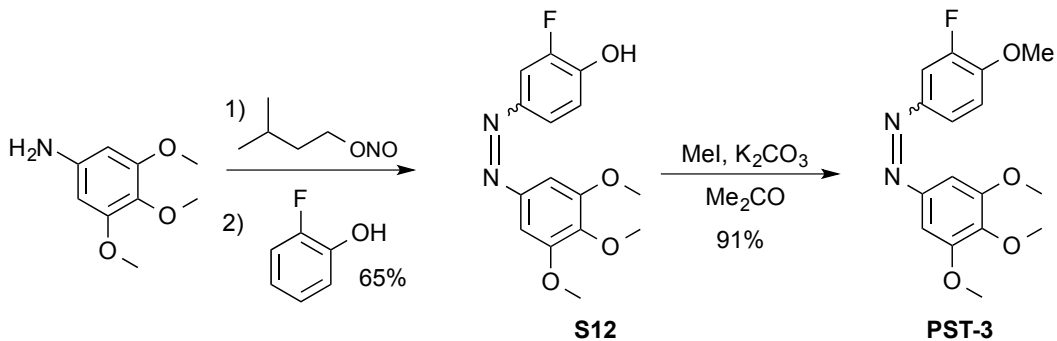
tert-butyl (2-methoxy-5-((3,4,5-trimethoxyphenyl)diazenyl)phenyl)carbamate (S11)

By Standard Procedure B, **S10** (637 mg, 1.58 mmol) was methylated overnight with MeI (448 mg, 3.13 mmol) and K₂CO₃ (873 mg, 6.32 mmol). Chromatography of the black crude solid on 5:1→2.4:1 Hx:EA returned **S11** (593 mg, 1.42 mmol, 90%; R_f = 0.41 on 2.4:1 Hx:EA, FeCl₃) as a red oil. ¹H-NMR (400 MHz): δ = 8.64 (s br, 1H), 7.58 (dd, 8.7 & 2.4 Hz, 1H), 7.20 (s, 2H), 7.09 (s, 1H), 6.90 (d, 8.7 Hz, 1H), 3.90 (s, 9H), 3.86 (s, 3H), 1.49 (s, 9H) ppm. ¹³C-NMR (100 MHz): δ = 153.4 (×2), 152.6, 149.8, 148.4, 146.7, 140.2, 128.8, 119.1, 111.2, 109.6, 100.4 (×2), 80.7, 61.0, 56.2 (×2), 56.0, 28.4 (×3) ppm. LCMS(+): $t_{\text{ret}} = 4.57$ & 5.42 min, 418 Th = [MH]⁺: these peaks were assigned to the Z & E isomers respectively since the UV absorption profile of the first peak (Z) featured a shoulder centred around 440 nm. HRMS (ESI+) calcd for [C₂₁H₂₈N₃O₆]⁺ = [MH⁺]: m/z 418.19726, found 418.19718.

2-methoxy-5-((3,4,5-trimethoxyphenyl)diazenyl)aniline (PST-2)

To **S11** (590 mg, 1.41 mmol) were added CH₂Cl₂ (6 mL) and CF₃COOH (5 mL) and the purple solution stirred overnight at room temperature. The volatiles were removed under high vacuum, the residual TFA neutralised with addition of CHCl₃ (10 mL) and K₂CO₃ (618 mg) and the residue chromatographed on 1:1:0→1:1:1 Hx:EA:MeOH, giving **PST-2** as a green-black powder (394 mg, 1.24 mmol, 88 %; R_f = 0.56 on 1:1 Hx:EA (Van)). NMR when analysed in CDCl₃ without precautions to block ambient light showed two isomers in approximately 2:1 ratio [presumably *trans* and *cis* forms, attributed by HSQC, denoted _E and _Z]. ¹H-NMR (400 MHz): δ = 8.84 (s br, ‘1H’, NH₂), 7.72 (dd, 8.5 & 1.9 Hz, 1H_E), 7.58 (d, 2.2 Hz, 1H_Z), 7.56 (d, 1.9 Hz, 1H_E), 7.53 (dd, 8.6 & 2.4 Hz, 1H_Z), 7.26 (d, 8.5 Hz, 1H_E), 7.19 (s, 2H_E), 7.16 (s, 2H_Z), 6.90 (d, 8.6 Hz, 1H_Z), 3.92-3.84 (m, 12H_E & 12H_Z) ppm. ¹³C-NMR (100 MHz): δ = 153.6 & 153.5 (×2, E&Z), 151.6 & 149.4 (×1, E&Z), 148.5 & 148.1 (×1, E&Z), 146.8 & 145.7 (×1, E&Z), 140.8 & 140.2 (×1, E&Z), 130.0 (×1, E&Z), 121.7 & 120.7 (×1, E&Z), 110.4 & 110.3 (×1, E&Z), 110.1 & 101.3 (×1, E&Z), 100.5 & 100.2 (×2, E&Z), 61.1 & 61.0 (×1, E&Z), 56.2 & 56.2 (×2, E&Z), 56.1 (×1, E&Z) ppm. LCMS(+): $t_{\text{ret}} = 3.04$ & 3.94 min, each 318 Th = [MH]⁺: these peaks were assigned to the *cis* & *trans* isomers respectively as the first peak featured an absorption shoulder at 450 nm which was absent in the second peak (*trans*). HRMS (ESI+) calcd for [C₁₆H₂₀N₃O₄]⁺ = [MH⁺]: m/z 318.1448, found 318.1449.

PST-3: meta-fluoro analogue



2-fluoro-4-((3,4,5-trimethoxyphenyl)diazenyl)phenol (S12)

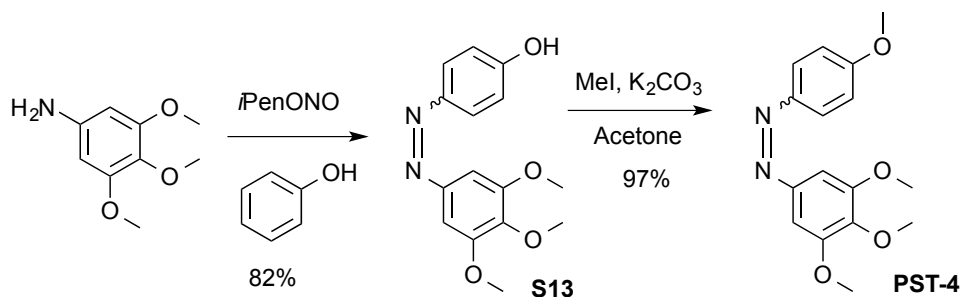
By Standard Procedure A, 3,4,5-trimethoxyaniline (183 mg, 1.00 mmol) was reacted with 2-fluorophenol (116 mg, 1.04 mmol). Chromatography on 5:1→2.5:1 Hx:EA returned **S12** (198 mg, 0.65 mmol, 65%; R_f = 0.25 on 2.4:1 Hx:EA, KMnO₄) as a yellow oil. ¹H-NMR (400 MHz, DMSO-d₆): δ = 10.77 (s, 1H), 7.68 (~t, 8.9 Hz, 1H), 7.18 (s, 2H), 6.80 (dd, 12.7 & 2.5 Hz, 1H), 6.74 (dd, 8.9 & 2.5 Hz, 1H), 3.88 (s, 6H), 3.76 (s, 3H) ppm. ¹³C-NMR (100 MHz, DMSO-d₆) showed the expected C-F couplings: δ = 162.8 (d, 12.1 Hz), 161.2 (d, 255.7 Hz), 153.8 (×2), 148.6, 140.3, 133.4 (d, 6.9 Hz), 119.0 (d, 2.0 Hz), 112.9 (d, 2.4 Hz), 103.8 (d, 21.8 Hz), 100.4 (×2), 60.7, 56.4 (×2) ppm. HRMS (ESI-) calcd for [C₁₅H₁₄N₂O₄F]⁺ = [M-H]⁻: m/z 305.09431, found 305.09433.

1-(3-fluoro-4-methoxyphenyl)-2-(3,4,5-trimethoxyphenyl)diazene (PST-3)

By Standard Procedure B, **S17** (190 mg, 0.62 mmol) was methylated overnight. Chromatography on 10:1→4:1 Hx:EA cleanly returned **S20** (173 mg, 0.54 mmol, 91%; R_f = 0.42 and 0.25 on 2.4:1 Hx:EA, FeCl₃ : E and Z isomers) as fine orange crystals. ¹H-NMR (400 MHz, DMSO-d₆): δ = 7.75 (~t, 9.0 Hz, 1H), 7.22 (s, 2H), 7.12 (dd, 13.0 & 2.6 Hz, 1H), 6.92 (ddd, 9.2 & 2.7 & 0.9 Hz, 1H), 3.89 (s, 6H), 3.89 (s, 3H), 3.77 (s, 3H) ppm. ¹³C-NMR (100 MHz, DMSO-d₆) showed the expected C-F couplings: δ = 163.8 (d, 11.2 Hz), 161.1 (d, 255.9 Hz), 153.8 (×2), 148.5, 140.6, 134.3 (d, 7.2 Hz), 118.8 (d, 2.1 Hz), 112.0 (d, 2.6 Hz), 102.7 (d, 23.4 Hz), 100.6 (×2), 60.7, 56.7, 56.4 (×2) ppm. ¹⁹F-NMR (282 MHz, DMSO-d₆): δ = -121.31 (ddd, 13.2 & 8.8 & 1.1 Hz) ppm. LCMS(+): t_{ret} = 3.96 & 4.82 min, each 321 Th = [MH]⁺: these peaks were assigned to the Z & E isomers respectively since the UV absorption profile of the first peak (Z) featured a shoulder centred at 445 nm which was absent in the first peak. HRMS (EI+) calcd for [C₁₆H₁₇N₂O₄F]⁺ = [M]⁺: m/z 320.1172, found 320.1167.

PST-4: meta-hydro analogue

PST-4 was actually reported in 1949 (Friedman et al., 1949). However, this was 15 years before the identification of tubulin, the compound was never photoswitched, and no subsequent research has returned to it until now.



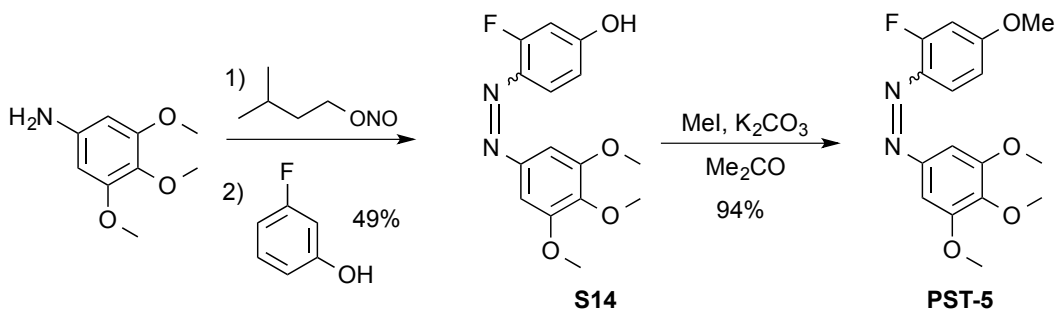
4-((3,4,5-trimethoxyphenyl)diazenyl)phenol (**S13**) (Friedman et al., 1949)

By Standard Procedure A, 3,4,5-trimethoxyaniline (174 mg, 0.95 mmol) was reacted with phenol (102 mg, 1.08 mmol). Chromatography of the red crude oil on 5:1→2.4:1 Hx:EA returned **S13** (227 mg, 0.78 mmol, 82%; $R_f = 0.64$ on 1:1 Hx:EA, FeCl_3) as a red oil. $^1\text{H-NMR}$ (400 MHz): $\delta = 7.81$ (d, 8.8 Hz, 2H), 7.19 (s, 2H), 6.89 (d, 8.9 Hz, 2H), 3.89 (s, 6H), 3.86 (s, 3H) ppm. $^{13}\text{C-NMR}$ (100 MHz): $\delta = 159.1, 153.5 (\times 2), 148.2, 146.6, 140.2, 125.1 (\times 2), 116.0 (\times 2), 100.1 (\times 2), 61.1, 56.2 (\times 2)$ ppm. HRMS (ESI+) calcd for $[\text{C}_{15}\text{H}_{17}\text{N}_2\text{O}_4]^+ = [\text{MH}]^+$: m/z 289.11828, found 289.11813.

1-(4-methoxyphenyl)-2-(3,4,5-trimethoxyphenyl)diazene (**PST-4**) (Friedman et al., 1949)

By Standard Procedure B, **S13** (226 mg, 0.77 mmol) was methylated overnight. Chromatography on 5:1→3:1 Hx:EA returned **PST-4** (231 mg, 0.76 mmol, 97%; $R_f = 0.76$ and 0.60 on 1:1 Hx:EA, E and Z isomers, FeCl_3) as a red oil. $^1\text{H-NMR}$ (400 MHz): $\delta = 7.85 (\sim \text{d}, 8.9 \text{ Hz}, 2\text{H}), 7.16 (\text{s}, 2\text{H}), 6.95 (\text{d}, 9.0 \text{ Hz}, 2\text{H}), 3.90 (\text{s}, 6\text{H}), 3.86 (\text{s}, 3\text{H}), 3.83 (\text{s}, 3\text{H})$ ppm. $^{13}\text{C-NMR}$ (100 MHz): $\delta = 162.0, 153.5 (\times 2), 148.5, 146.7, 140.2, 124.7 (\times 2), 114.3 (\times 2), 100.1 (\times 2), 61.1, 56.2 (\times 2), 55.6$ ppm. LCMS(+): $t_{\text{ret}} = 3.80 \& 4.78 \text{ min}$, each $303 \text{ Th} = [\text{MH}]^+$: these peaks were assigned to the Z & E isomers respectively since the UV absorption profile of the first peak (Z) featured a shoulder centred around 440 nm which was absent in the first peak. HRMS (ESI+) calcd for $[\text{C}_{16}\text{H}_{19}\text{N}_2\text{O}_4]^+ = [\text{MH}]^+$: m/z 303.13393, found 303.13371.

PST-5: meta-hydro, ortho-fluoro analogue



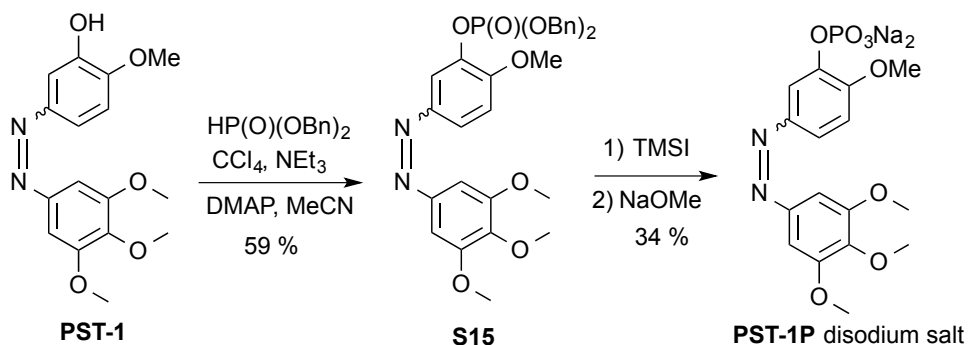
3-fluoro-4-((3,4,5-trimethoxyphenyl)diazenyl)phenol (S14)

By Standard Procedure A, 3,4,5-trimethoxyaniline (196 mg, 1.07 mmol) was reacted with 3-fluorophenol (120 mg, 1.07 mmol), and the product was extracted with ethyl acetate. Chromatography on 5:1→2.5:1 Hx:EA returned **S16** (161 mg, 0.53 mmol, 49%; R_f = 0.20 on 2.4:1 Hx:EA, KMnO₄) as a yellow oil only sparingly soluble in CH₂Cl₂ or CHCl₃. ¹H-NMR (400 MHz): δ = 7.68 – 7.60 (m, 2H), 7.14 (s, 2H), 7.07 (~t, 8.8 Hz, 1H), 5.47 (d br, 4.2 Hz, 1H), 3.89 (s, 6H), 3.86 (s, 3H) ppm. ¹³C-NMR (100 MHz) showed the expected C-F couplings: δ = 153.5 (×2), 151.3 (d, 240.1 Hz), 148.2, 146.7 (d, 5.2 Hz), 146.1 (d, 15.3 Hz), 140.5, 122.6 (d, 2.9 Hz), 117.0 (d, 2.2 Hz), 107.8 (d, 19.3 Hz), 100.3 (×2), 61.1, 56.2 (×2) ppm. HRMS (ESI-) calcd for [C₁₅H₁₄N₂O₄F]⁺ = [M-H]⁺: m/z 305.09431, found 305.09427.

1-(2-fluoro-4-methoxyphenyl)-2-(3,4,5-trimethoxyphenyl)diazene (PST-5)

By Standard Procedure B, **S14** (159 mg, 0.52 mmol) was methylated overnight in a mixture of acetone (15 mL), EA (0.6 mL), CHCl₃ (0.7 mL) and DMSO (0.7 mL). Chromatography on 10:1→4:1 Hx:EA cleanly returned **S19** (158 mg, 0.49 mmol, 94%; R_f = 0.44 and 0.20 on 2.4:1 Hx:EA, FeCl₃ : E and Z isomers) as a red oil. ¹H-NMR (400 MHz, DMSO-d₆): δ = 7.83 (ddd, 8.7 & 2.4 & 1.2 Hz, 1H), 7.69 (dd, 12.4 & 2.3 Hz, 1H), 7.39 (~t, 8.9 Hz, 1H), 7.24 (s, 2H), 3.96 (s, 3H), 3.89 (s, 6H), 3.77 (s, 3H) ppm. ¹³C-NMR (100 MHz, DMSO-d₆) showed the expected C-F couplings: δ = 153.85 (×2), 152.3 (d, 247.1 Hz), 150.3 (d, 11.1 Hz), 148.0, 146.0 (d, 5.1 Hz), 140.6, 123.3 (d, 2.9 Hz), 114.1 (d, 2.2 Hz), 107.4 (d, 19.1 Hz), 100.6 (×2), 60.7, 56.8, 56.5 (×2) ppm. ¹⁹F-NMR (282 MHz, DMSO-d₆): δ = -133.45 (ddd, 12.2 & 10.2 & 1.3 Hz) ppm. LCMS(+): t_{ret} = 3.86 & 4.80 min, each 321 Th = [MH]⁺; these peaks were assigned to the Z & E isomers respectively since the UV absorption profile of the first peak (Z) featured a shoulder centred at 440 nm which was absent in the first peak. HRMS (EI+) calcd for [C₁₆H₁₇N₂O₄F]⁺ = [M]⁺: m/z 320.1172, found 320.1170.

PST-1P: “azo-CA4P”, a water-soluble phosphate prodrug of PST-1



PST-1P was desired for the reasons outlined in Appendix 4. **PST-1P** and its precursor **S15** were synthesised similarly to a described procedure by Pettit (Pettit and Rhodes, 2009) developed to efficiently transform the analogous stilbene **CA4** into **CA4P**.

dibenzyl (2-methoxy-5-((3,4,5-trimethoxyphenyl)diazenyl)phenyl) phosphate (S15)

Similarly to the described procedure (Pettit and Rhodes, 2009), **PST-1** (100 mg, 0.31 mmol) was dissolved in dry acetonitrile (4 mL) under nitrogen, then the solution cooled to -30 °C. CCl₄ (242 mg, 1.57 mmol) was added, then NEt₃ which had been stood on KOH (71 mg), and 4-(N,N-dimethylamino)pyridine (DMAP; 5 mg). Dibenzyl phosphite (122 mg, 0.46 mmol) was then added dropwise. The reaction was stirred for 3 h at -30 °C, then as LCMS showed incomplete conversion of the starting material, additional dibenzyl phosphite (180 mg, 0.68 mmol) and CCl₄ (300 mg, 1.94 mmol) were added. The mixture was stirred warming to room temperature overnight. Aqueous KH₂PO₄ solution (10%, 10 mL) was added and the aqueous phase extracted with EtOAc (4×10 mL). The combined organic layers were washed with water (10 mL), brine (10 mL), dried on Na₂SO₄, filtered and concentrated. The crude oil thus obtained was chromatographed on 5:1→1:1 Hx:EA, giving **S15** (105 mg, 0.18 mmol, 59%; R_f = 0.38 and 0.22 on 1:1 Hx:EA (*trans* and *cis* isomers), Han) as a yellow oil. ¹H-NMR (400 MHz): δ = 7.82 (dd, 2.3 & 1.5 Hz, 1H), 7.73 (ddd, 8.7 & 2.4 & 1.0 Hz, 1H), 7.33 – 7.21 (m, 10H), 7.14 (s, 2H), 6.96 (dd, 8.8 & 1.0 Hz, 1H), 5.14 (d, 7.9 Hz, 4H), 3.90 (s, 6H), 3.87 (s, 3H), 3.80 (s, 3H) ppm. ¹³C-NMR (100 MHz) apparently resolved some C–P couplings: δ = 153.5 (×2), 153.0 (d, 5.1 Hz), 148.3, 146.3 (d, 1.8 Hz), 140.4, 140.1 (d, 7.2 Hz), 135.6 (d, 7.5 Hz, ×2), 128.6 (×4), 128.5 (×2), 127.9 (×4), 123.2 (d, 1.4 Hz), 114.2 (d, 3.1 Hz), 112.0, 100.3 (×2), 70.0 (d, 5.9 Hz, ×2), 61.1, 56.2 (×2), 56.2 ppm. HRMS (ESI+) calcd for [C₃₀H₃₂N₂O₈P]⁺ = [MH]⁺: m/z 579.18908, found 579.18938. LCMS(+): t_{ret} = 4.69 & 5.27 min, 579 Th = [MH]⁺; the first peak was assigned as the *cis* isomer due to its absorbance shoulder centred at 450 nm.

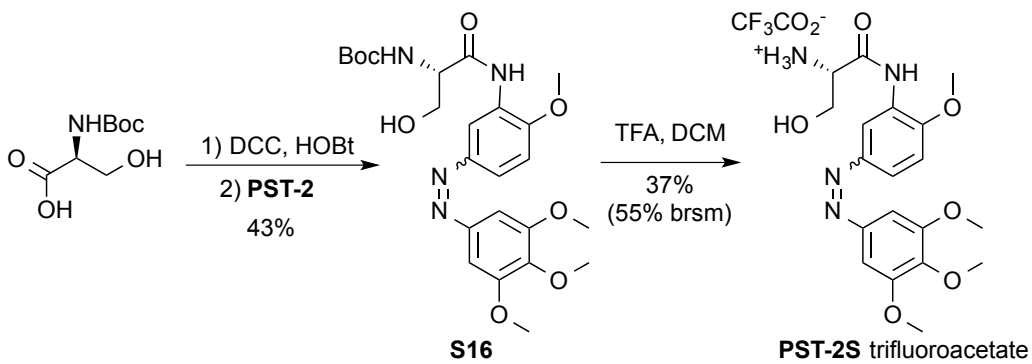
2-methoxy-5-((3,4,5-trimethoxyphenyl)diazenyl)phenyl phosphate (PST-1P), disodium salt

Similarly to a described, analogous procedure (Pettit and Rhodes, 2009), to **S15** (100 mg, 0.165 mmol) were added under nitrogen, NaI (49 mg, 0.33 mmol), dry acetonitrile (2.5 mL), and

TMSCl (37 mg, 0.34 mmol). The mixture was stirred for 4 h at room temperature. Water (1.5 mL) and aqueous Na₂S₂O₃ solution (10%, 0.05 mL) were added and the aqueous phase extracted with EtOAc (3×10 mL). The combined organic layers were dried on Na₂SO₄, filtered and concentrated to a red crude oil. To the crude oil were added under nitrogen, dry MeOH (3 mL) and NaOMe (18.5 mg) and the reaction was stirred overnight. The volatiles were evaporated, and the yellow oily residue (principally containing **PST-1P** disodium salt together with its monobenzyl ester, which was identified by LCMS as the peak with $t_{\text{ret}} = 3.08 \text{ min}$, 489 Th) was repeatedly triturated with cyclohexane (3×3 mL), 1:3 cyclohexane:ethyl acetate (5×2 mL), ethyl acetate (2×2 mL), and lastly acetone (2×2 mL), leaving **PST-1P** disodium salt as a yellow-brown powder (25 mg, 0.056 mmol, 34%) which was fully soluble in PBS to at least 25 mM. ¹H-NMR (400 MHz, D₂O): $\delta = 7.63$ (s, 1H), 7.39 (d, 8.7 Hz, 1H), 6.98 (d, 9.3 Hz, 1H), 6.97 (s, 2H), 3.80 (s, 3H), 3.77 (s, 6H), 3.70 (s, 3H) ppm. ¹³C-NMR (100 MHz, D₂O) apparently resolved some C–P couplings: $\delta = 153.3$ (~d, 5.5 Hz), 152.7 (×2), 148.2, 145.5, 142.5 (~d, 6.5 Hz), 138.8, 121.5, 112.2, 112.1, 100.0 (×2), 60.9, 55.9 (×2), 55.8 (~d, 4.5 Hz) ppm. HRMS (ESI-) calcd for [C₁₆H₁₈N₂O₈P]⁻ = [M-H]⁻: m/z 397.08008, found 397.08029. LCMS(+): $t_{\text{ret}} = 2.04$ & 2.44 min, 399 Th = [MH]⁺; the first peak was assigned as the *cis* isomer due to its absorbance shoulder centred at 450 nm.

The susceptibility of the phosphate ester to spontaneous hydrolysis was summarily evaluated by HPLC as follows: a solution of **PST-1P** at 10 μM in PBS + 1% MeCN was prepared and left to stand for 3 weeks at room temperature in a closed vial protected from light, then analysed by HPLC. The ratio of **PST-1** : **PST-1P** was estimated as 1:7 by integrating the UV-Vis trace at 210 nm for the respective peaks; it was therefore concluded that the halflife for spontaneous degradation in physiologically relevant media under ambient conditions was on the order of 100 days or more.

PST-2S: “azoombrabulin” – a water-soluble serine prodrug of PST-2



PST-2S was desired for the reasons outlined in Appendix 4.

(2-methoxy-5-((3,4,5-trimethoxyphenyl)diazenyl)phenyl)-1-(N'-tert-butoxycarbonyl)L-serinamide (S16)

To commercial *N'*-*tert*-butoxycarbonyl-L-serine (65 mg, 0.32 mmol) in an icebath were added DCM (15 mL), HOEt (50 mg, 0.37 mmol) and DCC (68 mg, 0.33 mmol), and the mixture stirred for 5 min. **PST-2** (100 mg, 0.31 mmol) was added, and stirring continued overnight while warming slowly to room temperature. The organic phase was washed with saturated aqueous sodium carbonate solution (20 mL), pH=10 phosphate buffer (20 mL), and brine (20 mL), then dried on Na₂SO₄, filtered, concentrated and chromatographed on 5:1→1:5 Hx:EA, returning **S16** (70 mg, 0.14 mmol, 43%; R_f = 0.24 & 0.12 on 1:1 Hx:EA, *trans* & *cis* isomers, FeCl₃) as a brown solid. ¹H-NMR (400 MHz): δ = 8.87 (d, 2.4 Hz, 1H), 7.65 (dd, 8.6 & 2.4 Hz, 1H), 7.18 (s, 2H), 6.94 (d, 8.8 Hz, 1H), 5.61 (s br, 1H), 4.38-4.12 (m, 3H), 3.90 (s, 3H), 3.89 (s, 6H), 3.86 (s, 3H), 1.44 (s, 9H) ppm. ¹³C-NMR (100 MHz): δ = 169.7, 157.4, 153.5 (\times 2), 150.5, 148.5, 146.7, 140.2, 127.7, 121.2, 112.9, 109.9, 100.2 (\times 2), 80.8, 62.7, 61.0, 56.2 (\times 2), 56.1, 50.1, 28.3 (\times 3) ppm. HRMS (ESI+) calcd for [C₂₄H₃₃N₄O₈]⁺ = [MH]⁺: m/z 505.22929, found 505.22945. LCMS(+): t_{ret} = 3.52 & 4.22 min, each 505 Th = [MH]⁺, *cis* and *trans* isomers respectively.

(2-methoxy-5-((3,4,5-trimethoxyphenyl)diazenyl)phenyl)-1-L-serinamide (PST-2S), 2,2,2-trifluoroacetate salt

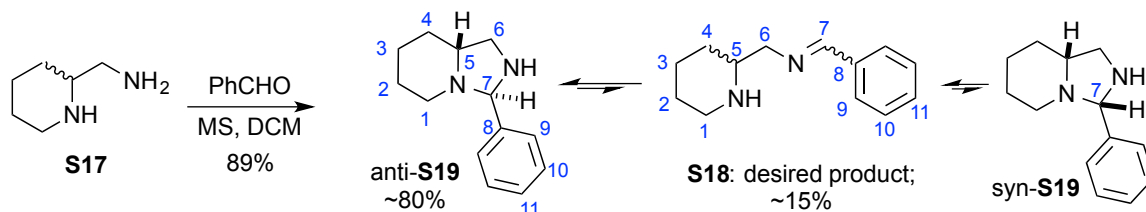
To **S16** (55 mg, 0.11 mmol) were added DCM (1 mL) and TFA (1 mL) and the purple solution stirred at room temperature for 1 h. The volatiles were removed at 1 mbar until a brown crude oil was obtained. Chromatography on 1:1:0→1:1:0.3 Hx:EA:MeOH returned unreacted **S16** (18 mg, 0.036 mmol) then **PST-2S** as the 2,2,2-trifluoroacetate salt (21 mg, 0.041 mmol, 37% or 55%brsm; R_f = 0.35 on 1:1:0.3 Hx:EA:MeOH, FeCl₃) as a brown viscous oil. ¹H-NMR (400 MHz, DMSO-d₆): δ = 8.63 (d, 2.5 Hz, 1H), 8.38 (s br, 3H), 7.80 (dd, 8.7 & 2.5 Hz, 1H), 7.32 (d, 8.9 Hz, 1H), 7.23 (s, 2H), 5.70 (s br, 1H), 4.70 (dd, 9.1 & 4.2 Hz, 1H), 4.54 (t, 8.9 Hz, 1H), 4.34 (dd, 8.8 & 4.1 Hz, 1H), 3.99 (s, 3H), 3.91 (s, 6H), 3.77 (s, 3H) ppm. ¹³C-NMR (100 MHz, DMSO-d₆): δ = 172.0, 158.0 (q, 31.6 Hz),

153.4 ($\times 2$), 152.1, 147.8, 145.4, 139.9, 127.2, 122.5, 117.1 (q, 294 Hz), 113.7, 111.4, 99.9 ($\times 2$), 60.5, 60.2, 56.4, 56.0 ($\times 2$), 54.5 ppm. HRMS (ESI $^+$) calcd for $[C_{19}H_{25}N_4O_6]^+ = [MH]^+$: m/z 405.17686, found 405.17695. LCMS(+): $t_{ret} = 2.30 - 2.65$ min (broad), 405 Th = $[MH]^+$.

PST-1CL and CA4CL: peptide prodrugs of PST-1 and CA4

PST-1CL was desired for dual optical-and-biochemical targeting; see Appendix 4.

Cyclisation spacer substrate S20, initial route:



S18 was desired as the first step of a potentially higher yielding synthesis of peptide-cyclisation spacer constructs such as **S20** than is currently reported (Thorn-Seshold et al., 2012). This was planned by initially differentiating the amine sites in cyclisation spacer **S17** through protecting groups, then regioselectively deprotecting the primary amine followed by peptide coupling. However, in the initial step, a majority of isomeric aminal forms **S19** was observed, so a regio-differentiated synthesis was not pursued from this molecule. This observation is in accordance with the observations of Hetenyi et al. (Hetenyi et al., 2003) who for a similar compound reported a 9:86:5 ratio corresponding to forms *E,Z*-**S18** : *syn*-**S19** : *anti*-**S19**.

(E/Z)-N-benzylidene-1-(piperidin-2-yl)methanamine (S18) and

***syn/anti*-3-phenyloctahydroimidazo[1,5-a]pyridine (S19)**

To a solution of commercial 2-aminomethylpiperidine (**S17**; 1.46 g, 12.8 mmol) in dry DCM (4 mL) over activated 4 \AA molecular sieves (3 g) was added benzaldehyde (1.20 g, 11.3 mmol). The mixture was stirred for 1 hour at RT, then the liquid phase filtered through Celite and the sieves washed twice with 1 mL CH_2Cl_2 . The combined filtrates were evaporated under reduced pressure to yield a yellow crude oil (2.05 g, 89 %), which was a NMR-spectroscopically pure mixture of compounds **E-S18**, **Z-S18**, **syn-S19** and **anti-S19**. HRMS (TOF ESI $^+$) calcd for $[C_{13}H_{19}N_2]^+ = [MH]^+$: m/z 203.1543, found 203.1536. The ratio of compounds **S19** to compounds **S18** in a range of solvents was calculated from the $^1\text{H-NMR}$ spectra, to see if the desired isomer **S18** could be favoured by an appropriate choice of the solvent. However, no such appropriate solvent was found.

Solvent	CDCl_3	CD_2Cl_2	acetone- d_6	$\text{DMSO}-d_6$	CD_3OD	D_2O
Ratio S19:S18	5:1	6:1	13:2	17:2	13:2	9:2

Complete NMR characterisation of the mixture of isomers was performed in CDCl_3 , and spectra were completely assigned for the majority species **E-S18** and **syn-S19**; characteristic peaks could be assigned for each of the minority species **Z-S18** and **anti-S19** enabling analysis of the proportion of each form in the equilibrium mixture. The ratio **E-S18 : Z-S18 : syn-S19 : anti-S19** in this solvent was determined by ^1H -NMR integration of the distinctive peaks for each isomer, and was calculated as 15:0.5:80:2.5. HSQC supported the spectral assignments.

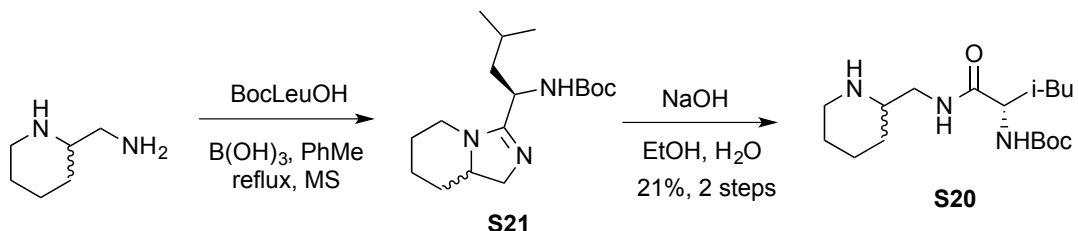
E-S18 (15 %): ^1H -NMR (500 MHz): δ = 8.22 (s, 1H, H7), 7.65-7.64 (m, 2H, 2 \times H9), 7.31-7.28 (m, 3H, 2 \times H10 + H11), 3.61 (dd, 11.8 Hz & 3.2 Hz, 1H, H6), 3.34 (dd, 11.6 & 8.5 Hz, 1H, H6'), 2.96-2.95 (m, 1H, H1), 2.80-2.79 (m, 1H, H5), 2.55 (td, 11.9 Hz & 2.3 Hz, H1'), 1.61 (d, 12.5 Hz, 1H, H4), 1.53-1.50 (m, 1H, H2), 1.40-1.33 (m, 1H, H2'), 1.31-1.26 (m, 2H, 2 \times H3), 1.18-1.16 (m, 1H, H4') ppm. ^{13}C -NMR (125 MHz): δ = 162.2 (C7), 136.1 (C8), 130.7 (C11), 128.6 (2 \times C9), 128.2 (2 \times C10), 67.8 (C6), 56.9 (C5), 46.8 (C1), 30.8 (C4), 26.3 (C2), 24.7 (C3) ppm.

syn-S19 (80 %): ^1H -NMR (500 MHz): δ = 7.38 (d, 7.8 Hz, 2H, 2 \times H9), 7.25 (~t, 7.4Hz, 2H, 2 \times H10), 7.22-7.20 (m, 1H, H11), 3.91 (s, 1H, H7), 3.00 (dd, 9.2 Hz & 6.5 Hz, 1H, H6), 2.73 (~t, 9.5 Hz, 1H, H6'), 2.66-2.65 (m, 1H, H1), 2.22-2.21 (m, 1H, H5), 1.85 (td, 11.2 Hz & 3.1 Hz, 1H, H1'), 1.79-1.70 (m, 2H, H3 + H4), 1.52-1.40 (m, 2H, 2 \times H2), 1.30-1.26 (m, 1H, H4'), 1.22-1.16 (dt, 12.8 Hz & 3.6 Hz, 1H, H3') ppm. ^{13}C -NMR (125 MHz): δ = 141.0 (C8), 128.5 (2 \times C10), 128.3 (C11), 127.9 (2 \times C9), 82.7 (C7), 63.8 (C5), 50.6 (C6), 48.8 (C1), 29.1 (C4), 25.2 (C2), 24.2 (C3) ppm.

Z-S18 (0.5 %): ^1H -NMR (500 MHz) characteristic peak: δ = 8.00 (d, 7.9 Hz, 2H, 2 \times H9) ppm. ^{13}C -NMR (125 MHz) characteristic peaks: δ = 165.0 (C7), 129.6 (2 \times C9) ppm.

anti-S19 (2.5 %): ^1H -NMR (500 MHz) characteristic peak: δ = 4.89 (s, 1H, H7) ppm. ^{13}C -NMR (125 MHz) characteristic peaks: δ = 141.5 (C8), 77.9 (C7) ppm.

Cyclisation spacer substrate, adopted route:



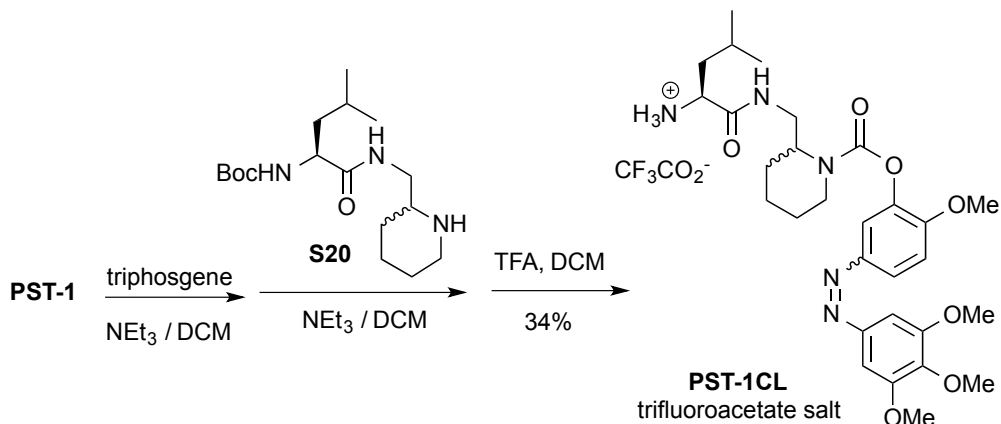
Only two applicable references (Mylavarapu et al., 2007; Thorn-Seshold et al., 2012) were found for a non-racemising, regioselective procedure for the peptide coupling to a primary amine in the presence of a secondary amine. The procedure of Mylavarapu *et al.* (Mylavarapu et al., 2007) was explored first, but using activated 4 \AA molecular sieves instead of a Dean-Stark trap. The product was however assigned as amidine **S21**, formed by a second, intramolecular dehydration, representing a facile synthesis of α -chiral amidines. Basic hydrolysis was found to give desired compound **S20**.

regioselectively. Although this procedure was found to give a lower yield than the DCC-mediated coupling previously reported for **S20** (Thorn-Seshold et al., 2012), it is both more atom-economical and environmentally-friendly, and is therefore reported here.

N'-tert-butoxycarbonyl-L-leucyl-(piperidin-2-ylmethyl)amide (S20**)** (Thorn-Seshold et al., 2012)

N'-tert-butoxycarbonyl-L-leucine (2.08 g, 8.99 mmol) was added to a flask containing dry toluene (60 mL) and activated 4Å molecular sieves (10.6 g). The mixture was heated to 60 °C until the amino acid had dissolved, then boric acid (67 mg, 1.1 mmol, 0.1 eq) and 2-aminomethylpiperidine (1.027 g, 9.00 mmol) were added. The solution yellowed and was stirred for 16 h at 113 °C under a condenser with a closed air atmosphere. The mixture was then filtered, washed with sat. aq. Na₂CO₃ to eliminate the unreacted acid, and evaporated under reduced pressure yielding a crude red oil containing a majority of **S21** (ESI(+): m/z = 310 Th, [MH]⁺). To the crude oil were added EtOH (30 mL), H₂O (20 mL) and NaOH (6 g, 250 mmol), and the solution was stirred overnight at RT. The basic solution was extracted with DCM (3×30 mL) and the combined organic extracts rinsed with brine (20 mL) and dried over Na₂SO₄, filtered and evaporated to yield a crude yellow oil which was filtered through a silica pad using 1:1:0 → 1:1:1 EA:Cy:MeOH to give **S20** as a yellow oil (630 mg, 1.92 mmol, 21 %), identical by NMR to that produced by the reported method (Thorn-Seshold et al., 2012).

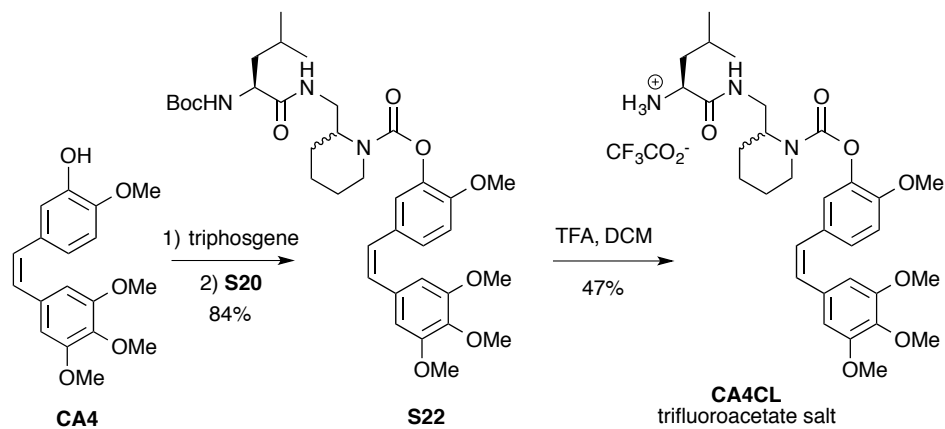
Use of cyclisation spacer substrate:



Caution: phosgene, liberated by amine-mediated decomposition of triphosgene, has boiling point 8 °C, is highly toxic and corrosive and can react violently with water or other nucleophiles especially if the reaction is in homogenous media. Reactions were kept cold to avoid boil-off of phosgene. Excess phosgene was caught apparently quantitatively during evaporation in a primary liquid nitrogen trap (a backup trap was employed but always found empty); it was destroyed when still cold by its dropwise addition to a vigorously stirred, cold mixture of 2-aminoethanol (1 mL) and ethanol (5 mL) in dichloromethane (20 mL) in a well-ventilated hood.

(2-methoxy-5-((3,4,5-trimethoxyphenyl)diazenyl)phenyl) 2-((L-leucinamido)methyl)piperidine-1-carboxylate (PST-1CL), 2,2,2-trifluoroacetate salt

To a solution of **PST-1** (13 mg, 0.041 mmol) in DCM (3 mL) under nitrogen atmosphere in an ice bath, were added a solution of triphosgene (60 mg, 0.20 mmol) in DCM (1 mL), then, dropwise, triethylamine (0.10 mL). The solution was stirred in the cold for 30 min while the colour changed to yellow-brown, then the volatiles were evaporated at high vacuum. To the residue under nitrogen were added a solution of NEt₃ (0.15 mL) and **S20** (16 mg, 0.045 mmol) (Thorn-Seshold et al., 2012) in DCM (3 mL), and the mixture stirred for 2 h at room temperature. The volatiles were evaporated, and a solution of TFA (2 mL) in DCM (2 mL) was added. The purple solution was stirred at room temperature for 30 min. The volatiles were removed at 0.4 mbar until the purple residue had become yellow-brown, indicating removal of excess TFA. Chromatography on 5:1:0→1:1:0→1:1:1 Hx:EA:MeOH returned **PST-1CL** as the 2,2,2-trifluoroacetate salt (9.5 mg, 0.014 mmol, 34%; R_f = 0.54 on 1:1:1 Hx:EA:MeOH, FeCl₃) as a brown viscous oil. ¹H-NMR (400 MHz, DMSO-d₆): δ = 7.87 (dd, 8.7 & 2.4 Hz, 1H), 7.63 (d, 2.5 Hz, 1H), 7.32 (d, 8.9 Hz, 1H), 7.23 (s, 2H), 6.21 (s, 1H), 3.90 (s, 3H), 3.90 (s, 3H), 3.89 (s, 6H), 4.51-4.23 (m, 2H), 3.86-3.02 (m, 4H overlapped), 1.82-1.61 (m, 1H), 1.58-1.34 + 1.12-1.06 (m+m, 8H), 0.85-0.80 (m, 6H) ppm. LCMS(+): t_{ret} = 2.92 & 3.41 min, each 572 Th = [MH]⁺; the first peak was assigned as the Z isomer due to its absorbance shoulder centred at 450 nm. HRMS (ESI+) calcd for [C₂₉H₄₂N₅O₇]⁺ = [MH]⁺: m/z 572.30788, found 572.30867.



2-methoxy-5-((Z)-3,4,5-trimethoxystyryl)phenyl 2-((N'-(*tert*-butoxycarbonyl)-L-leucinamido)methyl)piperidine-1-carboxylate (S22)

Combretastatin A-4 (Pettit et al., 1989) (**CA4**) was synthesised by Dr. Jean-Christophe Mulatier (ENS-Lyon) as described (Harrowven et al., 2006). To **CA4** (34 mg, 0.11 mmol) under argon atmosphere in an ice bath were added CH₂Cl₂ (2 mL) and diethylisopropylamine (60 mg), then, dropwise, a solution of triphosgene (47 mg, 0.16 mmol) in CH₂Cl₂ (2 mL). The solution was stirred for 60 min in the cold then the volatiles evaporated at high vacuum. To the residue under nitrogen were added CH₂Cl₂ (2 mL), diethylisopropylamine (25 mg), and **S20** (100 mg, 0.31 mmol). After

stirring for 1 h warming to room temperature, the volatiles were evaporated and the crude chromatographed on 5:1→1:1 Cy:EA, yielding **S22** (61 mg, 0.09 mmol, 84%; $R_f = 0.25$ on 1:1 Cy:EA, Han) as a colourless oil. $^1\text{H-NMR}$ (500 MHz, CD₃OD): $\delta = 7.15\text{-}7.07$ (m, 2H), 6.88-6.83 (dd, 8.3 & 3.4 Hz, 1H), 6.53 (s, 1H), 6.53 (s, 1H), 6.45 (\sim s, 2H), 5.08 (s br, 1H, carbamate), 4.55-4.33 (m, 1H), 4.18-4.02 (m, 2H), 3.84 (\sim s, 6H), 3.72 (s, 3H), 3.72 (s, 3H), 3.76-3.42 (m, 2H), 3.14-2.85 (m, 1H), 1.75-1.38 (m overlapped, 9H), 1.42+1.41 (s+s, 9H, rotamers), 0.95-0.86 (m, 6H) ppm. $^{13}\text{C-NMR}$ (125 MHz, CD₃OD): $\delta = 172.9, 155.6, 155.5, 152.9 (\times 2), 150.6, 140.3, 137.1, 132.5, 130.2, 129.4, 128.7, 127.1, 123.6, 112.3, 105.9 (\times 2), 79.8, 60.9, 56.3, 55.9 (\times 2), 53.1, 51.2, 41.7, 40.4, 39.3, 28.3 (\times 3), 26.2, 25.1, 24.7, 22.9, 21.9, 19.2$ ppm. DIMS(+): 670 Th = [MH]⁺. MS (ESI+) calcd for [C₃₆H₅₂N₃O₉]⁺ = [MH]⁺: m/z 670.4, found 670.4.

(Z)-1-(((1-((2-methoxy-5-(3,4,5-trimethoxystyryl)phenyl)2-((L-leucinamido)methyl)piperidine-1-carboxylate (CA4CL), 2,2,2-trifluoroacetate salt

To **S22** (53 mg, 0.079 mmol) were added DCM (1 mL) and TFA (1 mL) and the mixture stirred at room temperature under argon for 1 h. After evaporation of the volatiles, chromatography on 1:1:0→1:1:1 Cy:EA:MeOH returned **CA4CL** (25 mg, 0.035 mmol, 47%; $R_f = 0.32$ on 2:2:1 Cy:EA:MeOH, Nin) as a colourless solid. As reported for similar molecules (Thorn-Seshold et al., 2012), NMR resolved some peak sets resulting from diastereomers/rotamers/conformers; these are reported by group as eg. “X+X” to highlight which structural group is responsible for which peak set. $^1\text{H-NMR}$ (400 MHz, CD₃OD): $\delta = 7.03$ (dd, 8.5 & 2.1 Hz, 1H), 6.95-6.88 (m, 2H), 6.48 (s, 1H), 6.46 (s, 1H), 6.40 (s, 1H), 6.39 (s, 1H), 4.45-4.31 (m, 1H), 4.08-3.90 (m, 1H), 3.72 + 3.72 (each s, total 3H), 3.65 + 3.64 (each s, total 3H), 3.62-3.55 (m, 1H), 3.58 + 3.57 (each s, total 6H), 3.47-3.40 (m, 1H), 3.28-3.22 (m, 1H), 3.15-2.93 (m, 1H), 1.68-1.10 (m, 9H), 0.91-0.78 (m, 6H). $^{13}\text{C-NMR}$ (100 MHz, CD₃OD): $\delta = 170.8, 161.80$ (q, 33.8 Hz), 154.5, 152.8 + 152.8 ($\times 2$), 150.7, 140.1, 136.9 + 136.8, 132.8 + 132.8, 130.0, 129.3 + 129.1, 128.2, 127.2, 122.9, 116.7 (q, 292 Hz), 112.0, 105.9, 105.8, 59.8, 55.1 + 55.1, 55.1 + 55.0 ($\times 2$), 52.0 + 51.8, 50.9, 41.0, 40.2, 38.0, 25.8+25.1, 24.1 + 24.0, 22.1, 21.9 + 21.8, 20.7 + 20.5, 18.6 ppm. DIMS(+): 570 Th = [MH]⁺. HRMS (ESI+) calcd for [C₃₁H₄₄N₃O₇]⁺ = [MH]⁺: m/z 570.3174, found 570.3156.

Part B: Photocharacterisation *in vitro*

The rationale for the choice of isomerisation parameters to determine, and the methods for their measurement / modelling, are explained in **Appendix 1**. Photocharacterisations were performed only for the non-prodrug compounds, as the prodrugs could be expected to function as slow-release sources of these active cores and so to have similar photoisomerisation requirements. Important quantities determined are $\epsilon_E(\lambda)$ and $\epsilon_Z(\lambda)$ [the molar absorptivities of the *trans* and *cis* species respectively], $\phi(\lambda)$ [the simulated fraction of *cis* at the photostationary state], $E(\lambda)$ [a parameter estimating the bulk efficiency of photoisomerisation as a function of irradiating wavelength], and τ [the halflife of spontaneous thermal *cis*→*trans* reversion].

Spectrophotometry equipment

Absorption spectra in cuvette (“UV-Vis”) were acquired on a Varian CaryScan 50 (1 cm, 100 µL or 1 mL volume) with Peltier cell temperature control unit maintained at 37 °C, in PBS at pH~7.4 containing 20% MeCN. A TILL Photonics Polychrome V monochromator with a fibre optic cable output directed into the cuvette was used to perform photoisomerisation studies by UV-Vis spectrophotometry although even single low-power LEDs were equally successful in providing repeatable monochromatic photoisomerisation. Separated spectra of *trans* and *cis* forms were acquired from the inline Diode Array Detector on the AGILENT 1260 SL coupled LC-MS system after HPLC separation as described in Part A.

B.1: *trans*- and *cis*- absorption spectra

The *trans*- and *cis*-isomers of each for the non-prodrug compound were separated by HPLC and $\epsilon^*_E(\lambda)$ and $\epsilon^*_Z(\lambda)$ were measured on the inline ultraviolet/visible Diode Array Detector; these were then scaled as outlined in **Appendix 1** to derive the molar absorptivities $\epsilon_E(\lambda)$ and $\epsilon_Z(\lambda)$ (**Figure S1A**). The parameters λ_{strong} (peak absorption wavelength of the *trans* form), $\epsilon_E(\lambda_{\text{strong}})$ and λ_{iso} (the isosbestic point) were also determined, in PBS containing 20% MeCN, at pH = 7.4 unless indicated otherwise (**Figure S1B**; see also **Appendix 1**). This illustrates the **PST** compounds’ large single-photon absorption coefficients within the *in vivo* compatible wavelength range, which especially distinguish them from the prior art in stilbene tubulin inhibitors. Such strong absorption coefficients, coupled with the high quantum efficiencies known to be typical of azobenzene photoisomerisation (Beharry and Woolley, 2011a; Knoll, 2003), enable efficient single-photon photoisomerisation of the **PST** compounds in both directions *cis* → *trans* and *trans* → *cis*, with low power irradiation as is *in vivo* compatible, cheap and practical.

B.2: Calculated $\phi(\lambda)$ and $E(\lambda)$

$\phi(\lambda)$ and $E(\lambda)$ were calculated as per **Appendix 1** and are presented in **Figure S1A**. These indicate that even small structural variations may substantially alter both the proportion of the *cis* form in the photostationary state at different wavelengths, and the relative efficiency of approaching those photostationary states. This illustrates the possibility of structural modifications within this scope being used to give spectral tuning, eg. for better biological light penetration by red-shifting so that both *trans*→*cis* and (especially) *cis*→*trans* photoisomerisations may be conducted more efficiently and to a greater extent at longer wavelengths.

B.3: Reversible *trans*↔*cis* photoisomerisation

$A(\lambda_{\text{strong}})$ was measured over time, while the monochromator applied λ_{irrad} alternating between two values λ_1 and λ_2 , chosen to induce bulk *trans*→*cis* and bulk *cis*→*trans* isomerisation respectively. Typical results were presented for **PST-1** in **Figure 1D**, measuring the absorbance of **PST-1** (18 μM) at $\lambda_{\text{strong}}=378$ nm, while the irradiating wavelength was held alternately at $\lambda_1=388$ nm (50 s; bulk *trans*→*cis*) then $\lambda_2=508$ nm (180 s, bulk *cis*→*trans*). Higher absorbance corresponds to a greater amount of *trans* isomer: an absorbance of 0.27 corresponds to ~5:1 *trans:cis* isomeric ratio in the sample, and an absorbance of 0.12 corresponds to ~1:2. Note that this bulk *trans*→*cis* isomerisation at 388 nm is significantly faster than the bulk *cis*→*trans* isomerisation at 508 nm, although the monochromator equipment used delivers light at 508 nm with approximately 1.5 times the intensity of the light delivered at 388 nm. This is consistent with the expectation that photoisomerisation toward the respective photostationary states should be significantly more efficient at 388 nm than at 508 nm for this compound, since $E(388)/E(508) = 0.04$.

PST compounds were bulk-photoisomerised hundreds of times over a timescale of hours (50 representative cycles are summarised in **Figure 1D**), such that the majority species in a sample was alternated between the *trans*-isomer and the *cis*-isomer. This proceeded without any detectable photobleaching, or decreases in photoswitching speed, or photoswitching efficiency or limiting isomeric percentage obtained, despite the fact that measurements were conducted in non-degassed PBS solution (10% MeCN) under open air atmosphere at 37 °C. This highlights the extreme robustness of the **PST** compounds towards photochemical reaction or damage in an aqueous environment. This robustness is a key advantage of the azobenzene **PST** compounds when compared to the prior art advancing stilbene photoisomerisation (Bisby et al., 2013), a process known to give extensive and rapid degradation (eg to phenanthrenes via 6π-electrocyclisation-oxidation) when biologically relevant conditions (eg. presence of dissolved oxygen) are used (Mallory and Mallory, 2004). These results thus demonstrate that photocontrolled *trans*↔*cis* isomerisation of the **PSTs** is fully reversible, in a highly robust fashion, which is practical to implement under biologically relevant conditions.

B.4: Thermal *cis*→*trans* reversion halflives

Thermal reversion halflives τ were measured as per **Appendix 1**, in PBS at pH = 7.4 unless indicated otherwise, containing 20% MeCN to ensure solubility (**Figure S1B**). These reversion halflives show that structural variations within the scope of photoswitchably bioactive **PST** designs can greatly alter the timescale of spontaneous *cis*→*trans* reversion. Therefore we anticipate that different **PSTs** will be suited to maintain *cis/trans* gradients on different spatial scales, *e.g.* for subcellular, cellular and tissue level studies, or for experiments carried out over significantly different time scales (eg. seconds to minutes for experimental biology applications, or hours to days for biomedical applications).

ASSAYS *in vitro*, *in cellulo*, & *in vivo*

Materials and Methods

Safety Precautions

The photoswitchable compounds examined here are cytotoxic and should be treated cautiously as for standard chemotherapeutics. In case of spills or splashes, ethyl acetate might be used to remove the compounds from the affected areas without favouring their percutaneous transport; traces or waste may be destroyed if necessary by KMnO₄.

Biochemical Assays *in vitro*

Radioligand scintillation proximity assay (SPA): The competitive tubulin-binding assay was modified from literature procedure (Tahir et al., 2000). The assay uses porcine brain tubulin, where random surface lysines have been covalently modified with long chain biotin linkers, in conjunction with streptavidin-coated yttrium silicate SPA beads, so that only the tritiated colchicine which is bound to tubulin (at the CDI site) is held in close proximity to the SPA bead and gives rise to a scintillation signal upon radioactive decay. Briefly, a tritiated colchicine solution was prepared by diluting commercial tritiated colchicine stock (Perkin-Elmer, specific activity 83.5 Ci/mmol) threefold with “cold” colchicine (Sigma). SPA assays were then performed in clear-bottom, white 96-well plates by mixing 0.5 µg of biotinylated tubulin (Cytoskeleton, Tebu-Bio), 0.08 mg streptavidin-coated yttrium silicate SPA beads (Perkin Elmer), and the inhibitor (**PST-1** or combretastatin A4 (**CA4**, Sigma)), in General Tubulin Buffer (80 mM PIPES pH=6.8, 0.5 mM EGTA, 2 mM MgCl₂) supplemented with 1 mM GTP (final volume 100 µL), containing 1% acetonitrile and 0.22% ethanol for inhibitor solubility. To initiate the assay tritiated colchicine solution (0.08 µM final concentration) was added and plates were incubated at 37 °C, with shaking for 70 min, then without shaking for 15 minutes to allow the beads to settle. The radioactive counts were then directly measured using a

Wallac Microbeta 1450 scintillation counter. The nonspecific background signal (determined using controls without tubulin) was subtracted, and as the SPA photons can be appreciably absorbed by **PST-1** in bulk solution at higher concentrations, we also applied an experimentally determined colour quenching correction to the **PST-1** data. The CDI site occupation by ^3H -colchicine was calculated as a percentage relative to the positive control (counts determined without competitive inhibitor). Dark conditions were achieved by preparing the assay under red-light conditions and running it inside light-shielded boxes. In our hands, permanent assay illumination at 390 nm resulted in almost total loss of specific binding signal, presumably by 4π electrocyclisation of colchicine to non-binding lumicolchicine. Therefore appropriate "390 nm" conditions were achieved using pulsed irradiations at 390 nm (75 ms every 45 s), applied by the Disco timed illumination system using a 96-LED array (see below); the control signal under these conditions was almost indistinguishable from that obtained under dark conditions, indicating no significant photodegradation of the radioligand. Results are expressed as mean percentage of colchicine binding relative to the positive control (without inhibitors), +/- standard deviation, calculated from 3 experiments performed in quadruplicates. Graphical representations and statistical analysis of the data were performed using GraphPad Prism (GraphPad Software, La Jolla, CA, USA). Four-parameter curve fitting for sigmoidal dose-response curves with a variable slope was used to determine the EC₅₀ values for **CA4** and for **PST-1** under 390 nm illumination. Results obtained for *trans*-**PST-1** (dark conditions) did not fit a sigmoidal model (indicating no strong competition for CDI site binding), so a second order polynomial was fitted instead.

In vitro tubulin polymerisation assay: Tubulin from porcine brain with 30% MAPs (Microtubule-associated proteins) was obtained from Cytoskeleton Inc. (Cat. # ML116, Denver, CO, USA). The polymerisation reaction was performed at 2 mg/mL tubulin, in polymerisation buffer (80 mM piperazine-N,N'-bis(2-ethanesulfonic acid) (PIPES) pH=6.9, 0.5 mM EGTA, 2 mM MgCl₂), in a cuvette (100 μL , 1 cm path length) in a Varian CaryScan 50 with Peltier cell temperature control unit maintained at 37 °C. Tubulin was first incubated for 10 min at 37 °C with **PST** (in 1 % MeCN to ensure solubility) in buffer without GTP. Then GTP was added to 1 mM final concentration with mixing, and the change in absorbance at 340 nm (Lin et al., 1988) was monitored for 15 min. Throughout the whole experiment samples were kept shielded from ambient light ("dark") or exposed to illumination at 390 nm using the monochromator-fibre optic setup described in **Part B**.

Cell Culture

MDA-MB-231, HeLa and HEK-293T cells were grown in Dulbecco's modified Eagle's medium (DMEM, PAN-Biotech P04-03550), and Jurkat cells were maintained in Roswell Park Memorial Institute medium (RPMI 1640, PAN-Biotech P04-16500). Medium was supplemented with 10% heat-inactivated fetal calf serum, 100 U/mL penicillin and 100 $\mu\text{g}/\text{mL}$ streptomycin (Sigma Aldrich,

P4333) and additionally with 1% pyruvate (Merck) for Jurkat cell culture. Cells were grown at 37°C in a 10% CO₂ atmosphere. Prior to assays, cells were transferred to phenol red free medium (DMEM, PAN-Biotech P04-03591 or RPMI 1640, PAN-Biotech P04-16515). One day post plating, **PSTs** were applied and cells were exposed to lighting regimes as indicated.

Use of Photoswitchable Compounds in Cell Culture: Long-term experiments were prepared under ambient light (pipetting, dilutions, dosage etc.). For short-term experiments such as video microscopy, **PSTs** were stored in the dark prior to use, and red light/dark-room conditions were used when setting and running experiments. Irradiated cell culture was performed using a cheap, easily self-built computer-controlled system of arrays of LEDs, which achieved parallel throughput (eg. >30 plates) for repeatable screening of irradiation conditions (**Figure S6**). Each array irradiated a standard 24-well or 96-well cell culture plate, and these were kept in separate light-proof gas-permeable cardboard boxes in the incubator. The choice of LEDs plugged into each array determined the wavelength at which its well plate was irradiated. The timing sequences (defined by light pulse length t_{IR} , and interval t_{pause} between pulses) were defined by a programmed microcomputer (Arduino Uno Mega), and actuated to power the arrays *via* a multichannel switchboard. Either one or two arrays were used per well plate (eg. one illuminating from the bottom, and an optional second array illuminating from the top down at a different wavelength, on a synchronised but different timing sequence if desired), thus enabling pulsed or continuous implementation of eg. toxic regime, strong rescue regime, weak rescue regime, or dark rescue regime protocols (see **Appendix 4**). Typical settings for the toxic regime were 390 nm with $t_{IR} = 75$ ms, $t_{pause} = 15$ s; typical settings for the rescue regime were twin pulses with the first pulse component being 390 nm with eg. $t_{IR} = 75$ ms, $t_{pause} = 30$ s administered from a 390 nm array below the well plate, and synchronously with the end of this component, starting a second pulse component at 515 nm with $t_{IR} = 375$ ms, $t_{pause} = 30$ s from a 515 nm array above the well plate (see setup represented in **Figure S6A**). Arrays and switchboards were assembled by hand from components bought at a home improvement hardware store (Conrad). The Arduino programs used, circuit designs, parts lists, schematics and build guide for both arrays and switchboards are given in full in **Appendix 2**. The following central-wavelengths of LEDs were used in this study (in nm): 370, 380, 390, 400, 410, 425, 435, 450, 465, 475, 490, 505, 515, 525, and 535 nm; all LEDs were bought from Roithner Lasertechnik GmbH, as 4V / 20 mA / 5 mm units, and the corresponding Roithner part numbers are VL370-5-15, RLS-UV380, VL390-5-15, RLS-UV400, VL410-5-15, VL425-5-15, LED435-12-30, LED450-04, RLS-B465, B56L5111P, LED490-03, B5-433-B505, LED515-10-30, B5-433-B525, and LED535-01 respectively. The LEDs were removably plugged into sockets, to give maximum modularity to the equipment. Only one wavelength of LED was used per array, and arrays at different wavelengths were kept in separate boxes (save for the rescue protocols). We consider this crucial since with standard, clear well plates, light scattering from one well across the whole plate was often observed to be significant enough to compromise results. For the same

reasons, for microscopy, **Photostatins** were applied only in the moment of imaging (by contrast to e.g. applying the **PST** to all wells, then imaging them one-by-one) to avoid similarly compromising results by light scattering.

Cell Biology Assays

Crystal violet staining was adapted from standard protocol (Saotome et al., 1989). Briefly, MDA-MB-231 cells were seeded on 96-well microtitre plates at 5000 cells/well. After 24 h, cells were treated with the test compounds, shielded from ambient light inside light-proof boxes, and exposed to the appropriate light regimes; here, the toxic regime was defined as 390 nm pulses of 75 ms every 15 s. In these experiments, 0.1% DMSO and 3% MeCN were present as cosolvents for all compounds at all the concentrations tested, to ensure full solubility of all compounds and intercomparability of the data. Following 48 h of treatment, cells were stained with crystal violet solution (0.5% crystal violet in 20% methanol) for 10 min at room temperature. Unbound crystal violet was removed by rinsing with distilled water and cells were subsequently air-dried. Crystal violet was then eluted from cells with 0.05 M sodium citrate in 50% ethanol. The absorbance of crystal violet is proportional to the cell number and was determined at 590 nm with a FLUOstar Omega microplate reader (BMG Labtech). For statistical analysis, the absorbance readings for untreated controls (cosolvent only) were set as 100% of viable cells. Results are given as the mean percentage of viable cells relative to these controls, +/- standard deviation (SD) from 4 representative experiments performed in triplicates. Graphical representations and statistical analysis of the data were performed using GraphPad Prism (GraphPad Software, La Jolla, CA, USA). Four-parameter curve fitting for sigmoidal dose-response curves with a variable slope was used and the EC₅₀ values and Hill coefficient were calculated.

MTT assay: Mitochondrial dehydrogenase activity in HEK-293T or HeLa cell lines was quantified by spectrophotometrically measuring the reduction of 3-(4,5-dimethylthiazol-2-yl)-2,5-diphenyl tetrazolium bromide (MTT) to formazan, according to standard protocol (Cushman et al., 1991). Cells were seeded on 96-well microtitre plates. After 24 h, cells were treated with **PSTs**, shielded from ambient light with light-proof boxes, and exposed to the appropriate light regimes. Following 48 h of treatment, cells were incubated with 0.5 mg/mL MTT for 3 hours at 37 °C. The formazan crystals were dissolved in DMSO, and absorbance at 550 nm was measured using a FLUOstar Omega microplate reader (BMG Labtech). Results represent mean +/- SD, which are proportional to the cell number.

Nuclear fragmentation and cell cycle analysis: Following treatment with **PST** under the indicated light regime, cells were harvested on ice and incubated in a hypotonic buffer [0.1% sodium citrate, 0.1% Triton X-100 and 50 µg/mL propidium iodide (PI)] for 30 min at 4 °C. Following the PI staining cells were analysed by flow cytometry using a FACSCalibur flow cytometer (Becton Dickinson,

Heidelberg, Germany) run by Cell Quest Pro Software (Becton Dickinson). The cell cycle analysis was subsequently performed using FlowJo software (Tree Star Inc., Ashland, OR, USA) employing the Watson (Pragmatic) fitting model. Cells with subdiploid DNA content (inferior to G₁ phase content) were considered as apoptotic in accordance with Nicoletti (Nicoletti et al., 1991). Results represent means +/- SD calculated for triplicates from one representative experiment out of three independent trials.

Propidium iodide exclusion assay: Membrane integrity was assessed as a marker of cellular viability, *via* examining the uptake of propidium iodide (PI) in non-permeabilised cells. Following treatment with **PST** under the appropriate light regime, cells were harvested, stained with 5 µg/mL PI in PBS containing 2% FCS (foetal calf serum), and immediately analysed by flow cytometry using a FACSCalibur flow cytometer (Becton Dickinson, Heidelberg, Germany) with Cell Quest Pro Software (Becton Dickinson). Data are expressed as means +/- SD of one representative experiment out of three independent trials performed in triplicates.

Western Blot: Following 48 h of treatment with **PST-1P** in the dark or under 390 nm pulsed illuminations, HeLa cells were lysed using RIPA buffer (50 mM Tris-HCl pH=7.5, 150 mM NaCl, 1% SDS, 0.5% Na-deoxycholate, 1% Triton X 100, protease inhibitor cocktail). Protein concentration in the cell lysates was determined using Roti Quant Universal (Carl Roth) colorimetric protein concentration detection kit according to the manufacturer's instructions. For immunoblotting, equal amounts of protein extracts were resolved by SDS-PAGE in 12% polyacrylamide gel and transferred onto a PVDF membrane. The membranes were blocked with Roti Block solution (Carl Roth) and probed with anti-PARP-1 (Cell Signaling) and anti-β-actin (Millipore) primary antibodies and subsequently with HRP goat anti-rabbit (Cell Signaling) and HRP goat anti-mouse (Santa Cruz Biotechnology) secondary antibodies. The immunoreactive bands were detected by the ECL method and visualized using Fujifilm LAS-3000 Luminescent Image Analyzer.

Confocal microscopy, fixed cell imaging: MDA-MB-231 cells were seeded on coverslips and incubated with **PST-1** under dark or toxic regime (390 nm pulses of 200 ms every 2 min) for 20 h. Then, cells were washed with pre-warmed PBS, and cell extraction buffer (80 mM PIPES pH 6.8; 1 mM MgCl₂, 5 mM ethylene glycol tetraacetic acid (EGTA) dipotassium salt and 0.5% Triton X-100) was added to remove monomeric and dimeric tubulin subunits. After 30 s of extraction, cells were fixed for 10 min with 0.5% glutaraldehyde. Following glutaraldehyde quenching with 0.1% NaBH₄ in PBS for 7 min, coverslips were blocked with PBS containing 0.2% bovine serum albumin. Immunostaining was performed using anti-α-tubulin antibody (ab18251) and AlexaFluor 488 secondary antibody (A 11008), purchased from Abcam (Cambridge, UK) and Invitrogen (Darmstadt, Germany), respectively. Hoechst 33342 (bisbenzimide), purchased from Sigma Aldrich (Taufkirchen, Germany), was used at a concentration of 1 µg/mL for nuclear staining. Cells were mounted with

FluorSave reagent (Calbiochem) and analysed with a Zeiss LSM 510 Meta confocal microscope (Jena, Germany). Acquired images were processed using ImageJ open-source software (National Institutes of Health). Representative images are shown. White scale bars correspond to 20 μ m.

Confocal microscopy, live cell imaging: HeLa cells were plated on 8-well ibiTreat μ ibidi slides (ibidi, Martinsried, Germany) 24 h prior to transfection. Cells were transiently transfected with EB3-mCherry plasmid using jetPRIME reagent (Polyplus) according to manufacturer's indications. Cells were imaged twenty-four hours later using an UltraVIEW VOX spinning disk confocal microscope (PerkinElmer) operated with the Velocity software. During imaging cells were maintained at 37°C in a 5% CO₂ atmosphere. Cells were imaged briefly prior to the application of the test solution, in order to establish a reference point for basal EB3 dynamics, then treated either with **PST-1** (final concentration 10 μ M, with 0.5 % MeCN cosolvent) or else with cosolvent only, and incubated for 10 min in the dark. Then, cells were imaged at 561 nm at a rate of 17 frames per minute, with alternating phases of pulsed photoisomerisation illuminations at 514 nm and 405 nm (one 100 ms pulse every 3.53 s) in between of the imaging, with each phase lasting for 2 min (34 frames). EB3 comets were tracked using the MATLAB program u-track (Applegate et al., 2011). For each cell, we selected two to three regions of interest (ROI) of 0.22 x 0.22 μ m for tracking. This increases the efficiency and accuracy of comet detection by allowing us to exclude the region around the centrosome, where the fluorescent signal background is too strong to allow a correct detection of the comets. We chose conservative parameters for tracking to avoid detecting false positive signals (confirmed by visual inspection of the tracked movies; parameters are shown in the table below); consequently, the number of EB3 dots detected by the program can be somewhat underestimated (as in **Movie S3**).

Detection parameters	Gaussian filter parameters		Min (pix)	1
			Max (pix)	4
	Watershed segmentation parameters		Min (std)	6
			Step size (std)	1
Tracking parameters	Parameters	Max gap to close (frame)		3
		Min length of track segments from 1 st step (frame)		2
	Frame-to-frame linking	Brownian search radius (pix)		1-13
		Multiplication factor for Brownian search radius		2
		Number of frames for nearest neighbor distance calculation		3
	Gap closing, merging and splitting	Max forward angle (°)		30
		Min backward angle (°)		10
		Max shrinkage factor		1
		Fluctuation radius		1

For each ROI, at each illumination phase, we measured the number of EB3 dots, their average lifetime, average travelled distance and average speed (distance/lifetime). The number of EB3 dots was expressed as a percentage of the initial, 561 nm phase comet number, to enable comparison

between ROIs covering different cell areas; other quantities were kept as original values since the 561 nm phase values for these parameters were almost identical between different cells and movies. For each illumination phase, the mean phase values across multiple experiments were then calculated by averaging the values from multiple ROIs from several cells (in total 10 ROI per condition). During 405 nm phases with **PST-1**, EB3 dots were most often entirely undetectable by visual inspection as well as using the u-track program, therefore in such phases the comet parameters were set to 0.

***C. elegans* experiments**

PST-1 experiment: The *C. elegans* fluorescent strain ANA090 (*unc-119(ed3)III*, *ltIs44[pAA173;pie-1::mCherry::PH(PLC1delta1)+unc-119(+)]V* ; *ltIs37[pAA64;pie-1::mCherry::his-58 + unc-119(+)]IV*) was cultured using standard protocols and maintained at 25 °C. This strain allows the visualisation of the cell membrane and histones in the same channel with excitation at 561 nm. To permeabilise the embryo shell and allow the entry of **PST-1** into cells, RNAi against *perm-1* was performed by feeding ANA090 L4 larva on HT115 bacteria for at least 24 h (Carvalho et al., 2011). Embryos were mounted with 40 µM **PST-1** diluted in physiological worm buffer M9 containing 2% MeCN, onto a 2% agarose pad between slide and coverslip. Embryos were imaged using an inverted Zeiss LSM 710 confocal microscope controlled by the ZEN software with a 40× objective. Fluorescence imaging was conducted with 561 nm laser excitation pulses every 968.14 ms using a 3× digital zoom. Photoisomerisations were performed within defined ROIs using 405 nm and 514 nm lasers, with appropriate pulses applied every 30 s. The exposure area was chosen as a circle of diameter between 60—90 pixels (8.3—13 µm), and area irradiation time per pulse varied between 2—5 ms.

Colchicine control experiments: The *C. elegans* fluorescent strain, ANA058 (*oxIs279[pie-1::GFP::histone] II*; *ltIs25[pAZ132, pie-1::GFP::tba-2]*) was cultured using standard protocols and maintained at 25°C. This strain allows the visualisation of microtubules and histones in the same channel with excitation at 491 nm. Embryo shells were permeabilised as per the above procedure. Embryos were placed on a polylysine-coated coverslip and covered with M9 buffer, and 25 µL of colchicine (100 mM) were added. Embryos were imaged using an inverted spinning disc confocal microscope (Leica DMI400, Leica Microsystems, Mannheim, Germany) equipped with a 100× immersion objective and controlled by Metamorph software (version 7.5.6). Images were acquired with an EMCCD Camera (Andor, iXion3 897) every 0.5 s.

Mouse cremaster muscle experiments

Animals: Male C57BL/6 mice at the age of 10-12 weeks were purchased from Charles River (Sulzfeld, Germany). Animals were housed under standard laboratory conditions with free access to

food and water *ad libitum*. All experiments were performed according to German legislation for the protection of animals.

Surgical procedure: The microsurgical preparation of the cremaster muscle was performed as described by Baez with minor modifications (Baez, 1973). Briefly, mice were anaesthetised with an intraperitoneal injection of ketamine/xylazine mixture (100 mg/kg ketamine and 10 mg/kg xylazine). The right cremaster muscle was exposed through a ventral incision of the scrotum. The muscle was opened ventrally in a relatively avascular zone, using careful electrocautery to stop any bleeding, and spread over the pedestal of a custom-made microscopy stage. Epididymis and testicle were detached from the cremaster muscle and placed into the abdominal cavity. Throughout the experiment, the muscle was superfused with phosphate buffered saline (PBS) and was kept at 35°C by using a heating lamp. The body temperature was maintained at 37°C using a heating pad placed under the mouse. At the end of the experiment, the cremaster muscle was excised and processed for immunohistochemistry. Anaesthetised animals were then euthanised by an overdose of pentobarbital (Narcoren, Merial, Hallbergmoos, Germany).

In vivo light-dependent microtubule disruption experiment: Following the cremaster muscle preparation, **PST-1P** (50 µM) was added to the superfusion solution. For activation of **PST-1P**, a single 390 nm LED (VL390-5050, Roithner Lasertechnik, photon output est. 10 mW with cone angle 120°) centered 2 cm above the cremaster was used to supply constant illumination for 40 min. For the dark control, the mouse was kept in the dark. As controls, PBS superfusion was maintained and the mouse was kept in the dark or was irradiated for 40 min using the same 390 nm LED setup. Replicates performed: Active experiment (**PST-1P** + 390 nm): n=3, dark control (**PST-1P**, no illumination, protection from ambient light): n=2, illumination control (PBS + 390 nm): n=2, negative control (PBS only, no illumination, protection from ambient light): n=3.

Immunostaining and Imaging: Immediately after the treatment, the muscle was superfused with microtubule stabilising buffer (80 mM PIPES pH 6.8, 1 mM MgCl₂, 1 mM EGTA, 0.5% Triton X-100 (Sigma Aldrich, Munich, Germany)). Glutaraldehyde was added to a final concentration of 0.5%, to rapidly fix the tissue, and after 10 min, the cremaster muscle was dissected and incubated in 0.1% NaBH₄ in PBS to quench unreacted glutaraldehyde, following standard protocols (Desai et al., 2012). After washing the tissue with PBS, it was blocked for 30 min at room temperature using PBS supplemented with 0.5% Triton X-100 and 2% bovine serum albumin (Sigma Aldrich, Munich, Germany). Staining was performed using anti- α -tubulin antibody YL1/2 (Chemicon, Hofheim, Germany) and Alexa Fluor 546 goat anti-rat secondary antibody. Subsequent nuclear staining was performed using TO-PRO-3 Iodide (642/661) (both from Life Technologies, Carlsbad, CA, USA). The immunostained cremaster muscle was mounted between a glass slide and a coverslip using PermaFluor (Beckman Coulter, Krefeld, Germany). Samples were analysed using a Leica SP5 confocal laser-scanning microscope with an oil-immersion lens (63x; NA 1.40; Leica Microsystems,

Wetzlar, Germany), as described previously (Rehberg et al., 2010). Images were processed with Imaris 7 software (Bitplane, Zurich, Switzerland).

RESULTS

Part C: Cell Biology

Details and build guide for the cell culture “Disco” setup constructed to deliver pulsed light sequences were given in **Materials and Methods** and **Appendix 2**. Discussion of the cell biology assay design is presented in **Appendix 4**.

C.1: Toxicity dependency on pulse frequency and illumination wavelength

Examination of light pulse timing parameters in HEK-293T cell line: Controls for the pulse timings in the toxic regime at 390 nm were performed using MTT assay in HEK-293T cell line over 72 h incubation (in 0.04% MeCN) with **PST-1**. A range of low concentrations of **PST-1** ($\tau \approx 7$ min) were tested, with varied pulse timings. Sequences used were: 1) 50 ms ON / 15 s OFF; 2) 200 ms ON / 60 s OFF; 3) 1 s ON / 5 min OFF; 4) 1 s ON / 25 min OFF; and also 5) a double-cycling sequence where a phase of (2 s ON / 7 s OFF) lasting 90 seconds was followed by 120 min without light. These sequences are designed to apply roughly identical *time-average photon flux* to the samples. Results are given in **Figure S2O**, and show (a) that the timing pattern, and not the *total photon flux*, is the main determinant of cytotoxicity, and (b) that the interval t_{pause} between pulses should be on the order of, or less than, the *in vitro*-determined τ for best cytotoxic effects. This experiment therefore indicates that **PST-1** is not acting as a phototoxin, as phototoxicity should not depend on the t_{pause} but only on total irradiation dose. Instead the **PST-1**-induced cytotoxicity is correlated to the time-average concentration of *cis*-**PST**: due to its spontaneous reversion kinetics, only illuminations with $\tau \geq t_{\text{pause}}$ maintain high time-average *cis*-**PST** levels for potent toxicity (see too **Appendices 2 & 4**).

Wavelength-dependency of cytotoxicity in HeLa cell line: Detailed examination of the wavelength-dependency of **PST** toxicity was performed using MTT assay in HeLa cell line over 44 h incubation with **PST-1P** (no cosolvents). Our hypotheses were that (1) PSS is established at all strongly absorbed wavelengths; (2) only the *cis* isomer is responsible for cytotoxicity at biologically relevant doses (<100 μ M), therefore the toxicity profiles should be primarily determined by the PSS’s *cis* content, and should not depend on the total (*cis+trans*) **PST** content. Under these hypotheses, the dose-response curves for different wavelengths would be translated on the horizontal axis [total (*cis+trans*) **PST** content] by a factor corresponding to the %*cis* which is actually contained in the PSS; and the experimental EC₅₀ values [EC₅₀(λ)] should thus correspond to the EC₅₀ for a hypothetical pure-*cis* sample [EC₅₀(*cis*)] as follows:

$$[\text{EC}_{50}(\lambda) \times \text{PSS}_{\text{exp}}(\lambda)] = \text{EC}_{50}(\text{cis})$$

Dose-response curves were established by MTT assay following **PST** treatment under exposure to light at varying wavelengths (370-535 nm and dark) under constant pulse timing (75 ms ON / 15 s OFF) that was intended to establish PSS even at the weakly-absorbed wavelengths (t_{pause} is much smaller than τ). Results are given in **Figure 2C-D** and **Figure S1C**, showing representative dose-response curves and tabulating all the corresponding EC₅₀ values. We had already modelled the PSS by deriving $\phi(\lambda)$ in the Photocharacterisation section (see Part B and **Figure S1A**; the relevant curve is the $\phi(\lambda)$ of **PST-1** since this is the bioactive metabolite of the **PST-1P** prodrug). Therefore, to test our hypothesis, we postulated a reasonable fit as EC_{50(cis)}=0.68 μM; and we back-calculated PSS_{exp(λ)} values, which in **Figure S1C** are tabulated side-by-side with the corresponding PSS_{model} values [=φ(λ)] from Part B.

These results indeed show: (A) that the dose-response curves at 370-525 nm are essentially horizontal translations of each other, while the dark curve has a markedly flatter gradient, and the curve at 535 nm has an intermediate form between the two possibilities; (B) for all wavelengths 370-525 nm, the values of PSS_{exp(λ)} derived under our twin hypotheses are close to the PSS_{model(λ)} values that we calculated in the Photocharacterisation section, despite the many differences of assay conditions and even of readout, and despite that the EC_{50(λ)} values occupy nearly a ten-fold concentration range; (C) the differences between PSS_{exp(λ)} and PSS_{model(λ)} do not reveal a systematic drift which might argue for systematic error (eg, consistent underestimation of the observed toxicity at the UV wavelengths could argue for biochemical photodamage).

We interpret these results as follows: (1) our LED system was appropriate to achieve and maintain PSS at all wavelengths 370-525 nm; and for these wavelengths, (2) the fraction of the *cis* isomer at PSS is appropriately modelled by φ(λ) with λ taken as the nominal peak emission wavelength of the LED type used (despite the known significant bandwidth of LED sources and its variation with voltage and temperature), and (3) for these wavelengths the concentration of *cis* form as reflected in the PSS is the only significant determinant of cytotoxicity since the form of the dose-response curves depends entirely on the *cis* concentration (curve translation according to the %*cis*) and does not change with the *trans* concentration. (4) The dark case, with 100% *trans* isomer, shows that the *trans* form's toxicity (EC₅₀>200 μM) is more than 250× lower than that seen for the *cis* isomer (EC₅₀<0.70 μM), and (6) the *trans* form's primary mechanism of toxicity is different from the *cis*, since the form of the *trans* dose-response curve is substantially different (much flatter curve). (7) The shape of the 535 nm curve is intermediate between the *cis* and *trans* curves, and its PSS_{exp(λ)} is far from our modelled prediction; we hypothesise that the 535 nm LEDs were not intense enough to compensate for the very weak light absorption at this wavelength (cf. **Figure S1A**) therefore the true PSS was not reached, and that the toxicity arising from the small percentage of *cis* generated was comparable to overall toxicity of the remaining percentage of *trans*: so one might estimate approximately 1% *cis* established.

Together with the results presented above and below, these combined data argue that the toxicity resulting from inhibition of tubulin polymerization induced by **PSTs** may be modulated by the combination of (a) the total dose of **PST** applied, (b) the wavelength(s) applied (with regards to their $E(\lambda)$ and $PSS(\lambda)$), (c) the chronological order of the applied wavelength(s), (d) the time-average photon flux and the pulse frequency relative to τ . As $E(\lambda)$, $PSS(\lambda)$ and τ depend intrinsically on molecular design, this highlights the need for rational design to achieve satisfactory light control of **PSTs**' bioactivity. It also shows that lighting and dose conditions can be chosen and tuned to respond to experimental constraints, in a predictive manner, by considering the key isomerisation parameters which can be influenced by chemical design (Beharry et al., 2011a; Beharry and Woolley, 2011b) and then measured experimentally *in vitro*.

C.2. Photoactuated cytotoxicity of PSTs

The cytotoxicities of the **PSTs** under both dark and toxic regimes were assessed using crystal violet staining in MDA-MB-231 cells (**Figure S2A-I**) as detailed in the **Materials and Methods**. For all the **PST** compounds tested, strong dose-dependent toxicity was observed with activating irradiation (toxic regime). Importantly for the rationale of our design of this optically controlled OFF \leftrightarrow ON tubulin polymerisation inhibitor / cytotoxin, the large toxicity enhancement upon irradiation (up to 100 \times in this cosolvent-containing assay), combined with the steepness (nonlinearity) of the dose-response relationships, promises a wide “therapeutic window” of concentrations. For example, up to 10 μ M *trans*-**PST-1P** generates nearly no toxicity, whereas above 200 nM *cis*-**PST-1P** strongly reduces cell viability. One could therefore consider an “optical therapeutic window” of between 200 nM—10 μ M: inside this 50-fold concentration range, **PST-1P** can be applied globally but photoisomerised locally, to give strong localised cytotoxicity without effects in non-irradiated cells.

MTT assays performed in HeLa cells (**Figure S2J-N**) confirmed our results from crystal violet staining performed in MDA-MB-231 cells (**Figure S2A-I**), indicating therefore potent cytotoxic properties of **PSTs** across different cell types.

C.3: G₂/M phase cell cycle arrest (PST-1 and PST-1P)

The effect of **PSTs** on cell cycle progression was assessed by flow cytometry as described in the **Materials and Methods**. Results for **PST-1** were shown in **Figure 3D-E**; additional results are shown in **Figure S3F-H** (MDA-MB-231 cells with **PST-1** and **PST-1P**), **Figure S3I** (HEK-293T cells, **PST-1**) and **Figure S3J** (HeLa cells, **PST-1**). The toxic regime was set here as 390 nm pulses of 350 ms every 5 min; in the rescue regime each 390 nm pulse was immediately followed by 515 nm light pulses of 800 ms; and a 515 nm-only regime with that timing was used as a reference.

No changes in the repartition of the cell cycle phases were observed in the dark regime despite treatment with even up to 100 μ M **PST-1** (**Figure S3F**). This indicates, in accordance with the hypothesis of the study, that *trans-PSTs* do not interact potently with tubulin and that their mechanism of cytotoxicity at very high concentrations is also not related to tubulin. By contrast, *cis-PSTs* showed strong G₂/M phase arrest under the toxic regime mirroring the effect of the **PSTs'** parent compound **CA4** (**Figure 3D-E** and **Figure S3G-J**). Moreover this effect was reduced under the rescue protocol (**Figure S3H**). This reduction of G₂/M phase arrest under the rescue regime reinforces the hypotheses that [c*is*-PST] is the main determining factor for the **PSTs'** biological effects in practical settings, and that in our experiments, [c*is*-PST] is determined by the applied dose of **PST** multiplied by a scaling factor for the PSS(λ). The similarity of the results in **Figures S3G-I-J** again indicates that the cytotoxicity of **cis-PST-1** is generalizable across cell lines of different origins.

C.4: Membrane permeability induced by PST-1

Membrane permeability assessment was performed as detailed in the **Materials and Methods**. Similarly to the results obtained in MDA-MB-231 cell line (**Figure 3A**), a light-dependent induction of membrane permeability was also shown in HeLa cells (**Figure S3A**) after 70 h treatment with **PST-1**. Under the toxic regime, dose-dependent increases in membrane permeability were evident, attaining a similar level to those seen with the parent compound **CA4**, but no toxicity of **PST-1** was observed in the dark.

C.5: Nuclear fragmentation (PST-1)

A quantification of nuclear fragmentation was performed as detailed in the **Materials and Methods**, on MDA-MB-231, Jurkat and HeLa cells treated with **PST-1** (**Figure 3B** and **Figure S3B-E**; note that the panels of **Figure S2C-D** present overlapping data sets). Conditions: MDA-MB-231 and Jurkat: toxic regime - 350 ms pulses every 5 min, treatment time 48 h; HeLa: toxic regime - 1 s pulses every 15 min, treatment time 30 h. In all cell lines tested, the toxic regime at 390 nm resulted in steep induction of nuclear fragmentation with submicromolar **PST-1**, showing an effect similar to the one induced by the parent compound **CA4**. In the dark regime, the **PST** response began only at 100 – 300 times higher concentration than under the toxic regime. Jurkat cells were most sensitive to **PST-1** (EC₅₀ of 80 nM under the toxic regime) however all cell lines gave qualitatively similar response. This again indicated that **PSTs** have a generalizable mode of cytotoxic action across different cell lines (as is appropriate to CDIs) and that their cytotoxic mechanism may be controlled by light.

C.6: IF staining of tubulin in fixed cells

Immunofluorescence tubulin staining was performed in MDA-MB-231 cells as described in the **Materials and Methods**. **Figure S4A** shows a representative image after **CA4P** treatment. **CA4P** led

to complete microtubule breakdown and fragmentation of the nuclei (typical for apoptotic cells). This is a positive control to the **PST-1** immunofluorescence studies shown in **Figure 4C**.

Part D: *C. elegans* experiments

Still images of *C. elegans* embryos bathed in 40 μM **PST-1** and exposed to single-cell-localised ROI illumination with different conditions as outlined in the **Methods**, are shown in **Figure 6A-B**. The videos from which **Figures 6A** and **6B** are drawn are available as **Movie S4** and **Movie S5** respectively. The experiments show that single cells within *C. elegans* embryos can be targeted for mitotic arrest by localised illumination with 405 nm light (bulk isomerisation to the *cis* form within the defined ROI; representative results from $n=8$ independent experiments are shown). Rescue protocol experiments such as **Movie S5** show that by adding a second pulse component at 514 nm after each pulse of 405 nm, there is no mitotic block (bulk of **PST-1** is kept as *trans* isomer, since although each 405 nm pulse component favours *cis*, the immediately subsequent 514 nm component then induces bulk photodeactivation to *trans*); while an internal positive control within the experiment (cell with 405 nm pulse component only) was arrested in mitosis ($n=2$). In all cases, the neighbouring cells outside the ROIs, including those with cell cycle synchronised to the selected cells, divided normally.

Figure S4B-E shows representative images from control experiments examining the potential effects of illumination parameters on the mitotic progression, as well as behaviour of **PST-1** in the absence of photoisomerising illumination. These accompany the *C. elegans* experiments shown in **Movies S4-S5** discussed above. **Figure S4B** shows a dark control with **PST-1**: the cell cycle progression is not altered by **PST-1** at 40 μM in the absence of activating irradiation, even in the long term. **PST-1** was applied at $t=0$ min and embryos were imaged for up to 150 min. No perturbation of embryonic development was observed as many cell divisions occurred successfully ($n=6$). **Figure S4C-D** shows illumination controls in the absence of **PST-1**: the single-wavelength (405 nm only) and dual-wavelength (405 followed by 514 nm) irradiation regimes do not affect cell cycle progression in the absence of **PST-1** (C: $n=4$; D: $n=2$). **Figure S4E** shows a further control for the rescue regime: **PST-1** does not give mitotic arrest when irradiated at 514 nm only ($n=4$). Taken together, these results show that generating mostly *trans*-**PST-1** allows mitosis to proceed, while generating significant *cis*-**PST-1** arrests it; and *cis* \rightarrow *trans* photoswitching efficiently allows cells to continue mitosis after exposure to concentrations of the *cis* isomer that would otherwise leave them arrested.

Lastly, positive controls using the archetypal CDI, colchicine itself, were performed (**Figure S4F-G**) Note that the *C. elegans* strain (expressing GFP-tagged tubulin and histones) used here allows for direct visualisation of mitotic spindle and chromosome position. When colchicine was applied, chromosomal segregation was stopped and the microtubules depolymerized, whether colchicine was applied during metaphase or anaphase (**Figure S4F** and **G** respectively). The observed effect exactly

mirrors the arrest of chromosomal segregation seen with **PST-1** under 405 nm illumination and confirms that *cis-PSTs* behave as expected for a CDI in this model system.

Considering the combined data from these experiments, we can rule out that **PST-1**'s effect on mitosis is due to phototoxicity or a photosensitised mode of specific biochemical damage (eg. the chromophore-assisted laser inactivation effect), since then the Rescue cells *e.g.* in **Figure 4B** and **Movie S5** would also experience these effects, instead of dividing normally. We thus conclude that **PST-1** is inactive as an antimitotic in the dark, can be efficiently photoactivated by short 405 nm pulses, and can then be reversibly photodeactivated by short 514 nm pulses (up to 20 activation/deactivation cycles shown in **Movie S5**). Thereby, **PST-1** enables full and reversible photocontrol of mitosis on a single-cell level within the living organism, without affecting the progression of mitosis in neighbouring cells, and presenting no “background activity” in the absence of targeted illumination.

Part E: Mouse cremaster muscle experiment

Mouse cremaster muscle was treated with 50 μ M **PST-1P** (or PBS only) under 390 nm or in the dark. Following the treatment, muscle was fixed, stained and imaged as outlined in the **Materials and Methods**. **Figure S5A-D** gives larger-scale and wider field of view images of the data that are shown in **Figure 6C**. **PST-1P** achieved clear disruption of MTs *in vivo* under 390 nm irradiation; but in the dark it had no effects on the microtubule cytoskeleton that could be distinguished from the PBS negative controls.

Appendix 1: Photoisomerisation parameter space

Rationale for the quantities to be measured by *in vitro* studies:

We aimed to evaluate those isomerisation parameters of the **PSTs** which would be needed to satisfactorily design **PST** biological assays, and to evaluate and intercompare the results. Key measurements were therefore to be taken at 37 °C in aqueous solution (cell culture purpose PBS at pH~7.4, with 10% acetonitrile for solubility). We focussed on deriving *qualitatively useful* estimates of three key parameters: (1) **PSS(λ)**, the fraction of *cis* isomer established at the photostationary state (the condition when *trans*↔*cis* photoisomerisations are in equilibrium under saturating photon flux) as a function of wavelength. PSS(λ) depends strongly on the relative ratio between $\varepsilon_E(\lambda)$ and $\varepsilon_Z(\lambda)$ (the absorption coefficients of the *trans* and *cis* forms at wavelength λ), among other factors; (2) the **relative efficiency E(λ)** of approaching the PSS(λ) as a function of that wavelength λ . E(λ) reflects the magnitude of the photon flux one would need to apply to photoisomerise a mixture of *trans* and *cis* forms from a starting *cis/trans* ratio by a given percentage towards the *cis/trans* ratio at PSS(λ). E(λ) depends strongly on the absolute magnitudes of both $\varepsilon_E(\lambda)$ and $\varepsilon_Z(\lambda)$, among other factors; (3) the **thermal reversion halflife τ** for the spontaneous Z→E isomerisation.

PSS(λ), E(λ) and τ should inform the design of appropriate lighting conditions for long-term biological experiments, since for these, samples should not be irradiated at high intensities or with high net flux (Boonacker and Van Noorden, 2001; Grossweiner, 2005; Ibsen et al., 2013). If irradiation is to be applied at a fixed intensity as a function of wavelength [I(λ)], then limiting the applied flux while favouring the maintenance of the PSS is most easily achieved by applying pulses of time length t_{IR} , with the interval t_{pause} between pulses chosen to be rather less than τ; $1/[I(\lambda) \times E(\lambda)]$ could be used as a factor to scale the relative pulse durations $t_{IR}(\lambda)$ so that the PSS(λ) is approached equally at each wavelength applied (for *in cellulo* studies, $\varepsilon(\lambda) \times c \times l$ is relatively small so we ignore absorbance along the optical path).

These parameters also enable a key analysis and comparison of assay data. If the PSS is essentially maintained by appropriate lighting conditions with $t_{pause} \ll \tau$, then $[Z]^*(\lambda)$ – the product of the total applied concentration of **PST**, and its PSS(λ) – approximates the time-average concentration of *cis-PST* in the assay. The local net antitubulin effect generated might then be understood simplistically as the product of $[Z]^*(\lambda)$ with a wavelength-independent Inhibitory Factor which would crudely describe the *cis-PST*'s strength of tubulin polymerisation inhibition (which for **PSTs** should reflect not only the *cis* isomer's kinetic parameters of binding/unbinding and thermodynamic binding strength, but also eg. kinetic parameters of Z→E relaxation in the active site, and of the *trans* isomer's unbinding kinetics). This crude model was rather extraordinarily successful even when applied to far-downstream readout given in the long term, by cytotoxicity results obtained in the complex *in cellulo* environment (see **Figure S1C**). Therefore we concluded that under our assay conditions, PSS(λ) was reliably established, and we could indeed intercompare the **PSTs**' inhibitory strengths.

Note however, that the *quantitative* predictive power obtainable by using any particular set of *in vitro*-determined, solution-state values of τ , PSS(λ), and E(λ) was not considered to be strong, since there are large uncertainties about the true intracellular concentration, location, and expected isomerisation behaviour of an applied **PST**. Strong bioconcentration of the lipophilic combretastatins inside cells (relative to the applied extracellular concentration), and their inhomogeneous repartition between different cellular compartments, have been reported (Bisby et al., 2012). The **PSTs** too were predicted (calculated cLogP ~3-5) and observed (long retention times on reverse phase LCMS) to be relatively lipophilic; and similar bioconcentration of the **PSTs** would reduce the accuracy of using the applied dose to model the true [Z]*. Furthermore, azobenzenes have strong environment-dependence of τ , and to a lesser extent also of PSS(λ) and E(λ); and even in fully aqueous media τ depends strongly on the pH especially below pH 5-6 (Knoll, 2003). Therefore **PSTs** located in different cell types, in different cell compartments (eg cytosol vs. lipid membranes), or even lipophilically adsorbed onto carrier proteins (Bisby et al., 2012), would experience a range of solvent environments and pH values which should locally alter these three isomerisation parameters far from any single set of *in vitro*-determined values, providing a spatiotemporally heterogeneous distribution of stocks and sinks of the active *cis* form. Even the model that a certain effective pool of *cis*-**PST** at concentration [Z]*(λ) establishes a binding equilibrium with tubulin, where the proportion of bound tubulin then determines the “downstream biological readout,” is also a simplification, due to the potential for bound-state relaxation. If the *cis*→*trans* relaxation rate of bound **PSTs** is significantly different from the bulk rate, then considering only solution-state τ will be insufficient to understand the **PSTs’** bioactivity. Bound-state relaxation may also arise by photoisomerisation since the PSS(λ) is a dynamic equilibrium state. The effect these may have on overall MT inhibition is difficult to predict (especially at rather low **PST** concentrations only slightly beyond the threshold for bioactivity, which would be most interesting for biological applications). However, both could be very important, as the on-off kinetics and lability of CDIs have been argued to play a vital role in determining their biological consequences in diverse systems and assays (Jordan, 2002). Indeed from ongoing studies it seems likely that an altered- τ effect may contribute to the unexpectedly weaker toxicity of *cis*-**PSTs** compared to **CA4**.

With so many unknowns, we considered a full analytical description of **PSTs’** light-dependent bioactivity impossible. So, for initial qualitative intercomparison of the **PSTs** we simply determined estimates for solution-state PSS(λ), E(λ) and τ under *reasonable* conditions, by measurements which could simply be precise *enough* to be intercomparable between compounds. Our tests for whether these estimates, along with our simplistic model of Z*(λ), were *good enough* to inform an initial choice of biological assay conditions which could later be optimised, were the wavelength- and pulse timing-dependency assays shown in **Figure S1C** and **Figure S2O**. The successful outcome and logically consistent analysis of these assays under our simple model, argued that for our assay purposes, the prediction of the **PSTs’** wavelength-, pulse protocol-, and concentration-dependent effects required no more detailed investigations than this.

Defining and determining $\varepsilon_E(\lambda)$ and $\varepsilon_Z(\lambda)$, PSS(λ), τ , and $E(\lambda)$:

Measuring $\varepsilon_E(\lambda)$ and $\varepsilon_Z(\lambda)$: UV-Vis absorption spectra $A_{\text{dark}}(\lambda)$ in the range $340 \text{ nm} < \lambda_{\text{meas}} < 540 \text{ nm}$ were acquired, with samples kept in the dark overnight, so it was assumed that no significant spectral contribution from the *cis* isomer was present in these spectra. Then, an isosbestic point (wavelength λ_{iso}) was found for each compound by monochromator irradiation. See Part B for details.

HPLC (high-performance liquid chromatography) was then used with the run conditions described in Part A to measure $\varepsilon^*_E(\lambda)$ and $\varepsilon^*_Z(\lambda)$ (the separated absorption profiles of *trans* and *cis* isomers respectively, in arbitrary units which are not intercomparable in an absolute sense). Although these spectra are acquired in less well-defined and less biologically appropriate medium (usually 50:50 to 90:10 acetonitrile:slightly acidified MilliQ water (depending on the elution time) and 25 °C), it was approximated that these spectra would be identical in shape if measured under the UV-Vis conditions. To place the arbitrary-unit absorption spectra on an absolute scale, the maximal absorption wavelength λ_{strong} of the *trans*-isomer was first selected from the UV-Vis measurement: typically, $\lambda_{\text{strong}} \approx 380 \text{ nm}$. Expressing $A_{\text{dark}}(\lambda)$ in units $M^{-1}cm^{-1}$, $\varepsilon^*_E(\lambda_{\text{strong}})$ was then scaled so that $\varepsilon_E(\lambda_{\text{strong}}) = A_{\text{dark}}(\lambda_{\text{strong}})$, giving:

$$\underline{\varepsilon_E(\lambda)} = \varepsilon^*_E(\lambda) \times [A_{\text{dark}}(\lambda_{\text{strong}})/\varepsilon^*_E(\lambda_{\text{strong}})] \quad (\text{Eq. 1})$$

and the isosbestic point was used to scale the *cis*-isomer spectrum as per:

$$\underline{\varepsilon_Z(\lambda)} = \varepsilon^*_Z(\lambda) \times [\varepsilon_E(\lambda_{\text{iso}})/\varepsilon^*_Z(\lambda_{\text{iso}})] \quad (\text{Eq. 2})$$

The measured value of $A(\lambda_{\text{iso}})$ could also have been used to scale the spectra, with the advantage that finding $A(\lambda_{\text{iso}})$ does not require samples to be kept in the dark prior to UV-Vis measurement. However, using $A_{\text{dark}}(\lambda_{\text{strong}})$ was preferred, since (1) $A(\lambda_{\text{iso}})$ was typically much smaller than $A_{\text{dark}}(\lambda_{\text{strong}})$; (2) the gradient around $A(\lambda_{\text{iso}})$ is much larger than around $A_{\text{dark}}(\lambda_{\text{strong}})$; (3) λ_{iso} was seen to depend more on the solvent than λ_{strong} ; these three factors give the result that the standard deviation in the scaled absorptivities which the λ_{strong} method generated was smaller.

Calculating PSS(λ): In a simple analysis of the PSS(λ), it was approximated that Φ_{EZ} and Φ_{ZE} [the quantum efficiencies of the photoisomerisations *trans*→*cis* and *cis*→*trans*, respectively] are equal and independent of wavelength, and also that the kinetics of spontaneous reversion could be ignored (i.e. in the target experimental conditions, photoisomerisation is the strongly dominant bulk isomerisation pathway, comparing to thermal relaxation). A function $\phi(\lambda)$ was then calculated as per:

$$\underline{\phi(\lambda)} = \varepsilon_E(\lambda)/[\varepsilon_Z(\lambda) + \varepsilon_E(\lambda)] \quad (\text{Eq. 3})$$

If Φ_{EZ} and Φ_{ZE} are equal and independent of wavelength, $\phi(\lambda)$ gives the true PSS(λ). The wavelength independence of Φ_{EZ} and Φ_{ZE} may be an acceptable approximation in regions of relatively strong absorption within the visible spectrum. Their equality may also be an acceptable assumption: since if Φ_{EZ} and Φ_{ZE} are unequal but only depend weakly on wavelength in regions of relatively

strong absorption, then $\phi(\lambda)$ is a transform of the true PSS(λ), and this transform preserves the features of PSS(λ) which were most desired for evaluation in this study as long as Φ_{EZ} and Φ_{ZE} are not too different (eg less than a factor of ten difference). Indeed, the calculated $\phi(\lambda)$ were later confirmed by *in cellulo* experiments to give reliable indications of both favourable wavelengths for bulk *trans*→*cis* and bulk *cis*→*trans* photoisomerisation, and of the experimentally-experienced PSS(λ) (see **Figure S1C**). The advantages of calculating $\phi(\lambda)$ rather than exhaustively measuring the PSS(λ) experimentally are that (a) the throughput is much faster, (b) the true PSS(λ) may be difficult to achieve at weakly-absorbing/inefficiently-isomerising wavelengths or with fast-relaxing compounds, (c) the true PSS(λ) may be difficult to measure accurately at wavelengths where one isomer strongly dominates the sample even if both are relatively strongly absorbing, and (d) the variation of PSS(λ) with changes in the local biological microenvironment (polarity, pH etc.) may anyway be larger than the error incurred by the assumption $\phi(\lambda)=\text{PSS}(\lambda)$.

Calculating E(λ): To consider the efficiency E(λ) of approaching the PSS(λ) under flux-limited conditions [where a relatively low light intensity is applied, so that the sample does not instantaneously attain PSS(λ)], in a simple analysis we again approximated that Φ_{EZ} and Φ_{ZE} are equal and independent of wavelength. Then, ignoring spontaneous reversion, we derive Z(t) [the proportion of a sample present as the Z form after irradiation at a given wavelength ‘for time t’ - where t is a dummy parameter reflecting normalised photon flux] as follows:

$$dZ(t)/dt = E(t)\varepsilon_E(\lambda) - Z(t)\varepsilon_Z(\lambda) \quad (\text{Eq. 4})$$

Defining the sum of the absorptivities $\sigma(\lambda) = [\varepsilon_E(\lambda)+\varepsilon_Z(\lambda)]$, we then have

$$Z(t) = Z(t_0)\exp[-\sigma(\lambda)t] + \varepsilon_E(1-\exp[-\sigma(\lambda)t])/\sigma(\lambda) \quad (\text{Eq. 5})$$

Note in passing that maximising or minimising (Eq. 4) implies that *under flux-limited conditions, the optimum wavelength for effecting photoisomerisation in either direction (Z→E or E→Z) is not a constant, but depends on the current Z:E isomeric ratio*. Typically, for E→Z isomerisation, the optimum wavelength varied by only 10-20 nm for $0 < Z(t_0) < 0.9$; however, for the “rescue” wavelength used to effect Z→E isomerisation, for a typical compound the variation could be substantial (>100 nm) even over the range $0.2 < E(t_0) < 0.8$. This makes quoting an “optimum rescue wavelength” a gross simplification, which sometimes missed key qualities.

To compare efficiencies of approaching the PSS as a function of wavelength, note that the “rate constant” for this photoisomerisation process is $\sigma(\lambda)$ (see Eq. 5). Thus a relative photoisomerisation efficiency E(λ) was calculated as per Eq. 6, and is graphed in **Figure S1A**:

$$E(\lambda) = \sigma(\lambda)/[\sigma(390)] \quad (\text{Eq. 6})$$

Larger values of E(λ) therefore denote higher efficiency photoisomerisation [less photon flux is required to approach the PSS(λ)], where E(λ) is parametrised to $\sigma(390)$ since typically 390 nm gave

strong absorption and efficient photoisomerisation, ie. satisfactorily rapid attainment of a *cis*-rich PSS useful for biological studies (see **Figure S2**). It should be noted that $E(\lambda)$ are *not* intercomparable between compounds, especially as the Φ_{EZ} (or the Φ_{ZE}) of two arbitrarily chosen compounds may differ by a significant amount, even if the approximation that Φ_{EZ} and Φ_{ZE} are equal and independent of wavelength applies independently to each compound. Thus while $E(\lambda)$ does not present new measured information, as an efficiency measurement it is a convenient quantity, whereby increasing $E(\lambda)$ denotes higher efficiency isomerisation (lower dose of light required to approach the PSS(λ)).

Trends in τ : Finally, trends in τ were ascertained by establishing the PSS at λ_{strong} , then turning off the light source at time t_0 , and measuring $A(\lambda_{\text{strong}})$ over time. Data were acquired for half an hour, or else the first three halflives (whichever was the shorter period), then fitted to:

$$A(\lambda_{\text{strong}}, t) = A_{\text{dark}}(\lambda_{\text{strong}}) - [A_{\text{dark}}(\lambda_{\text{strong}}) - A(\lambda_{\text{strong}}, t_0)] \times e^{-kt} \quad (\text{Eq. 7})$$

This fit was used to return an *in vitro* halflife τ^* for the *cis*→*trans* spontaneous thermal reversion isomerisation process, defined as $\tau^* = \ln(2)/k$ (**Figure S1B**). It should be recalled however, that azoaryl compounds' thermal reversion rates are known to depend strongly upon their microenvironment, such as pH and solvent/solvation effects (Beharry and Woolley, 2011b; Knoll, 2003). This was shown for **PST-1**, where a change of only 1.4 pH units – while remaining within an aqueous environment – gave a 25% change in τ^* . Note too that different compounds are expected to respond very differently to changes in pH and environment so no unifying trends are expected. Therefore the τ^* acquired *in vitro* were considered appropriate only for qualitative intercomparison between samples (trend of τ^* vs structure), rather than quantitative prediction of the τ values which might be experienced *in cellulo* or *in vivo*.

A note on photoisomerisations at wavelengths above 530 nm

Driving photoisomerisation in a sample depends not only on the intensity applied but on intrinsic switching efficiency at the wavelength applied. The measurement procedures used above rely on low-intensity light, so can demonstrate photoswitching only at wavelengths with relatively high $E(\lambda)$, eg. below 530 nm, where the applied monochromator light dominates the effects of both the 378 nm readout beam of the spectrophotometer and of the spontaneous *cis*→*trans* isomerisation. However if light at >530 nm is applied at sufficient intensity, near-complete (>90%) *cis*→*trans* photoisomerisation may still be actively induced. So, (1) if choosing a wavelength for a rescue protocol where weaker light sources must be used (such as the long-term LED lighting systems), shorter wavelengths such as 505-515 nm, which generate “worse” *cis/trans* ratios, may prove more effective; but (2) it is likely that longer wavelengths can compensate for their small $E(\lambda)$ to deliver near-complete *cis*→*trans* isomerisation, if very high intensities, eg. a microscopy laser, can be used.

Appendix 2: PhotoCan “Disco” cell culture lighting system

Disco system – in practice

Figure S6 introduced our “Disco” cell culture lighting system, which we describe in more detail to encourage other researchers to use such simple and cost-effective automatic, multichromatic, parallelised pulsed lighting systems.

Disco system – Switchboards

Note: since this work was performed, we have found that pre-prepared 8-Relay modules with identical circuit design and function as ours, with the correct operating voltages/currents for use with Arduino input, and output circuits up to 10A at 24V DC, and with inbuilt operation indicator LEDs, are now available for 10-20€ by mail order from quality electronics suppliers such as Okaphone Elektronika (www.okaphone.nl) as well as from large internet warehouses (searchterms “5V Relay Module Arduino”). We confirmed that the pre-built switchboard from Okaphone was suitable.

We built switchboards to use programmable timed output sequences from a cheap, simple Arduino microcomputer to drive sets of LED-arrays to flash ON/off with identical timings. The Arduino timed voltage sequences alternate between 5V [but low current] and 0V, and independent output can be taken from up to 52 “pins” on a standard Arduino (50€). Each LED-array required 24V, 80-320 mA power. Typically, up to 8 arrays were run on an identical timing sequence controlled by the output from one pin and up to 8 pins were used in one parallelised experiment, so upwards of 30 LED arrays were run independently or in parallel in a single experiment. The circuit diagram in **Figure S6A** depicts one such switchboard arrangement.

In brief, the switchboards took the 5 V output from an active pin on the Arduino, through a 1000-Ohm resistor, to actuate a transistor allowing a 5 V driving current (primary circuit) to close the switch of a Reed Relay (with a diode as protection for the against back-flow current during state change). This switch bridged the gap between a set of LED arrays (with each array in the set being in parallel) and a 24V external power supply. Thus the arrays turned off and on according to the timed Arduino sequence of that pin. By setting up multiple relay circuits (eg. between 3 and 14) on one switchboard, and connecting each relay circuit to a different Arduino output pin, we could drive the different timing patterns for cell culture experiments in a fully parallel, automated fashion which was also highly modular (different wavelengths can be obtained by swapping LEDs on each array). **Figure S6E** shows working examples of these switchboards. The power source driving the switchboard+Arduino was a standard, low-current 5 V DC wall charger (eg. a re-purposed mobile phone charger); the power source for the arrays (24 V DC) could also be a low-current model (eg. 2 A is suitable for twenty 24-LED arrays flashing in unison, or many more with staggered timing).

In the switchboards shown in **Figure S6E**, the Arduino inputs (near bottom) are indicated by the lightning symbols. Outputs for the arrays are indicated by triangles (near top) and arrays are visible, plugged in, at top. The output leads are passed into a cell culture incubator during real operation, so the Arduino and switchboard do not need to be housed in the incubator (**Figure S6F**).

Disco system – LED arrays

LED arrays were constructed to illuminate well plates. While we used one array per well plate, multiple well plates could also be stacked on top of a single array without significant difference in the results obtained, due to the relatively high LED wattage/area ratio of the directional LEDs used (usually 15° cone angle and 10-20 mW output), coupled with the transparency of our standard well plates at the tested wavelengths [plate absorbance <10% if $\lambda>340$ nm], careful geometric alignment of the stacks over the arrays (held in place by rubber corners), the low optical density of the solutions of azobenzenes at the tested concentrations, and the high azobenzene photoswitching efficiency. We trialled both 96-LED and 24-LED arrays and found similar performance with azo switches, though the 24-arrays were cheaper and easier to build and run. No machining/laser cutting is required, just solder and glue. Each 24-array required the following parts and consumables:

Standard 24-array		
Parts	#	€ (total)
160x100 mm pre-punched circuit board card (Eurocard, 2.54 mm spacing)	1	3
small 47 ohm <u>resistor</u> (rated to 0.05W)	4	0.25
standard, breakable SIP IC connector rows, for inserting LEDs (40 slots/row, breakable, 2.54 mm spacing)	3	6
2-slot screw-in <u>socket</u> , 5.08 mm spaced legs	1	0.5
30 mm lengths of standard red rubber vacuum <u>tube</u> (as supports to hold plate)	4	0.25
3-5 mm high stick-on rubber <u>feet</u> (or flat-cut pieces of rubber tube) (non-slip grip, shields circuits from contacting surface below)	4	1
Consumables per array		
zinc-coated 0.5 mm Cu <u>wire</u> (for connections; 40 cm)		0.1
<u>solder</u> (20 cm)		0.2
two-component <u>epoxy</u> resin for gluing tubes		0.5
<u>superglue</u> for gluing stecker sections		0.2
Array total cost over the counter		
LEDs		
<u>24 LEDs</u> (5 mm size, legs 2.54 mm apart, 20 mA / 4V) eg RLS-UV400, $\lambda=400$ nm (Roithner Lasertechnik)		10€

Construction: Cut the LED legs down to size, keeping the polarity (eg. long leg & short leg). Split the SIP rows into sections of four slots each (easier to glue in place). Centred on the board, align the sections in rows of 6, each row 94 mm long with equal horizontal spacing between the sections, with approx. 18 mm vertical spacing between rows. On a pre-punched 2.54 mm board, vertical spaces will

be 18/21/18 mm, and horizontal spaces (to section centres) will be 18 / 21 / 18 / 18 / 21 mm, for best alignment with wells in a standard plate (**Figure S6C**). Glue the sections in place. Align the socket with the top row, at the edge of the plate, and glue in place. Flip the board over; solder cut pieces of wire to connect the sockets in each row leaving gaps (for the LEDs) between the middle two slots, and inserting one resistor per row. Connect the four rows (in parallel) to the positive and negative poles of the socket. Place/glue the feet as close to the outermost sections as possible (**Figure S6D**), so that they will sit on the lid of a cell culture plate below them for stacking plates if needed, or at least provide clearance between wiring and the surface below in case of shorts in damp incubator settings (the bottom of the array can also be sprayed with lacquer to insulate it). Flip the board over, epoxy the rubber tube sections in position so that the corners of a standard cell culture plate lie in the centre of each tube section when its wells are aligned over the LEDs. Using a sharp sturdy craft knife, carefully cut out inward-facing 90° wedges approx. 5 mm high from the tubes, so that the cell culture plate will slide down into these slots and be held firmly in place during movement, so will not be de-aligned by small impacts, and so it sits flat (**Figure S6C**).

These 24-arrays can accommodate 96-, 24-, and 6-well cell culture plates with no significant spatial variation in the biological effects of the photoswitches tested here under our conditions, probably due to light scattering in the clear cell culture well plates combined with the efficiency of azobenzene photoisomerisation; and other formats such as 130×87 mm cell culture dishes can also be fit by installing extra tubes as holders. Alternatively, similar construction gives 96-LED arrays if desired; the slightly irregular gaps shown on the schematic permits using stecker rows without cutting them into sections (**Figure S6B**).

Disco system – Arduino program 1

The free and open-source Arduino GUI interface (<http://www.arduino.cc>) allows uploading programs to the Arduino via USB cable. Program 1 is a typical program we used to control standard cell culture experiments. It has a long but basic structure for easy overview. Typical pulsed protocol settings are given through pins 46-53, and mirrored output on pins 22-29 as well as overall indicator pins 12-13 for an optional indicator board showing system operation. Channel pairs (1 & 2) and (3 & 4) are synched for *strong rescue* protocols (channel 1 activating, channel 2 deactivating; similarly for 3&4). The standard cycle time is 30 seconds (except channels 5-6). By default, cycles are slightly staggered so as not to risk overloading the array power supply by flashing all arrays on simultaneously, when many arrays are used (though for relatively few LED boards this can be ignored entirely).

```
/* Non-Array Program 1: Channels 1/2 and 3/4 as synched pairs of Act/Deact ; channels 5-8 for
general purpose. Please acknowledge source-inspiration if you find this useful. OTS 2013 */

/* CIRCUITS - 8 channels of LED arrays hooked on Digital pins 46-53, INVERSE MIRRORS - 8
channels to Digital Pins 22-29 for indicator board */
const int pinC1 = 46; const int pinC2 = 47; const int pinC3 = 48; const int pinC4 = 49; const
int pinC5 = 50; const int pinC6 = 51; const int pinC7 = 52; const int pinC8 = 53;
```

```

/* INDICATORS : Operation pin 13 flashes on and off to show it's running (can plug a LED
straight in), Index pin 12 is ON if any circuit is lit. C pins are for signal output, M pins
are INVERSE of their C pin, can hook to indicators externally to see system run. Index shows
if any pin is on, Operation always blinks to show power is OK. */
const int pinM1 = 22; const int pinM2 = 23; const int pinM3 = 24; const int pinM4 = 25; const
int pinM5 = 26; const int pinM6 = 27; const int pinM7 = 28; const int pinM8 = 29;
const int pinCIndex = 12; const int pinOperation = 13;

/* INITIALISE : How long to flash LEDs on (milliseconds); int is less than 65556 ms == 65
seconds */
/* the synchronised pairs */
unsigned int tIRC1 = 150; unsigned int tIRC2 = 500;
unsigned int tIRC3 = 150; unsigned int tIRC4 = 500;
/* the individual channels */
unsigned int tIRC5 = 75; unsigned int tIRC6 = 300; unsigned int tIRC7 = 800; unsigned int
tIRC8 = 250; unsigned int tIRCOperation = 250;

/* INITIALISE How long in a CYCLE of off-ON (ms); used to ensure regularity and
synchronisation; long is less than 2,147,483,647 ms == 596 hours; 300,000 ms == 5 min */
unsigned long tCycC1 = 30000; unsigned long tCycC2 = tCycC1;
unsigned long tCycC3 = 30000; unsigned long tCycC4 = tCycC3;
unsigned long tCycC5 = 6000; unsigned long tCycC6 = 15000; unsigned long tCycC7 = 30000;
unsigned long tCycC8 = 30000; unsigned long tCycCOperation = 2000;

/* INITIALISE : timestamp - counters for offsetting irradiation cycling; ALLOW NEGATIVE */
long timestamp = 0;
/* the synchronised pairs */
long counterC1 = 0; long counterC2 = counterC1 + tIRC1 - tCycC2;
long counterC3 = 1000; long counterC4 = counterC3 + tIRC3 - tCycC4;
/* the individual channels */
long counterC5 = 2000; long counterC6 = counterC5 + tIRC5; long counterC7 = counterC6 +
tIRC6; long counterC8 = counterC7 + tCycC7; long counterCOperation = 0;

/* INITIALISE Circuit State Variables into state 1 */
int stateC1 = LOW; int stateC2 = LOW; int stateC3 = LOW; int stateC4 = LOW; int stateC5 =
LOW; int stateC6 = LOW; int stateC7 = LOW; int stateC8 = LOW;
int stateM1 = LOW; int stateM2 = LOW; int stateM3 = LOW; int stateM4 = LOW; int stateM5 =
LOW; int stateM6 = LOW; int stateM7 = LOW; int stateM8 = LOW;
int stateCOperation = HIGH; int stateCIndex = HIGH;

/* REDECLARE into state 1; use the cycle times to set the tPause: How long to pause between
flashes (ms); long is less than 2,147,483,647 ms == 596 hours; 300,000 ms == 5 min */
unsigned long tPC1 = tCycC1 - tIRC1; unsigned long tPC2 = tCycC2 - tIRC2; unsigned long tPC3
= tCycC3 - tIRC3; unsigned long tPC4 = tCycC4 - tIRC4; unsigned long tPC5 = tCycC5 - tIRC5;
unsigned long tPC6 = tCycC6 - tIRC6; unsigned long tPC7 = tCycC7 - tIRC7; unsigned long tPC8
= tCycC8 - tIRC8; unsigned long tPCOperation = tCycCOperation - tIRCOperation;

void setup() {
pinMode(pinC1, OUTPUT); pinMode(pinC2, OUTPUT); pinMode(pinC3, OUTPUT); pinMode(pinC4,
OUTPUT); pinMode(pinC5, OUTPUT); pinMode(pinC6, OUTPUT); pinMode(pinC7, OUTPUT);
pinMode(pinC8, OUTPUT); pinMode(pinCIndex, OUTPUT); /* set the Channel pins as output */
pinMode(pinM1, OUTPUT); pinMode(pinM2, OUTPUT); pinMode(pinM3, OUTPUT); pinMode(pinM4,
OUTPUT); pinMode(pinM5, OUTPUT); pinMode(pinM6, OUTPUT); pinMode(pinM7, OUTPUT);
pinMode(pinM8, OUTPUT); pinMode(pinCOperation, OUTPUT); } /* set the mirror pins as output */

void loop()
{
timestamp = millis();

/* Process Circuit 1 */
if (timestamp < counterC1 + tIRC1) {stateC1 = HIGH; stateM1 = LOW;} /* still keep it on */
else if (tIRC1 > 10 && timestamp > counterC1 + tIRC1 + tPC1) {counterC1 = timestamp; stateC1
= HIGH; stateM1 = LOW;} /* immediately cycle over the counter1 and turn on LED */
else {stateC1 = LOW; stateM1 = HIGH;} /* else keep the circuit 1 state low. Now set Circuit
1 */
digitalWrite(pinC1, stateC1); digitalWrite(pinM1, stateM1);

/* Process Circuit 2 */
if (timestamp < counterC2 + tIRC2) {stateC2 = HIGH; stateM2 = LOW;} /* still keep it on */
else if (tIRC2 > 10 && timestamp > counterC2 + tIRC2 + tPC2) {counterC2 = timestamp; stateC2
= HIGH; stateM2 = LOW;} /* immediately cycle over the counter2 and turn on LED */
else {stateC2 = LOW; stateM2 = HIGH;} /* else keep the circuit 2 state low. Now set Circuit
2 */
digitalWrite(pinC2, stateC2); digitalWrite(pinM2, stateM2);

/* Process Circuit 3 */
if (timestamp < counterC3 + tIRC3) {stateC3 = HIGH; stateM3 = LOW;} /* still keep it on */
else if (tIRC3 > 10 && timestamp > counterC3 + tIRC3 + tPC3) {counterC3 = timestamp; stateC3
= HIGH; stateM3 = LOW;} /* immediately cycle over the counter3 and turn on LED */

```

```

else {stateC3 = LOW; stateM3 = HIGH;} /* else keep the circuit 3 state low. Now set Circuit
3 */
digitalWrite(pinC3, stateC3); digitalWrite(pinM3, stateM3);

/* Process Circuit 4 */
if (timestamp < counterC4 + tIRC4) {stateC4 = HIGH; stateM4 = LOW;} /* still keep it on */
else if (tIRC4 > 10 && timestamp > counterC4 + tIRC4 + tPC4) {counterC4 = timestamp; stateC4
= HIGH; stateM4 = LOW;} /* immediately cycle over the counter4 and turn on LED */
else {stateC4 = LOW; stateM4 = HIGH;} /* else keep the circuit 4 state low. Now set Circuit
4 */
digitalWrite(pinC4, stateC4); digitalWrite(pinM4, stateM4);

/* Process Circuit 5
if (timestamp < counterC5 + tIRC5) {stateC5 = HIGH; stateM5 = LOW;} /* still keep it on */
else if (tIRC5 > 10 && timestamp > counterC5 + tIRC5 + tPC5) {counterC5 = timestamp; stateC5
= HIGH; stateM5 = LOW;} /* immediately cycle over the counter5 and turn on LED */
else {stateC5 = LOW; stateM5 = HIGH;} /* else keep the circuit 5 state low. Now set Circuit
5 */
digitalWrite(pinC5, stateC5); digitalWrite(pinM5, stateM5);

/* Process Circuit 6 */
if (timestamp < counterC6 + tIRC6) {stateC6 = HIGH; stateM6 = LOW;} /* still keep it on */
else if (tIRC6 > 10 && timestamp > counterC6 + tIRC6 + tPC6) {counterC6 = timestamp; stateC6
= HIGH; stateM6 = LOW;} /* immediately cycle over the counter6 and turn on LED */
else {stateC6 = LOW; stateM6 = HIGH;} /* else keep the circuit 6 state low. Now set Circuit
6 */
digitalWrite(pinC6, stateC6); digitalWrite(pinM6, stateM6);

/* Process Circuit 7 */
if (timestamp < counterC7 + tIRC7) {stateC7 = HIGH; stateM7 = LOW;} /* still keep it on */
else if (tIRC7 > 10 && timestamp > counterC7 + tIRC7 + tPC7) {counterC7 = timestamp; stateC7
= HIGH; stateM7 = LOW;} /* immediately cycle over the counter7 and turn on LED */
else {stateC7 = LOW; stateM7 = HIGH;} /* else keep the circuit 7 state low. Now set Circuit
7 */
digitalWrite(pinC7, stateC7); digitalWrite(pinM7, stateM7);

/* Process Circuit 8 */
if (timestamp < counterC8 + tIRC8) {stateC8 = HIGH; stateM8 = LOW;} /* still keep it on */
else if (tIRC8 > 10 && timestamp > counterC8 + tIRC8 + tPC8) {counterC8 = timestamp; stateC8
= HIGH; stateM8 = LOW;} /* immediately cycle over the counter8 and turn on LED */
else {stateC8 = LOW; stateM8 = HIGH;} /* else keep the circuit 8 state low. Now set Circuit
8 */
digitalWrite(pinC8, stateC8); digitalWrite(pinM8, stateM8);

/* Process Circuit Index */
if (stateC1 == LOW && stateC2 == LOW && stateC3 == LOW && stateC4 == LOW && stateC5 == LOW
&& stateC6 == LOW && stateC7 == LOW && stateC8 == LOW) {stateCIndex = LOW;} /* don't shine if
all are off */
else {stateCIndex = HIGH;} /* indicates at least one circuit is active; danger burnout of
this LED! */

/* Process Circuit Operation */
if (timestamp < counterCOperation + tIRCOperation) {stateCOperation = HIGH;} /* still keep
it on */
else if (tIRCOperation > 10 && timestamp > counterCOperation + tIRCOperation + tPCOperation)
{counterCOperation = timestamp; stateCOperation = HIGH;} /* immediately cycle over the
counterOperation and turn on LED */
else {stateCOperation = LOW;} /* else keep the circuit Operation state low. Now set Circuit
Operation */
digitalWrite(pinCOperation, stateCOperation);
/* IT'S ALLOVER */
}

```

Disco system – Arduino program 2

The purpose of Program 2 is similar to that of Program 1, but (a) Program 2 uses matrices to shorten the structure while increasing the number of pins active; and (b) an optional “priming sequence” allows using several long irradiations at the start to attain PSS in standard experiments quickly, before reverting to the main sequence of timed and synchronised pulses intended to maintain them.

```

/* Array Program 2: Setup all pins 22-39 for individual wiring, and then pins 40-45 for
subsidiary block and 46-53 as usual for the main 8-channel block with serial cable. Assume
may use Wire, Subsid, AND Main blocks simultaneously or in combo.
Please acknowledge source-inspiration if you find this useful. OTS 20140730 */

unsigned long EscapeTime = 3000; /* ESCAPE TIME - time delay before program will start, after
plugging in Arduino: note all times are in milliseconds */

/* PRIMING SEQUENCE VARIABLES */
unsigned int PrimeCycles = 4; /* To kill the priming sequence, just set this to zero. Number
of priming flashes per channel */
unsigned long PrimingTiming[2] = {500, 10000}; /* PRIMING pulse duration is [0], the minimum
cycle time for one channel is [1] so as not to overheat those cells (will be updated as
needed automatically to match prime sequence) */

/* MAIN SEQUENCE VARIABLES*/
unsigned int NumberOfPins = 32; /* if change this, must add/remove lines in Pincode, and
change array index in Pincode, PinState, and Pausetimes */
unsigned long Pincode[32][4] = { /* rows of PIN_NUMBER_L, tIR, tCYC, delay_counter */
/* Pin numbers (Pincode[i][0]) are followed by an L for emphasis */
/* tIR (Pincode[i][1]) is irradiation time : note all times are in milliseconds */
/* tCYC (Pincode[i][2]) is the time between irradiation cycles */
/* delay_counter (Pincode[i][3]) is used for synchronising channels to avoid current overload
(usually doesn't need changes) and ALSO to allow rescue (ALWAYS needs a check!) */
{22L, 75, 5000, 0}, /* WIRE BLOCK starts here (anticipate limited current, stagger to
minimise draw). First TOX; this synchs to 32resc */
{23L, 75, 15000, 500}, /* this synchs long to 33resc; can synch to 46ShortResc; can
precompete to 50 */
{24L, 75, 15000, 1000}, /* preceded synch by 51LongResc; can synch to 48ShortResc */
{25L, 75, 15000, 1500}, /* can synch to 40ShortResc */
{26L, 75, 30000, 2000}, /* this synchs long to 34resc */
{27L, 75, 30000, 2500}, /* most common timing, make extra channel; can synch to 41ShortResc
*/
{28L, 75, 60000, 3000}, /* this synchs to 35resc or 42ShortResc */
{29L, 75, 120000, 3500}, /* this synchs to 36resc or 43ShortResc */
{30L, 75, 300000, 4000}, /* this synchs to 37resc or 44ShortResc */
{31L, 75, 600000, 4500}, /* this synchs to 38resc or 45ShortResc */
{32L, 375, 5000, 75}, /* Now RESCUES: this one is rescue to 22tox */
{33L, 375, 15000, 575}, /* rescue to 23tox or overrescue 46tox */
{34L, 375, 30000, 2075}, /* rescue to 26tox */
{35L, 375, 60000, 3075}, /* rescue to 28tox */
{36L, 375, 120000, 3575}, /* rescue to 29tox */
{37L, 375, 300000, 4075}, /* rescue to 30tox */
{38L, 375, 600000, 4575}, /* rescue to 31tox */
{39L, 1000, 1000, 0}, /* Constant ON; can use for bulk deactivation priming from ambient
*/
{40L, 75, 15000, 1075}, /* SUB BLOCK (interleave as WIRE's rescue, and as MAIN's
competTox): can use as supplementary tox, or "Short" Rescue for competitive
illuminations/secondary rescue time; this can synch to 24tox */
{41L, 75, 30000, 2075}, /*this can synch to 26tox */
{42L, 75, 60000, 3075}, /*this can synch to 28tox */
{43L, 75, 120000, 3575}, /*this can synch to 29tox */
{44L, 75, 300000, 4075}, /*this can synch to 30tox */
{45L, 75, 600000, 4575}, /*this can synch to 31tox */
{46L, 75, 15000, 575}, /* MAIN BLOCK (do not fear current overload here, can overlap to tie
together): alternately paired 75+375 for rescues; this has 47resc or can be shortrescue to 23
or undertox to 33 */
{47L, 375, 15000, 650}, /* Rescue for 46 */
{48L, 75, 15000, 1075}, /* this has 49resc or can be shortrescue to 24 */
{49L, 375, 15000, 1150}, /* Rescue for 48 */
{50L, 75, 15000, 550}, /* this has 51resc or can postcompete to 23 or precompete to 33 */
{51L, 375, 15000, 625}, /* Rescue for 50, prerescue to 52 */
{52L, 75, 15000, 1000}, /* this is posttox to 51 */
{53L, 1000, 1000} /* Constant ON; can use for bulk deactivation priming from ambient
*/};

/* INITIALISE Circuit States and Pause Time. Change index sizes HERE if needed. */
unsigned long PauseTimes[32]; /* pauses between flashes for each pin, main sequence */
int PinState[32]; /* state array used for all pins */
unsigned long PrimerCounter; /* timecounter for cycling the priming sequence: Last timestamp
a priming sequence was begun */
int PrimeCycComplete = 0; /*passflag, always initialise to zero */
unsigned long timestamp = 0; int j = 0; int m = 0; /* initialise these counters to zero */

void setup() {

    PrimerCounter = EscapeTime; /* SetupPrimingSeq: initialise to set the bar here */
}

```

```

    if(PrimeCycles < 1 ) {PrimeCycComplete = 1;} /* if no priming was desired, then annull the
priming sequence, otherwise proceed to initialise priming variables*/
    else if(PrimingTiming[1] < (NumberOfPins) * PrimingTiming[0]) {PrimingTiming[1] =
(NumberOfPins) * PrimingTiming[0];} /* check and overwrite the priming sequence overall cycle
time if needed so no two priming flashes overlap */

    for (int i = 0; i < NumberOfPins; i = i + 1) { /*Setup Main Sequence*/
        pinMode(Pincode[i][0], OUTPUT); /* activate output on that pin */
        PinState[i]=LOW; digitalWrite(Pincode[i][0], PinState[i]); /* initialise ALL pins "OFF"
*/
    }
    PauseTimes[i] = Pincode[i][2] - Pincode[i][1]; /* dial in the pause times */
    Pincode[i][3] = Pincode[i][3] + EscapeTime + PrimeCycles * PrimingTiming[1]; /* and
adjust the staggering times to MainSeqStart*/

}

void loop() {
    timestamp = millis();

    if (timestamp > EscapeTime) { /* if it's not, then do nothing (keeps all pins OFF); if it is,
proceed to decision: main sequence or priming? */
        if(PrimeCycComplete > 0) { /* want to run the MAIN sequence in that case */

            /* MAIN SEQUENCE*/
            for (j = 0; j < NumberOfPins; j = j + 1) {
                /* still keep LED on if last on-switching was less than tIR ago: */
                if (timestamp < Pincode[j][3] + Pincode[j][1]) {PinState[j] = HIGH;}
                /* or if the last turning-off was more than tPause ago (and irrad was intended), then
immediately cycle over the counter j and set its LED to ON: */
                else if ((timestamp > Pincode[j][3] + Pincode[j][1] + PauseTimes[j]) && (Pincode[j][1]
> 5)) {Pincode[j][3] = timestamp; PinState[j] = HIGH;}
                /* else keep the circuit j state low: */
                else {PinState[j] = LOW;}
                /* Now write the pin and then treat the next pin along by cycling over the FOR loop. */
                digitalWrite(Pincode[j][0], PinState[j]);
            }

            else if(timestamp > EscapeTime + (PrimeCycles * PrimingTiming[1])){ PrimeCycComplete = 1;}
            /* check and raise the passflag if needed */
            else { /* run the priming sequence since main was not done, priming was not annulled, and
we are past the escape time */

                /* PRIMING SEQUENCE*/
                if(timestamp - PrimerCounter > PrimingTiming[1]) {PrimerCounter = timestamp;} /* scroll it
up like mod */
                m = (int) ((timestamp - PrimerCounter)/PrimingTiming[0]); /* set the (possibly unreal)
index number which should be made HIGH */
                for (j = 0; j < NumberOfPins; j = j + 1) {(PinState[j] = LOW);} /* turn all pins off,
first */
                if(m < NumberOfPins) {PinState[m] = HIGH;} /* then make the right pin HIGH */
                for (j = 0; j < NumberOfPins; j = j + 1) {digitalWrite(Pincode[j][0], PinState[j]);} /* write all pins */
            }
        } /*skips to here if we are inside Escape Time*/
    } /* Very Happy! */
}

```

Appendix 3: PST design and handling

Note in passing two unusually favourable features of the **PSTs**. (1) **PSTs** are *trans*-inactive. Thus they may be applied globally in their stable inactive *trans* form, and only photoisomerised to the active metastable *cis* inside the target zone of interest. This natively gives far easier spatial targeting than *trans*-active azobenzenes, which instead require active photoisomerisation everywhere outside the target zone to suppress off-target effects, which may be essentially impossible *in vivo*, and also in general is impossible to achieve quantitatively due to PSS considerations. (2) While azobenzenes are known to suffer bioreduction, the **PSTs** showed successful long-term intracellular applications, which we attribute to their extremely electron rich design (Beharry et al., 2011b).

Choice of Prodrug Strategies for PSTs

PST-1P: We anticipate that the biochemical activity of **PST-1P** is null until *both* phosphate cleavage by endogenous intracellular phosphatases *and* photoisomerisation take place, since the bulky phosphate group is expected (Tron et al., 2006) to prevent binding of *cis*-**PST-1P** to tubulin. We expect, and it is not contraindicated by experimental results, that such cleavage is nonspecific (many phosphatases are capable of it, and effects are not cell-type specific), and is rapid (the net activity of these phosphatases upon the candidate substrate **PST-1P** is high). Therefore **PST-1P** is essentially a delivery method for **PST-1** which (a) does not require using cosolvents (which may give side-effects or result in irregular biodistribution); and (b) can be applied in high concentrations since water solubility is ensured (at least 10 mM solubility in PBS); and (c) in a potential clinical setting, may ensure good delivery to target (Stella, 2006) - the negatively-charged phosphate is a key advantage for the isosteric **CA4P** compared to the lipophilic **CA4** (not only increases aqueous solubility, but eg. may reduce the drug's adsorption by hydrophobic carrier proteins in plasma) (Pettit and Rhodes, 2009). Points (b) and (c) may be vital for the efficiency and success of *in vivo* tumour treatment, since we expect that the *in vivo* drug response relationship at therapeutic concentrations will depend very nonlinearly on concentration (as seen *in cellulo*: eg. the sigmoidal fits of viability to $\log_{10}[\text{PST}]$ under the toxic regime, such as **Figure 2D**, have Hill coefficients around 3.6), so bolus-style, high-concentration application and target delivery could be exceptionally effective.

PST-2S: Water-soluble salt **PST-2S** is designed as an improvement (Ohsumi et al., 1998) over **PST-2** for *in vivo* work, with similar rationale as for **PST-1P**, including (a) a higher concentration can be supported in aqueous solution, and (b) better delivery to target. Likewise, it is expected that bioactivity requires the prior cleavage of the serine residue (see discussion in the section on **PST-1P** above). The serine residue is expected to be cleaved *in cellulo* nonspecifically (many peptidases may perform cleavage, and cleavage will not be cell/tissue type specific) by monopeptide-cleaving exopeptidases with relatively high substrate tolerance (eg. leucine aminopeptidase and membrane alanyl peptidase families, EC 3.4.11.1 and 3.4.11.2 respectively); however we anticipated that typical

enzymatic processing of **PST-2S** into **PST-2** would not be as fast as release of **PST-1** from **PST-1P**; and the tenfold drop of potency of **PST-2S** compared to **PST-2** (while the potency of **PST-1** is similar to that of **PST-1P**) may in part reflect such slower enzymatic processing.

PST-1CL was desired as a proof of principle for dual optical-and-biochemical targeting prodrugs. Phenolic phosphates such as **PST-1P** are biochemically nonspecific prodrugs due to the ubiquity of phosphatases. However, changes in the expression and activity of various peptidases have been widely documented in disorders such as cancers which are an obvious target for clinical applications of **PSTs** (Gill et al., 2014). Since numerous sequence-specific polypeptidases are known (eg. the tripeptide D-Ala-Phe-Lys- (de Groot et al., 2000) is specifically processed by the tumour-associated peptidase plasmin), using polypeptide sequences to target drug release specifically is attractive (Gill et al., 2014). However, although peptidyl anilides (as in design **PST-2S**) are tolerated by nonspecific monopeptidases to some degree, they are generally poor or unusable as mimics for the post-scissile portions of polypeptide-specific peptidase substrates (de Groot et al., 2000; Thorn-Seshold et al., 2012). Therefore, we wished to apply a cyclisation spacer design which (a) provides a highly robust prodrug in the absence of enzymatic hydrolysis (this robustness is favoured by the electron richness of the **PST-1** phenol), (b) bears an aliphatic amine post-scissile bond with low steric demand for optimal enzymatic processing, (c) features very rapid kinetics of spacer immolation and drug release (Thorn-Seshold et al., 2012), (d) favours water solubility for better chance of success in clinical settings, and (e) is designed so that the attachment site for the auto-immolative spacer-peptide unit blocks all biochemical activity of the *cis* prodrug until enzymatic processing takes place. These several design criteria are satisfied in **PST-1CL**. The peptide substrate we have chosen (leucine) to attach to this cyclisation spacer will not provide biochemical specificity to a single enzyme, but rather, **PST-1CL** should be seen as a proof of principle for design and synthesis of prodrugs with different peptide sequences (incorporated by reaction sequences analogous to that used for leucine here) that *will* enable true biochemical specificity for target cells to some degree, as well as optical control. The potential advantages of this dual targeting approach are discussed in Appendix 5.

Solubility and Handling

PST-1P's profile of light-dependent biological effects is indistinguishable from the two other most-potent candidates (**PST-1** and **PST-2**) but it surpasses them for convenience. It is easy to handle (hydrophilic) and soluble at >10 mM in PBS at room temperature; and its halflife for spontaneous degradation at room temperature under air (>100 days) implies that no special haste is required when preparing and applying solutions.

The non-prodrug **PSTs** instead (1) require a cosolvent and their solubility is temperature-dependent; and (2) they are hydrophobic, so brief handling instructions are detailed here. We recommend using

glass vials for preparing any stocks at concentrations above 100 µM; always performing dilutions such that the percentage of cosolvent is maximised along the chain of dilutions; and using only teflon cartridges to filter pure-MeCN-solutions, for these reasons:

- (1) Acetonitrile (MeCN) was found to be a much better *cosolvent* for these azobenzenes than DMSO; additionally, it is tolerated in cell culture at 10-20× higher percentage without significant effects. **PST-1** and **PST-2** are soluble at 100 µM with 2% MeCN at 25°C and may be diluted down keeping this cosolvent ratio (eg 10 µM, 0.2%). **PST-3** and **PST-5** require 2-3 times as much acetonitrile, and **PST-4** is intermediate in solubility between these cases. The MeCN used does not have to be top grade ("dry" MeCN may even be disadvantageous due to contaminants from the drying process).
- (2) Especially, the plastic surfaces of Eppendorf tubes (but also other surfaces such as standard cellulose filters and some pipette tips) can easily adsorb **PSTs**, which may not be obvious due to light scattering obscuring colouration. Adsorption losses depend entirely on stock preparation: this includes the particular compound's lipophilicity, the stock concentration coupled with its cosolvent percentage, the temperature, the settling time, and it can even be kinetically affected by order of addition. High adsorption results from working with concentrated solutions near their solubility limit (eg 100 mM in pure MeCN), but also when using medium-concentrated solutions at 2-20% MeCN (eg 0.1-2 mM) even if solubility is acceptable when solutions are contained in glass vials. The true concentration of a **PST** working stock can always be measured by UV-Vis absorbance, calibrating to the absorbance coefficients detailed in Part B. We have found adsorptive losses of the more lipophilic compounds of up to 70% when careful sample preparation is neglected.

Appendix 4: Photopharmacology: design, rationale, applications

From Principles to Biological Assay Design: Rationale

For convenience, $[Z]$ is defined as the instantaneous local concentration of the **cis-PST** isomer; $[Z]^*$ is defined as the time-average $[Z]$ experienced during a significant phase of an experiment (eg. the first phase of a two-phase experiment; see below); and t_{pause} is defined as the interval between light pulses in a pulsed experiment (if the experiment is a dual-wavelength experiment, each pulse is defined as containing both λ_{ACT} and λ_{DEACT}). A **target** is that spatiotemporal region where it is desired that the biological effects of the **PST** be most strongly applied, while it would be beneficial to avoid generating biological effects in all **off-target** zones.

Two *strong light-dependent steady-state* protocols are evident for the **PSTs**: (1) a toxic regime designed to maximise their pharmacological effect **on-target**, by applying *activating irradiation* at wavelength λ_{ACT} so as to generate a significant $[Z]^*$ in the **target**; continuous irradiation could be used, or else pulsed irradiation if t_{pause} were significantly shorter than τ ; an example pulsed toxic regime for compound **PST-1** (τ estimated around 8 minutes) could thus be “390 nm applied in pulses of 75 ms with $t_{\text{pause}}=30$ s”; and (2) a strong rescue regime, designed to deliver a rigorous test of the degree of photocontrol which can be exerted over the **PST**’s toxicity, by applying λ_{ACT} exactly as for the toxic regime, but competitively applying *deactivating irradiation* at wavelength λ_{DEACT} in order to reduce $[Z]^*$ relative to the value experienced in the toxic regime; like the toxic regime, this regime could be pulsed or continuous; an example pulsed strong rescue regime for compound **PST-1** could thus be “390 nm applied for 100 ms then 505 nm applied for 600 ms, with $t_{\text{pause}}=30$ s”.

One design we consider likely for localised therapeutic applications of the **PST** compounds is shown in principle in **Figure S1E**. A toxic regime is applied on a **target** synchronously with the application of a deactivating regime (featuring only the λ_{DEACT} component of an optimised strong rescue regime) in a thin protection zone surrounding this **target** (in order to reduce the exposure of the rest of the organism or sample to any **cis-PST** diffusing out of or transported away from the **target**, and counteract any scattering of λ_{ACT}). This may maximise the biological effects in a **target** while keeping the **off-target** $[Z]^*$ below the minimal response concentration, thereby avoiding side effects.

For such biomedical applications, the toxic regime thus gives an estimate of the maximum strength of the biological effects that can be exerted in a **target** zone by a given concentration of **PST**; and assuming that a deactivating regime can be applied in those off-**target** zones which are the very closest neighbours to this **target** zone, then the strong rescue regime estimates the maximum strength of the (undesirable) biological effects that could be experienced in the very nearest off-**target** zones (weaker biological effects are to be anticipated in off-**target** zones still further from the **target**).

Weak light-dependent protocols are defined as those where spontaneous *cis*→*trans* reversion plays a significant role in reducing [Z]*, and these may also be important in medicine and research. Examples include (3) a *dark rescue protocol*, where a toxic regime would be applied for the first phase of an experiment, then all light switched off throughout a second phase of the experiment thus allowing [Z] to reach zero; and (4) a *weak pulsed rescue regime* similar to the strong pulsed rescue regime but where t_{pause} is instead significantly longer than τ , such that the component of λ_{DEACT} in each pulse primes the sample to decay more rapidly to $[Z] \sim 0$ than would be possible by spontaneous reversion alone. Note that a weak pulsed rescue regime will always display lesser biological effects than the corresponding strong rescue regime (since the strong regime has a shorter t_{pause}).

Light can be applied either continuously (allowing very low intensities to be used), or in pulses (allowing for fixed source intensity, easier use, and permitting the weak pulsed rescue protocol). We always used pulsed protocols as they illustrated well the relationships between observed photopharmacological effects and the underlying qualitative trends of PSS(λ), E(λ) and τ described previously (see eg. **Figure S1C**). We focussed on strong light-dependent steady-state protocols, as these provide the most demanding proof of principle for fully reversibly light-controllable biological effects (compared to eg. the weak protocols described above): the corresponding weak protocols could always be applied with at least as much success. Lastly, λ_1 and λ_2 as defined in Part B.3 gave estimates for “good” values of λ_{ACT} and λ_{DEACT} by balancing the need to restrict the light flux applied, while still favouring one or the other isomer’s formation as much as possible. The values of λ_{ACT} and λ_{DEACT} used in optimised experiments could be refined empirically from these initial guesses, however we found this unnecessary.

***cis*-activity, dual targeting and other advantages for spatial precision**

Considering biomedical applications of photopharmaceuticals e.g. to chemotherapy (Velema et al., 2014), if target cells can be uniquely identified and spatially addressed by light (e.g. localised tumour), then cell-specific illumination may achieve cell-specific treatment, depending on the magnitude of the activity difference between the isomers and on the degree of control over isomerisation which is possible. An elegant solution for azobenzenes is if the *trans* is totally inactive and if the *cis*→*trans* halflife is moderate (the **PSTs** feature these two properties): then, they will be only photoisomerised to the active *cis* inside the target zone, and spontaneous *cis*→*trans* isomerisation outside this irradiated target zone, optionally aided by active photoswitching towards the *trans* as in the “belt zone” concept, should eliminate the toxic burden of diffusing/transported active *cis* on surrounding cells, *entirely* avoiding side-effects off-target. Such photopharmaceuticals may avoid the dose-limitations that the current always-ON antimitotics suffer (primarily due to cardiotoxicity, immunosuppression, endothelial toxicity and neurotoxicity), which may allow them to establish the truly optimum on-target dose (**OTD**) within such a spatially-addressable target, whereas

current drugs cannot. Thus a **PST** might achieve even better on-target effects than current therapies, but also without off-target effects elsewhere. These advantages correspond to the design features of an ideal general photopharmaceutical as reviewed by Feringa (Velema et al., 2014).

Yet even when tumour cells cannot be specifically addressed, and are surrounded by nearest-neighbour cells which must avoid toxicity (here called “blind targeting”), photopharmaceuticals such as **PSTs** may have therapeutic advantages over current agents. They will still only generate localised bystander toxicity, which must be preferable to the systemic side-effects that can be expected from conventional drugs; and as the OTD of **PSTs** can be chosen considering only this localised bystander toxicity, this may increase their usable OTD towards optimal therapeutic levels and thus improve the on-target therapeutic outcome compared to the always-ON case, as well as lowering the systemic load. Photopharmaceuticals might also for the first time allow treatment regimes tackling sensitive tissues piecewise (*e.g.* first treating one region, allowing tissue recovery, then treating the second region) to reduce the overall toxic challenge without being forced to apply lower (less therapeutic) drug doses.

In the context of blind targeting, the orthogonal extra level of target specificity from the preferential biochemical unmasking of **PST** prodrugs in a subpopulation of target cells within a tissue could be an important advantage, even compared to conventional biochemically-targeted prodrugs. Purely biochemically-targeted approaches are, generally, not entirely specific to targeted cells. Typically, a substrate’s processing is upregulated in the diseased state, rather than switched on from zero background; also, it is rare that processing of suitable substrates occurs with tissue-specificity for endogenous enzyme profiles; lastly, drug diffusion and bulk transport may occur after unmasking, further reducing spatial specificity. Yet, by dual optical-and-biochemical targeting, these effects may be compensated. *E.g.*, if enzymatic processing can occur in several distinct organs, but only one contains the target subpopulation, spatially localised irradiation can easily avoid generating off-target effects. Diffusion or bulk transport from the target zone after enzymatic activation may also be counteracted by localised optical deactivation.

Temporal modulation of photopharmaceuticals

Regardless of spatial precision effects however, photopharmaceuticals can deliver unique *temporal patterns* of their active form, which could provide significant advantages compared to conventional drugs, not only for cell biology research but potentially for clinical applications. This may give significant improvements to therapeutic effects, as well as greater mechanistic insight into treatment outcomes and more effective combination therapies.

Hat function dose(t) profiles: Recall that tumour cells in general show a different drug response profile to normal cells. In the long term, this provides a therapeutic margin where tumour destruction may involve an acceptable attrition of healthy bystander cells: this is the paradigm underlying decades of patient treatment with always-ON, nonspecific antimitotics, whose best achievable dosage regimes have been established by extensive pharmacokinetic trials and errors. Based on this intrinsic response difference, we first consider a simplistic picture where an **optimal OTD**, after maintenance for time t_{OPT} , would give some best possible overall therapeutic response: ie. the optimal OTD(t) is a “hat” function, which toggles from zero up to the optimal OTD and then back to zero after time t_{OPT} . *Truly off↔ON photopharmaceuticals such as **PSTs** can provide this hat function* (note that a situation approaching the “hat function” ideal profile $[\text{PST}]_{\text{eqm}}(t)$ has already been shown in the *C. elegans* experiments where active photoswitching was used to turn **PST-1** ON and OFF). Always-ON drugs rely on drug absorption and elimination to drive changes of the OTD, which constrains the conventional OTD(t) to exhibit only slow changes in concentration under typically biexponential kinetics. **Figure S1D** presents a model of a biexponential $[\text{toxin}](t)$ trace for a standard drug, compared to the OTD(t) trace for a *cis*-**PST** with the same underlying PK of the total pool of **PST**, but where irradiating wavelength (or, eg. irradiating intensity) would be modulated over time, depending on the local total concentration of **PST** (eg. with feedback *via* dynamic plasma concentration readout) so as to achieve a hat function of $[\text{cis-PST}](t)$. Essentially, the higher the local $[\text{PST}]_{\text{TOT}}$, the less *trans*→*cis* photoisomerisation is stimulated, but if even optimum *trans*→*cis* isomerisation would generate a suboptimal effect due to insufficient $[\text{PST}]_{\text{TOT}}$, then irradiation is stopped. The colour of the *cis*-**PST**(t) plot line at any given time is intended to reflect the wavelength applied, with red representing “no light applied” (since red is not absorbed by these **PSTs**); the colouration could instead be a heat-map reflecting the photon flux applied per unit time (intensity modulation), which would achieve the same behaviour. If an optimal OTD exists, the time spent at that dose can be maximised by the hat function which is possible profile for $[\text{cis-PST}](t)$. To recouch the result, the photopharmaceutical approach may eliminate therapeutically ineffective phases of conventional drug treatment (**Figure S1D**).

Other new PK patterns: Control of illumination wavelength, pulse repetition frequency and/or flux delivery (power × time) can also be imagined to modulate $[\text{cis-PST}](t)$ in other forms than a hat function, and even (were there merit to it) to reproduce the biexponential form shown for the conventional drug: the **PSTs**’ reversible optical control gives the flexibility to choose where, when, and how much of the compound should be activated. Since it may be unlikely that in all disease cases, an optimal therapeutic outcome is only achieved by a biexponential PK profile, such dynamic modulation could achieve therapeutic effects which it has not previously been possible to consider. *E.g.* **PST** treatment could allow applying numerous very short high-concentration spikes of *cis*-**PST**, each returning quickly to zero; these short spikes might be able to attain *cis*-**PST** levels well beyond

the maximum tolerated dose established for pharmacologically-equivalent but conventional drugs, but without giving unwanted effects, since the long phase of clearance is avoided. In the context of combination therapies too, the opportunity to turn one component (or several) on and off independently at will might allow great mechanistic insight and achieve better therapeutic outcomes.

Time-dependent toxicity: We also expect **PSTs** to exploit toxicity mechanisms which are regulated not only by dose but also by *time of application*; such that more sensitive (tumour) cells may tolerate *cis-PST* application for far shorter periods than do normal cells before committing to apoptosis, *even if in the long term*, with irreversibly-acting drugs, similar outcomes are achieved. Thus dynamic modulation to restrict exposure time might achieve intrinsic therapeutic selectivity.

Repeatability: Photochemical off↔ON switching may deliver a [toxin](t) profile which shows high temporal repeatability across different scenarios or patients, which may address problems faced when correlating applied doses with observed effects, or when selecting doses to administer, leading to improvements in monotherapy as well as greater understanding of its mechanisms.

Concluding remark on targeting and CDIs:

It may be that the *cis-PSTs* in particular can leverage non-linear effects inherent to their mode of action to improve on-target selectivity. For further information about CDI dynamics, and the varied and complex knock-on responses to MT inhibition on different levels (*in vitro* – cell culture – diffusion-limited culture – *in vivo*), the interested reader is referred to the reviews by Stanton (Stanton et al., 2011), de Tozer (Tozer et al., 2005; Tozer et al., 2002), Dumontet (Dumontet and Jordan, 2010), Jordan (Jordan et al., 1998), and Tron (Tron et al., 2006); from this last, we quote:

“... does the simple structure of **CA4** and the concentrated medicinal chemistry effort already profused mean that most interesting modifications have been exploited? Should medicinal chemists move to more complex natural products that have been shown to elicit effects on neovasculature? We believe not, since more challenges lie ahead. The strong cytotoxic nature of **CA4**, for example, would make it an excellent bullet against the tumor itself, if properly targeted...”
(Tron et al., 2006)

Munich, September 2014

Supplemental References

- Bailey, K., Cowling, R., Tan, E.W., and Webb, D. (2004). A colormetric assay for catechol-O-methyltransferase. *Bioorg Med Chem Lett* 12, 595-601.
- Bastos, E.L., Ciscato, L.F.M.L., and Baader, W.J. (2005). Microwave-Assisted Protection of Phenols as tert-Butyldimethylsilyl (TBDMS) Ethers Under Solvent-Free Conditions. *Synth Commun* 35, 1501-1509.
- Beharry, A.A., Sadovski, O., and Woolley, G.A. (2011a). Azobenzene Photoswitching without Ultraviolet Light. *J Am Chem Soc* 133, 19684-19687.
- Beharry, A.A., Wong, L., Tropepe, V., and Woolley, G.A. (2011b). Fluorescence Imaging of Azobenzene Photoswitching In Vivo. *Angew Chem, Int Ed* 50, 1325-1327.
- Beharry, A.A., and Woolley, G.A. (2011a). Azobenzene photoswitches for biomolecules. *Chem Soc Rev* 40, 4422-4437.
- Beharry, A.A., and Woolley, G.A. (2011b). Photoswitch Design. In *Photosensitive Molecules for Controlling Biological Function*, pp. 171-184.
- Bisby, R.H., Botchway, S.W., Hadfield, J.A., McGown, A.T., Parker, A.W., and Scherer, K.M. (2012). Fluorescence lifetime imaging of E-combretastatin uptake and distribution in live mammalian cells. *European Journal of Cancer* 48, 1896-1903.
- Boonacker, E., and Van Noorden, C.J.F. (2001). Enzyme Cytochemical Techniques for Metabolic Mapping in Living Cells, with Special Reference to Proteolysis. *J Histo Cyto* 49, 1473-1486.
- Cushman, M., Nagarathnam, D., Gopal, D., Chakraborti, A.K., Lin, C.M., and Hamel, E. (1991). Synthesis and evaluation of stilbene and dihydrostilbene derivatives as potential anticancer agents that inhibit tubulin polymerization. *J Med Chem* 34, 2579-2588.
- de Groot, F.M.H., van Berkum, L.W.A., and Scheeren, H.W. (2000). Synthesis and Biological Evaluation of 2'-Carbamate-Linked and 2'-Carbonate-Linked Prodrugs of Paclitaxel: Selective Activation by the Tumor-Associated Protease Plasmin. *J Med Chem* 43, 3093-3102.
- Desai, A., Cramer, L., and Mitchison, T. (2012). Fluorescence Procedures for the Actin and Tubulin Cytoskeleton in Fixed Cells. <<http://mitchison.med.harvard.edu/protocols.html>>.
- Dumontet, C., and Jordan, M.A. (2010). Microtubule-binding agents: a dynamic field of cancer therapeutics. *Nat Rev Drug Discov* 9, 790-803.
- Friedman, O.M., Gofstein, R.M., and Seligman, A.M. (1949). Preparation of Azo Compounds for the Study of Inhibition of Tumor Growth. *J Am Chem Soc* 71, 3010-3013.
- Gottlieb, H.E., Kotlyar, V., and Nudelman, A. (1997). NMR Chemical Shifts of Common Laboratory Solvents as Trace Impurities. *J Org Chem* 62, 7512-7515.
- Harrowven, D.C., Guy, I.L., Howell, M., and Packham, G. (2006). The Synthesis of a Combretastatin A-4 Based Library and Discovery of New Cooperative ortho-Effects in Wittig Reactions Leading to (Z)-Stilbenes. *Synlett*, 2977-2980.
- Hetenyi, A., Martinek, T.A., Lazar, L., Zalan, Z., and Fulop, F. (2003). Substituent-Dependent Negative Hyperconjugation in 2-Aryl-1,3-N,N-heterocycles. Fine-Tuned Anomeric Effect? *J Org Chem* 68, 5705-5712.
- Jordan, M.A. (2002). Mechanism of action of antitumor drugs that interact with microtubules and tubulin. *Current Medicinal Chemistry: Anti-Cancer Agents* 2, 1-17.
- Mallory, F.B., and Mallory, C.W. (2004). Photocyclization of Stilbenes and Related Molecules. In *Organic Reactions* (John Wiley & Sons, Inc.).
- Mylavarampu, R.K., Kondaiah, G.C.M., Kolla, N., Veeramalla, R., Koilkonda, P., Bhattacharya, A., and Bandichhor, R. (2007). Boric Acid Catalyzed Amidation in the Synthesis of Active Pharmaceutical Ingredients. *Org Process Res Dev* 11, 1065-1068.
- Shindo, K., Nakamura, R., Chinda, I., Ohnishi, Y., Horinouchi, S., Takahashi, H., Iguchi, K., Harayama, S., Furukawa, K., and Misawa, N. (2003). Hydroxylation of ionized aromatics including carboxylic acid or amine using recombinant *Streptomyces lividans* cells expressing modified biphenyl dioxygenase genes. *Tetrahedron* 59, 1895-1900.
- Stella, V. (2006). Prodrug Strategies for Improving Drug-Like Properties; in, Optimizing the “Drug-Like” Properties of Leads in Drug Discovery, R.T. Borchardt, E.H. Kerns, M.J. Hageman, D.R. Thakker, and J.L. Stevens, eds. (Springer New York), pp. 221-242.
- Tozer, G.M., Kanthou, C., and Baguley, B.C. (2005). Disrupting tumour blood vessels. *Nat Rev Cancer* 5, 423-435.
- Velema, W.A., Szymanski, W., and Feringa, B.L. (2014). Photopharmacology: beyond proof of principle. *J Am Chem Soc* 136, 2178-2191.